



HAL
open science

Génération et télécontro

Campuzano Gabriel

► **To cite this version:**

Campuzano Gabriel. Génération et télécontro. domain_other. Télécom ParisTech, 2003. English.
NNT: . pastel-00002459

HAL Id: pastel-00002459

<https://pastel.hal.science/pastel-00002459>

Submitted on 25 Jun 2007

HAL is a multi-disciplinary open access archive for the deposit and dissemination of scientific research documents, whether they are published or not. The documents may come from teaching and research institutions in France or abroad, or from public or private research centers.

L'archive ouverte pluridisciplinaire **HAL**, est destinée au dépôt et à la diffusion de documents scientifiques de niveau recherche, publiés ou non, émanant des établissements d'enseignement et de recherche français ou étrangers, des laboratoires publics ou privés.



Thèse

présentée pour obtenir le grade de docteur de l'École Nationale
Supérieure des Télécommunications

Spécialité: Électronique et Communications

Gabriel Campuzano

Génération et télécontrôle de signaux
radiofréquences par synchronisations optiques
multiples de lasers à semi-conducteurs

*(Remote Generation and Control of Radiofrequency Signals Using
Multiple Optical Synchronizations of Semiconductor Lasers)*

Soutenu le 17 Mars 2003 devant le jury composé de

Guy Michel Stephan	Président
Klaus Petermann Michel Têtu	Rapporteurs
Didier Decoster Bruno Thedrez	Examineurs
Philippe Gallion	Directeur de thèse

Acknowledgments

I would like to express my most sincere gratitude to my supervisor, Philippe Gallion, whose expertise, guidance, and patience, inspired me through all my research project. I greatly admired his passion for the field and his clever ability to spread knowledge about it.

I would like to specially thank Guy Stephan for giving me the honor of presiding the Jury. I really appreciated the reports made by Klaus Petermann and Michel Têtu on my thesis for it provided me with great insight and tons of reflection material. My examiners, Didier Decoster and Bruno Thedrez have my deepest gratitude.

The serious and quality-rich scientific environment I found at school in conjunction with some fun now and then a few blocks away from the lab greatly enriched my learning experience; and to that matter, I owe very special thanks to the *permanents*, Yves, Duan, Didier, Claude, Guy, Cédric, and Gabet. Evidently, I am also grateful for the assistance they provided at all levels of the research project. The kind assistance and support received from Alan, at the mechanics shop, and from Danielle and Marie Baquero at administration greatly simplified my life. I thank them deeply.

During long hours at and after school I had the privilege of getting acquainted with excellent characters I believe I will never forget. Their a major contribution to numerous happy days; thanks to my fellow friends Carlos, Cristophe, Beatriz, Laurent, Stephan, Robson, Haroun, Elena, Ousama, Olivier, Sabine, Arash... and the list continues, Sebastian, Guillaume, Antoine, Mohammed, Elizabeth, Virginie, Joseph, Isabelle, and Fernando.

This work was made possible thanks to the financial aide I received from CONACyT (Consejo Nacional de Ciencia y Tecnología) and SFERE (Société Française d'Exportation des Ressources Éducatives); and also to the non-occasional donations I received from my father.

Résumé

Ce travail se trouve simultanément dans la frontière du domaine des communications optiques et micro-ondes et dans le domaine de l'optoélectronique. Les réseaux d'accès futurs, notamment, les réseaux LMDS (Local Multipoint Distribution System), MVDS (Multipoint Video Distribution System), and MBS (Mobile Broadband System) se développeront dans la zone millimétrique du spectre électromagnétique. Par conséquent, il y aura besoin d'une génération et transport des signaux millimétriques sur des portées peu compatibles avec l'atténuation, le facteur de bruit et la dynamique des circuits et lignes classiques. La radio sur fibre ou réseaux hybrides sont aujourd'hui la solution la plus attractive car plusieurs avantages ont été démontrés : les stations de bases à faible coût, la faible atténuation de la fibre, les porteuses RF à haute fréquence, plus d'utilisateurs par surface, le grand facteur de réutilisation de fréquences et la puissance RF réduite. Étant donnée l'indéniable importance acquise par le marché des télécommunications récemment, il faut mener une étude minutieuse des ressources techniques disponibles afin d'augmenter la capacité de liaisons de la boucle locale.

Les nombreux avantages de la génération de signaux radiofréquences, basée sur la transmission et le battement de signaux optiques de fréquences différentes et de phases fortement corrélées, présente une solution apparemment effective et élégante. L'écart en fréquence entre les deux signaux correspond à la fréquence RF désirée, et leur battement au niveau de la photodiode produit un signal RF très pur, avec un rapport signal sur bruit important. Une technique, il n'y a pas longtemps proposé pour la génération de deux signaux optiques de fréquences différentes avec une forte corrélation de phase, est la synchronisation optique de deux lasers esclaves sur différentes bandes latérales de modulation d'un même laser maître. Cette technique permet à la fois le télécontrôle des caractéristiques du signal RF généré à la station de base, une large plage d'accordabilité en fréquence (~100GHz) grâce aux caractéristiques de modulation (AM/FM) du laser maître et un bruit de phase très faible, dès lors qu'une très bonne corrélation est préservée

entre les phases des lasers esclaves. De plus, ce faible bruit de phase, permet l'utilisation des formats de modulation spectralement efficaces pour le transport d'information. Par ailleurs, la puissance optique est concentrée seulement sur deux porteuses optiques, ce qui entraîne une technique de très bon rendement pour la génération RF ainsi qu'un transport fibré moins sensible à la dégradation due à la dispersion chromatique. Pour le transport multicanaux, il ne faut qu'intégrer plus de lasers esclaves synchronisés sur différentes bandes latérales de modulation du laser maître dans la station de contrôle. Tout cela incite une étude expérimentale et théorique pour la compréhension des mécanismes physiques associés à la synchronisation optique des lasers à semi-conducteur et leur effet sur les propriétés spectrales de porteuse RF ainsi générée.

Tout d'abord, dans le premier chapitre, une analyse de performance de la liaison, comprenant les divers paramètres de la conception, comme le transmetteur optique de double fréquence, la distance de transmission, la dispersion chromatique de la fibre, les retards différentiels et la fréquence RF désirée, est faite. L'influence de ces paramètres sur le signal sur bruit, le bruit de phase, le taux d'erreur binaire et la distance maximale de transmission est aussi discuté. En particulière, la puissance de sortie du photodétecteur est calculée étant donnée la possible relaxation de contraintes d'amplification au niveau de la station de base et par conséquent la possible réduction de coût du système. La génération RF autour des 60 GHz et le transport d'information en format de modulation QPSK sans erreur sont possibles sur une distance de 15 km pourvu que la dispersion chromatique soit compensée par un retard différentiel entre les deux lasers esclaves.

Ensuite, dans le deuxième chapitre, une étude théorique sur le processus d'injection et synchronisation optique des lasers à semi-conducteur à réaction distribuée est présentée. Un modèle basé sur les équations d'ondes couplées est développé afin de décrire précisément l'injection optique dans les lasers DFB. Plusieurs structures sont discutées pour comprendre les capacités du modèle. Une analyse de stabilité révèle la détermination de la bande de synchronisation et sa dépendance vis-à-vis des caractéristiques intrinsèques de la structure et du réseau de Bragg. Dans ce dessein, la réflectivité équivalente de la face du laser dû à l'injection est calculée puis son association à la différentiation de l'équation des valeurs propres a permis la détermination de variations

statiques de la fréquence et du gain. C'est-à-dire, on a déduit une expression pour la bande d'accrochage qui met en évidence les caractéristiques du réseau de Bragg du laser. Remarquons que la bande d'accrochage croît d'une façon non linéaire alors que la constante de couplage du réseau de Bragg diminue. Les résultats soulignent, de plus, les différences entre les lasers à cavité Fabry-Pérot et les lasers à réaction distribuée.

Plusieurs simulations de grand signal ont été faites à l'aide de la méthode numérique de différences finies. Les variations de la fréquence et du gain du laser injecté sont incluses dans les équations d'onde couplées dépendant du temps. Une analyse de stabilité montre comment le temps d'amortissement associé aux fréquences de relaxation dépende des caractéristiques du réseau de Bragg. Ceci impose une limite à la valeur maximale du taux d'injection pour un écart fréquentiel donné pour que la synchronisation soit maintenue. Cette valeur maximale diminue alors que la constante de couplage du réseau croît. Les résultats numériques sont ensuite présentés pour différents régimes d'injection et comparés avec des résultats expérimentaux. Une très bonne concordance a été trouvée. Afin de illustrer l'applicabilité du modèle au sujet de la thèse, la génération RF basée sur le transmetteur comprenant deux lasers esclaves est simulée et présentée.

Dans le cadre expérimental, dans le chapitre 3, une étude de caractérisation des lasers DFB a été menée. En particulier, les caractéristiques statiques, de modulation et du bruit, ont été déterminées par les moyens classiques de mesure. La procédure de stabilisation de l'injection optique et les résultats concernant la bande d'accrochage ont été documentés. Par ailleurs, une nouvelle mesure des variations réelles et imaginaires de l'indice du laser dû à l'injection optique externe a été proposée et réalisée. La technique consiste en l'utilisation de la réflectométrie à faible cohérence sensible à la phase et les résultats permettent, de plus, la détermination du facteur d'élargissement de raie du laser où un très bon accord a été trouvé avec des autres mesures indirectes.

Finalement, dans le quatrième chapitre, la génération optique de signaux RF basé sur les synchronisations multiples des lasers à semi-conducteur a été expérimentalement étudiée. L'optimisation du spectre d'un laser maître modulé, et des spectres des différents lasers esclaves synchronisés sur deux de ses bandes latérales de modulation, permet

l'obtention, par battement hétérodyne, de signaux radiofréquences de très hautes qualités spectrales. Le contrôle du taux d'injection, du signe de son désaccord fréquentiel et le choix des bandes latérales permettent une optimisation des signaux RF ainsi générés. Plus particulièrement, on a trouvé que la modulation du laser maître devait donner comme résultat un spectre de bandes latérales le plus large et le plus plat possible afin de permettre une large plage d'accordabilité des signaux générés, par la sélection possible de nombreux harmoniques. Ceci est simplement obtenu par l'utilisation d'une forte profondeur de modulation du courant du laser maître. Quant aux lasers esclaves, la dépendance de largeur de bande d'accrochage en fonction du taux d'injection a été clairement établie. Un compromis doit être trouvé entre un taux d'injection élevé, élargissant la bande d'accrochage et améliorant la stabilité, dans les limites de la zone d'accrochage, et la dégradation du spectre résultant de l'injection des bandes latérales adjacentes. Ces dernières constituent en effet autant de sollicitations pour le laser esclave et le recouvrement de leurs différentes bandes de synchronisation dégrade le spectre émis. Les spectres des lasers esclaves s'améliorent considérablement par un faible taux d'injection ($\sim -40\text{dB}$), ce qui augmente le taux de réjection des bandes latérales de modulation résiduelles. L'optimisation des spectres des lasers maître et esclaves sur les critères précédemment mentionnés et la sélection des bandes latérales les plus favorables permettent l'obtention une porteuse RF avec un taux de réjection des fréquences non désirées de 23 dB, un rapport « porteuse sur bruit » de 45 dB et une largeur spectrale inférieure au Hz. Les expériences menées ont permis d'obtenir de fréquences de porteuse allant jusqu'à 20 GHz, limité uniquement par la largeur de bande de l'analyseur de spectre RF.

Les contributions principales de ce travail peuvent être résumé en quatre points :

1. Une analyse de faisabilité sur les performances d'une liaison optique générant de radiofréquences au niveau de la photodiode. Cette étude est basée sur le calcul du bruit de phase de la porteuse RF générée. La faisabilité de transmissions avec un taux d'erreur binaire ($BER < 10^{-9}$), à une porteuse de 60 GHz modulée en QPSK 155 Mbps sur de distances ~ 15 km, a été établie, pourvu que la dispersion chromatique de la fibre soit compensée par un retard différentiel entre les deux lasers esclaves.

2. Une méthode basée sur la théorie des ondes couplées pour décrire les variations de la fréquence et du gain dues à l'injection optique dans les lasers à réaction distribuée. Comme résultat, la dépendance de la bande d'accrochage sur les caractéristiques du réseau de Bragg de la cavité a été déterminée.

3. Une méthode de mesure des variations de la fréquence et du gain dues à l'injection optique dans les lasers à réaction distribuée basée sur la réflectométrie optique à faible cohérence et sensible à la phase. Les résultats ont été directement utilisés pour l'estimation du facteur d'élargissement d'Henry.

4. Une procédure expérimentale pour optimiser les caractéristiques spectrales des signaux RF optiquement générées en termes de la densité de puissance spectrale des lasers maître et esclave et des conditions d'injection. Des porteuses RF montant jusqu'aux 20 GHz ont été générées gardant un bruit de phase inférieure au hertz, un signal sur bruit de 45dB et un taux de rejection de fréquences résiduelles > 23 dB.

Remote Generation and Control of Radiofrequency Signals Using Multiple Optical Synchronizations of Semiconductor Lasers

Abstract

Basically, the topic of this work lies at frontier of the optoelectronic and microwave communications fields; a combination of fields frequently called microwave photonics. Future access networks like LMDS (Local Multipoint Distribution System), MVDS (Multipoint Video Distribution System), and MBS (Mobile Broadband System) will work in the 25-70 GHz range. Consequently, they will need the generation and transport of millimeter signals over distances that are not compatible with the attenuation, noise factor, and dynamic range of classical microwave circuits and transmission lines. Hybrid networks (radio over fiber) are today the most attractive solution since several advantages can be acknowledged: low-cost base stations, low fiber attenuation, high frequency RF carriers, more users per surface, high reuse frequency factor and reduced RF power. Given the undeniable importance the telecommunications market has been acquiring in the past two decades, a thorough examination of available resources to satisfy the increasing bandwidth demand is in place. The numerous advantages of the sideband injection locking technique for optical generation and control of microwaves suggest further scrutiny of the physical mechanisms involved in this technique. Obviously, complete comprehension of the device physical behavior is not sufficient as an objective. A full performance assessment in terms of practical design issues was added.

The sideband injection locking technique consists in optical heterodyning the signals of two slave lasers frequency-separated by the desired microwave frequency. The resulting RF phase noise caused by the spontaneous emission of photons in each slave laser cavity is cancelled by injection locking to the modulation sidebands of a master laser. The master laser is sub-harmonically modulated so that only low-cost and commercially available microwave components and laser-diodes are required in the control station. Although its

implementation is somewhat complex, the technique offers a variety of advantages. A great flexibility regarding the microwave frequency is offered since it is given by the frequency spacing of the two lasers. Frequencies from some megahertz up to the terahertz-region are possible. Due to the low phase noise, RF carriers with sub-hertz linewidths can be obtained and bandwidth efficient broadband modulation formats can be applied. The data modulation is simply carried out directly via the laser injection current. In contrast to other optical microwave generation techniques, a further advantage of this method is that the optical power is concentrated only in two optical waves. Thus, it represents a very efficient microwave generation technique, which is also suitable for long distances without degradation due to fiber dispersion. For multi-channel operation, further slave lasers with different optical frequencies are added in the optical transmitter. Furthermore, the injection-locked lasers represent a multifunctional element: they act as an optical narrow-band filter, as an amplifier and as a phase modulator with a modulation speed determined by the maximum system bit rate.

First of all, a feasibility analysis characterizing link performance in terms of design parameters, such as the dual-frequency optical transmitter, transmission distance, fiber dispersion, differential delays, and carrier frequency is carried out. The influence of these parameters on signal to noise ratio, phase noise, bit error rate, and the longest possible transmission distance are discussed as well. In particular, close attention is given to the output power of the photodetector, which plays an important role on cost reduction and link gain. The different candidate photodetectors are briefly discussed highlighting the advantages and drawbacks of each. It was found that errorless transmissions are possible in the 60GHz range using a 155 Mbps QPSK format over 15 km of fiber distance as long as the dispersion delay is compensated by a differential delay between both slave lasers.

The study of injection locking of distributed feedback semiconductor lasers applied to fiber radio access systems is also presented. A semiconductor laser model is developed to accurately describe optical injection in distributed feedback semiconductor lasers. In view of its potentiality in numerous applications it is important to fully describe. Different structures are discussed so as to understand the capabilities of the model. A stability analysis reveals a precise determination of the locking range and the dependency on

intrinsic characteristics is established. To do so, the gain and frequency variations due to optical injection are calculated using the coupled-wave equations as a starting point. Including a modified facet reflectivity in the analysis, it was possible to deduce a locking bandwidth appropriate for DFB lasers. The results highlight the difference between the synchronization process occurring in DFB lasers and Fabry-Perot lasers. The latter are well described using the modified Adler rate equation governing the phase of an injected oscillator. It was found that the locking bandwidth non-linearly increases as the coupling strength of the laser grating decreases. The frequency and gain variations due to external injection are included in the time-travelling coupled-wave equations for DFB lasers. A stability analysis shows how the static/dynamic limit defined by the damping time associated to the relaxation oscillations depends on the grating characteristics. The modified coupled-wave equations are then solved numerically by implementing an appropriate central finite-differences scheme. Applications of the model are finally studied. The simulation results are afterwards presented for different injection regimes and compared to experimental ones. To further illustrate the proposed model, both simulation and experimental results on microwave generation by sideband injection locking of two DFB lasers are presented.

An experimental study of the distributed semiconductor lasers used through the thesis is presented. First, the static, noise and modulation characteristics are described through different classical measurement schemes. The experimental results concerning injection locking of DFB semiconductor lasers and the stabilization procedure are given. An optical low-coherence reflectometer (OLCR) is proposed to measure optically induced index and gain changes. As a result, a direct non-invasive technique for the determination of the linewidth enhancement factor was successfully developed for the first time and the measured factor agrees with stop-band indirect measurements.

Optically generated microwaves using the sideband injection locking technique are finally experimentally investigated. After presenting the experimental procedure, conditions on the modulation properties of the master laser are established. It was found that a large modulation depth is necessary for achieving a flat spectral comb, which in turn is necessary for simultaneously maximizing the RF carrier to noise ratio and relaxing

filtering conditions at the receiver. Then, sideband injection locking is compared to fundamental peak locking with the objective to find stability conditions. Optical generation of microwaves is experimentally demonstrated and RF properties are discussed. Limited only by the spectrum analyzer bandwidth and resolution, up to 20 GHz microwave carriers were generated exhibiting a sub-hertz phase-noise linewidth, with a carrier to noise ratio ~45 dB and a residual rejection rate ~23 dB.

Table of Contents

LIST OF FIGURES	1
CHAPTER0: INTRODUCTION.....	1
0.1 INTERACTIVE BROADBAND APPLICATIONS.....	2
0.2 JUSTIFYING FIBER RADIO SYSTEMS.....	3
0.3 EXPLORATION OF POSSIBLE TECHNIQUES	5
0.3.1 Direct Modulation of Semiconductor Lasers	6
0.3.2 Modulation Sideband Technique	6
0.3.3 Dual Mode Laser	7
0.3.4 External Modulation Technique	7
0.3.5 Mode-Locked Lasers.....	8
0.3.6 Sideband Injection Locking Technique	8
0.4 THESIS OVERVIEW	9
0.5 REFERENCES	11
CHAPTER 1: GENERALITIES OF THE HETERODYNE DETECTION SCHEME.....	15
1.1 HETERODYNE DETECTION SCHEME.....	16
1.1.1 Differential Delay Influence on Phase Noise.....	18
1.1.2 Bit Error Rate Analysis	23
1.1.3 RF Output Power	28
1.2 PHOTODETECTORS	31
1.2.1 Recent Photodiode Technology.....	32
1.2.2 Three-port Detectors	33
1.2.3 Optical Control of MMIC Devices.....	33
Summary	34
1.3 CONCLUSION	35
1.4 REFERENCES	36
CHAPTER 2: INJECTION LOCKED DFB LASERS	39
2.1 COUPLED-WAVE THEORY OF DFB SEMICONDUCTOR LASERS	40
2.2 OPTICALLY INDUCED FREQUENCY AND GAIN CHANGES	42
2.3 INJECTION LOCKING DYNAMIC MODELING	46
2.3.1 Stability.....	47
2.3.2 Numerical Model Implementation	49
2.3.3 Injection Regimes.....	50
2.3.4 Chirp Reduction and Optical PSK Modulation	53
2.3.5 Microwave Generation	54
2.4 CONCLUSION	56
2.5 REFERENCES	57

CHAPTER 3: EXPERIMENTAL STUDY I, LASER CHARACTERISTICS AND INJECTION LOCKING PROPERTIES	59
3.1 DESCRIPTION OF DFB SEMICONDUCTOR LASERS USED	60
3.1.1 Laser Chip Assembly	60
3.1.2 Static Characteristics	61
3.1.3 Modulation Properties	64
3.1.4 Laser Linewidth	66
3.2 INJECTION LOCKING CHARACTERISTICS	68
3.2.1 Schema and Control Parameters	68
3.2.2 Locking Bandwidth	69
3.2.3 Injection Regimes	72
3.3 OPTICALLY INDUCED INDEX CHANGES	73
3.3.1 OLCR Technique	74
3.3.2 Reflection Coefficient of a DFB Laser	75
3.3.3 Free-Running Lasers at 0 mA Bias	77
3.3.4 Free-Running Lasers Above Threshold	78
3.3.5 Injection-Locked Lasers	79
3.4 CONCLUSION	81
3.5 REFERENCES	82
CHAPTER 4: EXPERIMENTAL STUDY II, MICROWAVE GENERATION	84
4.1 EXPERIMENTAL PROCEDURE	85
4.2 MODULATION CONDITIONS FOR THE MASTER LASER	86
4.2.1 Master Laser Modulation	86
4.2.2 Free-Running Beating	87
4.3 SIDEBAND INJECTION LOCKING CHARACTERISTICS	88
4.3.1 Locking Bandwidth Overlapping	89
4.3.2 Injection Rate Influence	90
4.3.3 Frequency Detuning Influence	92
4.3.4 Injection Locking Stability	93
4.4 EXPERIMENTAL DEMONSTRATION OF MICROWAVE GENERATION	95
4.4.1 Optimal Sideband Injection Locking	95
4.4.2 Spectral Analysis of RF Frequencies	97
4.4.3 Influence of the Injection Rate on RF Spectrum	99
4.4.4 Transmission Over 30 km of a Single-Mode Fiber	100
4.4.5 RF Characteristics	102
4.5 CONCLUSION	104
CHAPTER 5: GENERAL CONCLUSION	105
JOURNAL AND CONFERENCE PUBLICATIONS ISSUED FROM THIS WORK	109

List of Figures

Figure 0.1: Different service requirements in terms of session time vs. bandwidth.....	3
Figure 0.2: A fiber radio system where remote generation and control are carried out at the control station.....	4
Figure 1.1: Fiber optic transmission of two signals showing the possible photocurrent power spectrums.	16
Figure 1.2: Delay induced penalty on the carrier to noise ratio.....	19
Figure 1.3: Phase noise spectrum in function of the frequency.....	20
Figure 1.4: Phase error in function of the total differential delay.....	21
Figure 1.5: Total differential delay in function of the transmission distance and carrier frequency product.....	22
Figure 1.6: Path imbalance needed for fiber dispersion compensation.....	22
Figure 1.7: Bit error rate in function of the path imbalance for a 15 km transmission distance.	26
Figure 1.8: Bit error rate in function of the carrier to noise ratio for different modulation formats.	26
Figure 1.9: Dispersion compensation tolerance at BER of 10^{-9}	27
Figure 1.10: Bit error rate in function of the transmission distance for a carrier to noise ratio of 16 dB and without dispersion compensation.	27
Figure 1.11: Heterodyning at the photodiode.....	28
Figure 1.12: RF output power in function of the received optical power of each carrier.	29
Figure 1.13: RF output power in function of RF input power for several transmission distances.....	30
Figure 1.14: Link gain for two different detector quantum efficiencies (dotted line id for direct detection).....	31
Figure 2.1: DFB semiconductor laser structure.....	42
Figure 2.2: Coefficient C_l for the DFB laser structure.	45
Figure 2.3: Static locking bandwidth for different coupling coefficients.	46
Figure 2.4: Dynamic limit of the stable locking range for different coupling coefficients.	48
Figure 2.5: Stable locking bandwidth depicting the different injection regimes.....	51
Figure 2.6: Frequency synchronization of the slave laser to the master laser.....	52

Figure 2.7: Operation at the edge of the static locking bandwidth.	53
Figure 2.8: Nonlinear mixing between the master laser frequency and the slave laser free-running frequency.	53
Figure 2.9: Self-pulsating regime.	53
Figure 2.10: Chaotic behavior provoked by a high injection rate.	53
Figure 2.11: Free-running spectrum of the modulated DFB laser.	54
Figure 2.12: Injection-locked spectrum of the modulated DFB laser.	54
Figure 2.13: Free-running spectrum of the beat signal between the slave lasers.	55
Figure 2.14: Power spectrum of the slave lasers synchronized to different IM-FM sidebands.	55
Figure 2.15: Power spectrum of the beat signal between the injection-locked slave lasers.	55
Figure 3.1: DFB Laser structure	60
Figure 3.2: Mechanical assembly	61
Figure 3.3: Power-current characteristics of the laser diode and its optical spectrum above threshold.	62
Figure 3.4: Wavelength dependence on biasing current	63
Figure 3.5: Wavelength dependence on temperature	64
Figure 3.6. Modulated master laser optical spectrum with no drive current amplification.	66
Figure 3.7. Modulated master laser optical spectrum with drive current 35 dB amplification.	66
Figure 3.8: Self-homodyne technique for measuring the laser linewidth.	67
Figure 3.9: Self-homodyne spectrum.	67
Figure 3.10: Setup for injection locking experiments.	69
Figure 3.11: Non-synchronized slave laser spectrum.	70
Figure 3.12: Theoretical fit (continuous line) and measured data (dots) of the locking bandwidth.	71
Figure 3.13: Stable locking (i).	73
Figure 3.14: Unlocked slave laser spectrum (ii).	73
Figure 3.15: Relaxation oscillations sidebands (iii).	73
Figure 3.16: Chaotic behavior (iii).	73
Figure 3.17: Experimental setup for the OLCR measurements.	75
Figure 3.18: Structure used to calculate the reflectivity coefficient as seen from the fiber/air interface.	75
Figure 3.19: Measure magnitude of the OLCR data.	77

Figure 3.20: Theoretical OLCR data.....	77
Figure 3.21: Phase of the OLCR data.....	78
Figure 3.22: Theoretical phase of the OLCR data.....	78
Figure 3.23: OLCR data above threshold.....	79
Figure 3.24: Calculated reflectogram above threshold.....	79
Figure 3.25: Complex index changes due to optical injection.....	80
Figure 4.1: Experimental setup used to optically generate microwaves.....	85
Figure 4.2: Optical spectrum of the modulated master laser.....	86
Figure 4.3: Parasitic modulation of the slave lasers.....	87
Figure 4.4: RF spectrum without microwave absorbers.....	88
Figure 4.5: RF spectrum with microwave absorbers.....	88
Figure 4.6: Locking bandwidth overlapping.....	90
Figure 4.7: Slave laser spectrum evolution as the injection rate varies.....	91
Figure 4.8: Optical spectrum of the locked slave laser at the injection rate limits for stable locking.....	92
Figure 4.9: Slave laser spectrum near the positive and negative detuning edge of the locking bandwidth.....	93
Figure 4.10: Sidebands peak power in function of the modulation depth with the overtone number as parameter.....	96
Figure 4.11: Beatnote power spectrum of the detected current.....	96
Figure 4.12: Master laser spectrum modulated at 4 GHz.....	97
Figure 4.13: RF Spectrum of free-running beating at 20 GHz.....	97
Figure 4.14: RF spectrum of the beating signal for different injection rates.....	99
Figure 4.15: Modulated master laser at 3 GHz.....	100
Figure 4.16: RF spectrum.....	100
Figure 4.17: Slave lasers optical spectrum.....	101
Figure 4.18: Resulting RF spectrum.....	101
Figure 4.19: Slave lasers optical spectrum.....	101
Figure 4.20: Resulting RF spectrum.....	101
Figure 4.21: Partial uncorrelation after 30 km of transmission distance.....	102

Chapter 0: **INTRODUCTION**

In recent years an increasing number of countries have been deregulating their telecommunication markets. Strong competition in these markets force network operators to modernize their infrastructure with special emphasis in satisfying the increasing bandwidth demand of private and small business subscribers. Traditionally, telephone networks were operated by telephone companies. New entrants in the market are cable television operators. The economics surrounding the telecommunication market bring both types of operators in to adopting a short-term approach for modernization of their existing networks. As a result, many of the improvements developed up to now are not compatible with each other. Moreover, they are not able to support high bit rate applications that need a large bandwidth and which are clearly foreseen in the near future.

This calls for innovative solutions and any network proposal should yield a roadmap that identifies the path for introducing new technologies, establishing simultaneously a short and a long-term goal. The short-term goal is to facilitate convergence by designing a universal architecture that allows *(i)* transparent interconnection of access networks and in-house networks, *(ii)* incorporating current technologies, and *(iii)* upgrading towards new technologies and infrastructures. The key interface in this architecture, connecting private and public networks, is referred to as the Residential Gateway (RG). The long-term aim is to reach far beyond the current state-of-technology by progressing to an architecture that will permit integration of advanced optical and wireless technologies, thus building the broadband Residential Area Highway.

Evidently, high quality services will continue to develop. The need for more bandwidth will thus continue to increase and the future home environment will be best served by the implementation of a network that offers high bandwidth and that is flexible in use. It is believed that options such as high bit-rate wireless links inside a small area interconnected to an optical fiber network have the best perspective. These types of systems are referred to as fiber radio systems and as it will be seen, the main idea behind them is to provide interactive broadband applications for the individual user.

0.1 Interactive Broadband Applications

Nowadays a lot of data is transferred in commercial networks for publishing reasons or for videoconferences. In the future, sending of CDs, documents by mail, etc. could also be replaced by data transfer on the information highway. In general, there are four classes of applications in the broadband area: moving images, data communication, mail and messaging, and on-demand services [1]. Moving images include applications as picture telephony, video conferencing, and video surveillance, which by the way, has become increasingly important in the last decade due to security reasons worldwide [2]. Data communication applications are, among others, LAN connections, CAD/CAM connections, and file and image transfer. As for mail and messaging, common transfers will be video-mails, large documents, and exchange of TV programs. Finally, desired on demand services might be teleeducation, data base access, movies on demand, radio and TV streaming, and digital newspaper. All these applications differ from each other in bandwidth, session time and burstiness as outlined in Figure 0.1.

A general view from the final-user perspective could be described as transmission and detection of broadband signals (including voice, data, and/or video) by anyone, anywhere, and at anytime. Current efforts to provide these services are the design of broadband fiber radio access systems, particularly systems like the Local Multipoint Distribution System (LMDS), the Multipoint Video Distribution System (MVDS), and the Mobile Broadband System (MBS) [3].

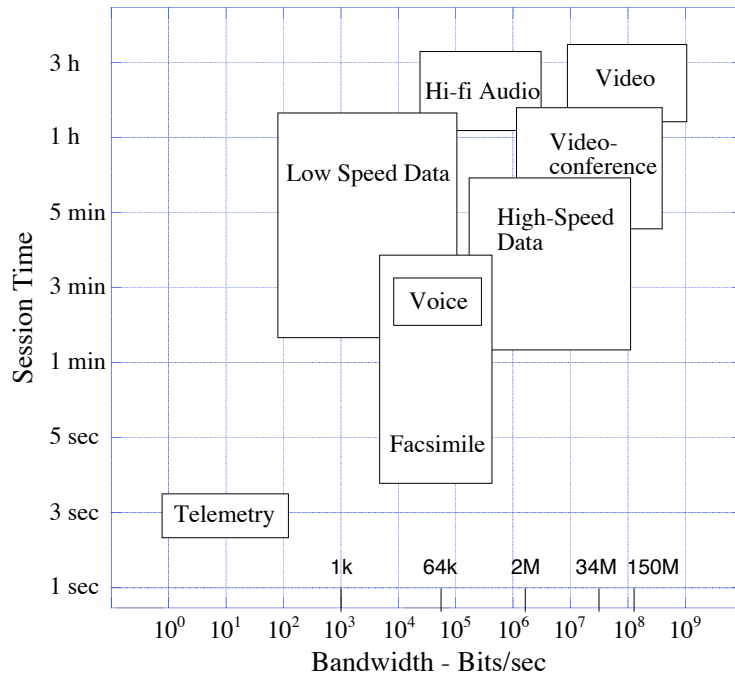


Figure 0.1: Different service requirements in terms of session time vs. bandwidth.

0.2 Justifying Fiber Radio Systems

The microwave frequency band at 25-70 GHz is being considered for fiber radio systems in order to avoid spectral congestion at lower frequencies. These systems may employ hybrid optical/microwave systems since this combination of optics and microwave techniques offers a variety of advantages [4]. First of all, the low fiber attenuation for feeding the base stations is exploited given that transmission of higher radio frequency (RF) carriers by microwave classical means is limited by the attenuation, the noise factor, and microwave circuit dynamics. Concerning the radio link, addition of RF atmospheric attenuation to free space attenuation allows better cell orthogonality and reduces multi-user interference inside a given cell. The use of high RF carriers result then, in a network having a reduced cell-size with more subscribers per area [5]. Moreover, a high frequency-reuse factor is obtainable together with a reduced RF power yielding negligible electromagnetic interference (EMI).

All this leads to a picocellular system having numerous low-cost base stations without microwave oscillators and modulators, and with superior RF properties.

Fiber radio systems, shown in Figure 0.2, comprise microwave components for the radio link between the mobile station (MS) and the base station (BS), and optical components for the optical link between the BS and the control station (CS). These optical components are in charge of the broadband low-loss connection, the generation, and control of the RF signals. Especially in 60 GHz picocellular systems, the costs of the numerous BS's should be kept as low as possible. Therefore, the generation and control of the microwave signals should be carried out in a centralized manner in the CS, thus obviating the need for microwave oscillators and modulators in the BS's. In this concept, further functions such as frequency selection and stabilization, signal processing, and network management are performed remotely in the CS. Despite the possibly rough environment of the base station, RF carriers with superior characteristics can be optically generated.

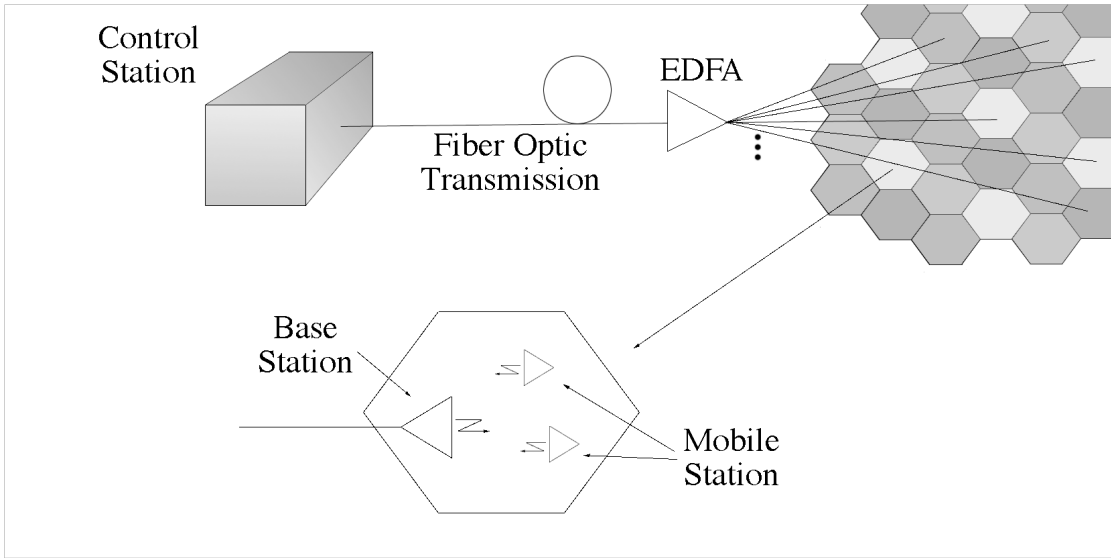


Figure 0.2: A fiber radio system where remote generation and control are carried out at the control station.

0.3 Exploration of possible techniques

Once having clear that the best solution to fulfill the increasing bandwidth demand is a hybrid optical/microwave network, it is necessary to explore available technologies and identify key problems. In a picocellular system, independently of the services provided, large bandwidth signals will be delivered to numerous base stations. For example, an intelligent vehicle highway system, which will prevent the problem of road accidents and traffic congestion, will require distribution of 60 GHz signals to more than a 1000 remote antenna units (e.g. at traffic lights) that are dispersed over an area with radius just above 10 km [6]. Available standard optical technologies do not permit distribution of signals in this band in a cost-effective way. Innovative solutions have to be proposed keeping in mind that the 1550 nm optical band is mandatory in order to take advantage of erbium-doped fiber amplifiers (EDFA).

The simplest method one can think of is direct modulation of laser diodes, but this is limited by laser bandwidth, chirp and fiber dispersion [7]. Different heterodyne methods have been investigated for the optical generation of microwave signals. In principle, the optical waves can be emitted either from two separate lasers [8], [9] or from a single laser by use of special arrangements. Techniques comprising a single laser include the modulation-sideband-technique [10], dual mode laser [11], externally modulated lasers [12], and mode-locked lasers [13]. It should be noted that most of these techniques require fiber dispersion compensation [14].

There are many other techniques enabling optical generation of microwaves, but are mainly variations of those previously mentioned. For example, instead of using the mode-locked laser technique, self-sustained pulsation lasers could be used to frequency modulate a subcarrier able to reach 100 GHz [15]. Another technique utilizes a phase-locked loop to force a heterodyne signal to track the phase of a reference signal [16]. Still another optical microwave source called an optoelectronic oscillator is based on Brillouin scattering in optical fibers [17]. Following, a brief description of the principal techniques for optical generation of microwaves will be given, outlining their major advantages and drawbacks.

0.3.1 Direct Modulation of Semiconductor Lasers

Direct laser diode modulation, because of its simplicity and wide bandwidth capability, is the most attractive method for generation of a microwave signal at a remote photodetector. For short links the maximum microwave frequency, the link gain, and signal to noise ratio (S/N) are limited by the laser diode characteristics. Basically, the modulation bandwidth is limited by the relaxation oscillation frequency [18]. Above this frequency, the modulation response falls as $1/f_m^2$, where f_m is the modulation frequency. Although exceeded in experimental devices [19], the typical modulation bandwidth of a high-speed 1550 nm laser diode is ~20 GHz and represents the practical upper frequency limit. The maximum link gain is limited to -15 dB by the laser slope efficiency and by the responsivity of the photodetector. The performance depends on the laser intrinsic noise (RIN), which has a resonance at a frequency just below the 3 dB modulation bandwidth. The typical S/N is 50 dB at 18 GHz for 0 dBm drive power and a 1 MHz detection bandwidth [7]. An undesirable feature of direct modulation is the presence of harmonics due to the nonlinearities in the dynamics of laser power vs. current response. In the frequency range of 5 to 15 GHz, the second harmonic to fundamental microwave power ratio is typically -10 dB but can be as little as -5 dB for reasonable (30%) modulation depth and laser bias (I_{th}). Another disadvantage is the non-flat frequency response, which either has to be compensated for or, in certain applications such as frequency response measurements of optoelectronic components, must be calibrated out. Furthermore, the microwave signal is carried as a lower and an upper sideband on the optical carrier. Due to fiber chromatic dispersion and the large frequency offset between the sidebands and the optical carrier, the phase of each of the spectral components of the transmitted optical signal experiences a differential change. After detection, this results in a power reduction of the recovered microwave signal and thereby a reduction of its carrier to noise ratio C/N .

0.3.2 Modulation Sideband Technique

The modulation sideband technique for optically generating microwaves is based on a self-heterodyne detection scheme. The main interest behind this optical source configuration

is its simplicity and low cost. It can support a single very high data-rate channel. A conventional semiconductor laser is externally modulated with a high bandwidth Mach-Zehnder optical modulator. As a result of optical double sideband suppressed carrier modulation, two optical carriers are generated with a frequency difference equal to twice the drive frequency of the modulator. This corresponds to the desired frequency of the microwave carrier. The data modulation is directly applied to the modulator drive signal using a modulation scheme like frequency shift keying (FSK) [10]. This results in an optical output spectrum with two carriers that are frequency shift keyed. The optical signals are transported by a fiber network to the BS where coherent mixing of the carriers generates the electrical microwave signal bearing the FSK data signal.

0.3.3 Dual Mode Laser

Dual-mode multi-section long-cavity distributed feedback (DFB) semiconductor lasers have been developed to generate microwave frequencies up to the 60 GHz range [11]. Two optical modes produced at the output of the device have a frequency separation equal to the desired microwave carrier. The beat signal is produced at a wideband photodetector. To reduce beat phase noise, phase locking of the beat signal is obtained by applying a drive signal to one of the laser sections at a subharmonic of the desired signal. This is a straightforward way of obtaining pure microwaves using a single semiconductor laser chip. Nevertheless, data transmission is not evident. Direct intensity modulation of the laser diode will provoke a simultaneous optical modulation on both modes and a square-law photodetector would eliminate the data PM and FM modulation.

0.3.4 External Modulation Technique

From the viewpoint of cost effectiveness, the external modulation scheme is seemingly a very good solution because of simple configuration [20]. This technique requires a specially designed electroabsorption (EA) modulator with high-efficiency around the desired microwave carrier. This means that a microwave band modulator is required but a wide

bandwidth is not necessary. To overcome chromatic fiber dispersion such as the signal modulation fading phenomenon due to an optical double sideband (DSB) modulation format [21], an optical single sideband (SSB) filtering technique [22] can be adopted. A balanced optical modulation scheme and either a fiber Bragg grating or a Fabry–Perot etalon filter are used to produce the optical SSB signal. The use of optical SSB filter makes possible long standard SMF transmissions (>50 km). Another way to overcome dispersion problems is the use of chirped fiber gratings that for a given distance and carrier frequency a given dispersion compensation must be specified. Although high frequencies can be obtained using this technique (>630 GHz), several drawbacks are accompanied: polarization dependent, nonlinear response, limited modulation depth, additional optical loss, cost, bias drift, frequency chirping and limited power.

0.3.5 Mode-Locked Lasers

In this system, two modes are filtered out from the output of a mode-locked laser and heterodyned at a photodetector. The frequency of the generated microwave corresponds to the longitudinal mode spacing. Active mode locking reduces phase noise and provides a mean to control the generated frequency [13]. Fiber dispersion immunity and full modulation depth are inherent to this technique. The mode-locked laser does not need a mm-wave oscillator but only a low-frequency microwave source. Nevertheless, complex laser structures remain a major drawback.

0.3.6 Sideband Injection Locking Technique

This technique consists in optical heterodyning the signals of two lasers frequency-separated by the desired microwave frequency. The phase noise caused by the spontaneous emission of photons in the laser cavity is cancelled by sideband injection locking with a master laser [8]. The master laser is sub-harmonically modulated so that only low-cost and commercially available microwave components and laser-diodes are required in the CS. Although its implementation is somewhat complex, the technique offers a variety of

advantages. A great flexibility regarding the microwave frequency is offered since it is given by the frequency spacing of the two lasers. Frequencies from some megahertz up to the terahertz-region are possible. Due to the low phase noise, RF carriers with sub-hertz linewidths can be obtained [5] and bandwidth efficient broadband modulation formats can be applied. The data modulation is simply carried out directly via the laser injection current. In contrast to other optical microwave generation techniques, a further advantage of this method is that the optical power is concentrated only in two optical waves. Thus, it represents a very efficient microwave generation technique, which is also suitable for long distances without degradation due to fiber dispersion. For multi-channel operation, further slave lasers with different optical frequencies are added in optical transmitter. The injection-locked lasers represent a multifunctional element: they act as an optical narrow-band filter, as an amplifier and as a phase modulator with a modulation speed determined by the maximum system bit rate.

0.4 Thesis Overview

Given the undeniable importance the telecommunications market has been acquiring in the past two decades, a thorough examination of available resources to satisfy the increasing bandwidth demand is in place. The numerous advantages of the sideband injection locking technique for optical generation and control of microwaves suggest further scrutiny of the physical mechanisms involved in this technique. Obviously, complete comprehension of the device physical behavior is not sufficient as an objective. A full performance assessment in terms of practical design issues has to be added.

Basically, the topic of this work lies at frontier of the optical and microwave communications fields; a combination of fields frequently called microwave photonics. With the hope to move forward this field, the study of injection locking of distributed feedback semiconductor lasers applied to fiber radio access systems is presented. To accomplish this, an original injection-locked laser model backed up by novel measurement experiments was developed to optically generate and control microwaves.

In the first chapter an introduction to optical heterodyne techniques for microwave generation is given. The choice for heterodyne detection scheme for use in fiber radio access systems was justified earlier. Further insight on this choice is given by a feasibility analysis characterizing link performance in terms of design parameters, such as the dual-frequency optical transmitter, transmission distance, fiber dispersion, differential delays, and carrier frequency. The influence of these parameters on signal to noise ratio, phase noise, bit error rate, and the longest possible transmission distance will be discussed as well. In particular, close attention is given to the output power of the photodetector, which plays an important role on cost reduction and link gain. Finally, the different candidate photodetectors are briefly discussed highlighting the advantages and drawbacks of each.

In chapter two, a semiconductor laser model is developed to accurately describe optical injection in distributed feedback semiconductor lasers. In view of its potentiality in numerous applications it is important to fully describe. Different structures are discussed so as to understand the capabilities of the model. A stability analysis reveals a precise determination of the locking range and the dependency on intrinsic characteristics is established. Large-signal dynamical simulations are carried out using the finite difference method. Applications of the model are finally studied.

In chapter three, an experimental study of the distributed semiconductor lasers used through the thesis is presented. First, the static, noise and modulation characteristics are described through different measurement schemes. Next, the experimental results concerning injection locking of DFB semiconductor lasers and the stabilization procedure are given. An optical low-coherence reflectometer (OLCR) is finally used to measure optically induced index changes.

In chapter four, optically generated microwaves using the sideband injection locking technique is experimentally investigated. After presenting the experimental procedure, conditions on the modulation properties of the master laser are established. Then, sideband injection locking is compared to fundamental peak locking with the objective to find stability conditions. Finally, optical generation of microwaves is experimentally demonstrated and RF properties are discussed.

0.5 References

- [1] O. Golda, "Interactive broadband applications, the role of IN," Intelligent Network Workshop, IN '96., IEEE , 1996.
- [2] L. Marchesotti, L. Marcenaro, C. Regazzoni, "A video surveillance architecture for alarm generation and video sequences retrieval Image," International Conference on Processing. 2002. Proceedings. 2002 , Volume: 1 , 2002 Page(s): 892 –895
- [3] D. Budimir, B. Milovanovic, V. Stankovic, "Broadband wireless systems and components-an overview," Telecommunications in Modern Satellite, Cable and Broadcasting Services, 1999. 4th International Conference on , Volume: 1 , 1999 Page(s): 54 -61 vol.1
- [4] R.-P. Braun, G. Grosskopf, D. Rohde, and F. Schmidt, "Low-phase-noise millimeter-wave generation at 64 GHz and data transmission using optical sideband injection locking," IEEE Photon. Technol. Lett., vol. 10, pp. 728–730, 1998.
- [5] R.-P. Braun, "Fibre radio systems, applications and devices," 24th European Conference on Optical Communication, 1998., Vol. 2 , 1998, pp. 87 -119.
- [6] H. Schumuck, R. Heidemann et R. Hofstetter, "Distribution of 60 Ghz signals to more than 1000 base stations", Elec. Lett., vol 30, pp. 59-60, 1994.
- [7] L. Goldberg, R.D. Esman, K.J. Williams, "Optical techniques for microwave generation, transmission and control," in IEEE MTT-S Int. Microwave Symp. Dig., Microwave Symposium Digest, 1990., IEEE MTT-S International , 1990 Page(s): 229 - 232 vol.1
- [8] L. Goldberg, H. F. Taylor, J. F. Weller, and D. M. Bloom, "Microwave signal generation with injection locked laser diodes," Electron. Lett., vol.19, pp. 491–493, 1983.

-
- [9] R.-P. Braun, G. Grosskopf, D. Rohde, and F. Schmidt, "Fiber optic millimeter-wave generation and bandwidth efficient data transmission for 18–20 and 60 GHz-band communications," in Proc. Int. Top. Meet. Microwave Photonics, MWP'97, Duisburg, Germany, Sept. 1997, pp. 235–238, paper FR2-5.
- [10] H. Schmuck and R. Heidemann, "Hybrid fiber-radio field experiment at 60 GHz," in Tech. Dig. 22th Eur. Conf. Optical Communication, (ECOC'96), Oslo, Norway, Sept. 1996, vol. 4, pp. 59–62, paper ThC. 1.2.
- [11] D. Wake, C.R. Lima et P.A. Davies, "Optical Generation of Millimeter-Wave Signals for Fiber-Radio Systems Using a Dual-Mode DFB Semiconductor Laser", IEEE Trans. Microwave Theory Tech., vol 43, pp. 2270-2276, sept. 1995.
- [12] T. Kuri, K. Kitayama, A. Stohr, Y. Ogawa, "Fiber-optic millimeter-wave downlink system using 60 GHz-band external modulation", Journal of Lightwave Technology, Vol. 17, May 1999 pp. 799 -806
- [13] C. H. v. Helmolt, U. Krüger, K. Krüger, and G. Grosskopf, "A mobile broadband communication system, based on mode locked lasers," IEEE Trans. Microwave Theory Tech., vol. 45, pp. 1424–1430, Aug. 1997.
- [14] A. J. Seeds, "Microwave Photonics," IEEE Trans. Microwave Theory Tech., Vol?. 50, march 2002, pp. 877-887.
- [15] X. Wang, G. Li, C. S. Ih, "Microwave/Millimeter-Wave Frequency Subcarrier Lightwave Modulations Based on Self-Sustained Pulsation of Laser Diode", IEEE J. Light. Technol., vol 11, pp. 309-315, 1993.
- [16] Z.F. Fan et M. Dagenais, "Optical Generation of a Megahertz-Linewidth Microwave Signal Using Semiconductor Lasers and a Discriminator-Aided Phase-Locked Loop", IEEE Trans. Microwave Theory Tech., vol 45, pp. 1296-1300, août 1997.

-
- [17] X.S. Yao, "High-quality microwave signal generation by use of Brillouin scattering in optical fibers", *Optics Lett.*, vol 22, pp. 1329-1331, sept. 1997.
- [18] G. P. Agrawal and N. K. Dutta, *Semiconductor Lasers*, 2nd ed. New York: Van Nostrand Reinhold, 1993.
- [19] Weisser, S., Larkins, E.C.; Czotscher, K., Benz, W., Daleiden, J., Esquivias, I., Fleissner, J., Ralston, J.D., Romero, B., Sah, R.E., Schonfelder, A., Rosenzweig, J., "Damping-limited modulation bandwidths up to 40 GHz in undoped short-cavity In/sub 0.35/Ga/sub 0.65/As-GaAs multiple-quantum-well lasers", pp. 608 –610.
- [20] K. Kitayama, "Architectural considerations of radio-on-fiber millimeter-wave wireless access systems," in *Proc. 1998 URSI Int. Symp. Signals, Systems, and Electron. (ISSSE'98)*, Pisa, Italy, Invited Paper, Sept. 1998, pp. 378–383.
- [21] K. Kitayama, "Optical DSB signal based mm-wave fiber-radio system using external modulation technique: ultimate performance," *International Topical Meeting on Microwave Photonics*, 1999 pp. 53 -56
- [22] J. Park, W. V. Sorin, and K. Y. Lau, "Elimination of the fiber chromatic dispersion penalty on 1550 nm millimeter-wave optical transmission," *Electron. Lett.*, vol. 33, no. 6, pp. 512–513, Mar. 1997.

Chapter 1: **GENERALITIES OF THE HETERODYNE DETECTION SCHEME**

The microwave photonics field is developing to accomplish RF tasks with optical techniques in a more efficient way, with less cost and with increased capacity. Several transmission experiments incorporating optical/microwave hybrid techniques have been reported ([1] and references within). Nevertheless, numerous questions remain unanswered, particularly on how device characteristics specifically affect link performance and on what techniques favor different applications in fiber radio access systems. The objective of this chapter is then to clarify what the capabilities of a heterodyne detection link are in function of the device parameters and the desired RF tasks. Every system component is equally important so recent photodetector technology will be discussed as well.

1.1 Heterodyne Detection Scheme

Fiber radio access systems using a remote heterodyne detection scheme are based on the simultaneous transmission of two or more optical signals having a strong phase correlation. The optical signals are offset by the desired microwave frequency. This can be achieved for instance, by using any of the heterodyne techniques described in the introduction. It is assumed that the lasers are located at the control station. Otherwise, having a laser at the control station and a laser acting as a local oscillator at the base station would impose frequency control and polarization matching at the receiver, thus elevating the cost of the base station.

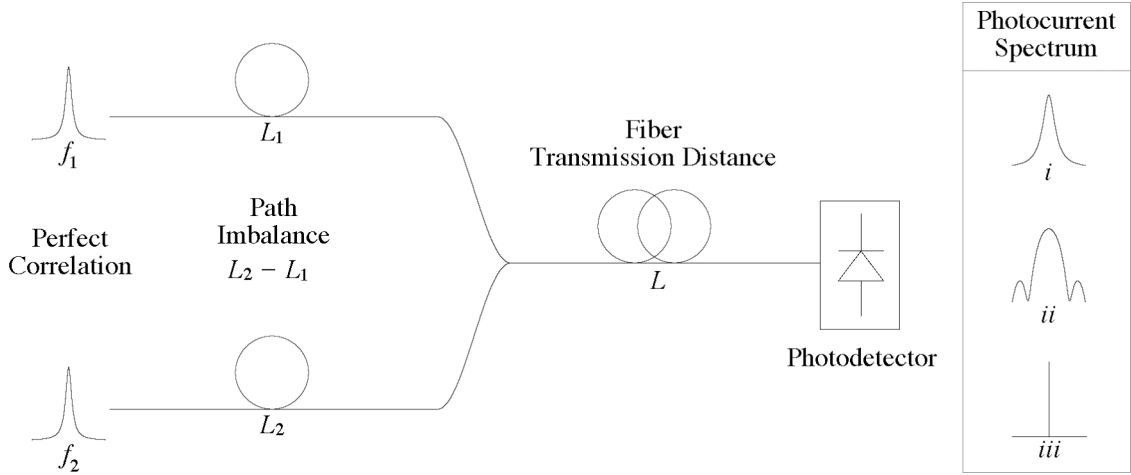


Figure 1.1: Fiber optic transmission of two signals showing the possible photocurrent power spectrums.

In Figure 1.1 the general heterodyne detection scheme is shown. Before transmission of both carriers through an optical fiber, each carrier often propagates through separate paths in the dual-frequency optical transmitter. As a result, the path imbalance, $\Delta L_{\text{path}} = L_2 - L_1$, causes a delay between both signals given by

$$\tau_{\text{path}} = \frac{L_2 \cdot n(\omega_2) - L_1 \cdot n(\omega_1)}{c}, \quad \text{Eq. 1.1}$$

where n is the refractive index of the unbalanced path and c the speed of light in vacuum. It should be noticed that this delay could be either positive or negative. Due to chromatic fiber

dispersion, each carrier propagates at different speeds and, after a transmission distance L , another delay is added, which is expressed as

$$\tau_{\text{disp}} = D \cdot L \cdot \frac{\lambda^2}{c} \cdot f_{\text{mw}}, \quad \text{Eq. 1.2}$$

D is the fiber dispersion taken as 17 ps/km · nm for standard single-mode fibers, λ the mean optical wavelength, and $f_{\text{mw}} = |f_2 - f_1|$ the microwave carrier frequency. The master laser, from which the two signals are derived in the dual-frequency optical transmitter, is assumed to have a Lorentzian-line power spectrum with a full-width at half-maximum (FWHM) $\Delta\nu_m = R_{\text{sp}}(1 + \alpha_H)/(4\pi P_0)$ [2], where R_{sp} is the rate of spontaneous emission coupled to the lasing mode [3], α_H is the linewidth enhancement factor [4], and P_0 is the average output power per facet. Under these assumptions, the single-sided photocurrent spectrum is calculated following Gallion *et al.* [5], by taking the Fourier transform of the generated current autocorrelation function to yield:

$$S_i(f) = \alpha^2 \langle i \rangle^2 \exp(-2\pi\Delta\nu_m \tau_0) \delta(f) + \alpha^2 \langle i \rangle^2 \frac{\Delta\nu_m / \pi}{\Delta\nu_m^2 + f^2} \cdot \left\{ 1 - \exp(-2\pi\Delta\nu_m \tau_0) [\cos(2\pi f \tau_0) + \Delta\nu_m \tau_0 \text{sinc}(2\pi f \tau_0)] \right\} \quad \text{Eq. 1.3}$$

where f represents the offset from the microwave carrier, $\tau_0 = |\tau_{\text{path}} + \tau_{\text{disp}}|$ the total delay between the optical signals [6], α the relative weight between the amplitudes of each field, and $\langle i \rangle = (\eta \cdot e / h\nu_0) \langle E^*(t)E(t) \rangle$ is the photocurrent mean value; η , e , h , and ν_0 , representing respectively, the detector quantum efficiency, the electron charge, the Planck constant, and the optical frequency. The sign of the path imbalance delay depends on whether it works in the same or opposite direction as the dispersion-induced delay. The laser field is modeled as a quasi-monochromatic field stabilized in amplitude $E(t) = E_0 \exp j[\omega_0 t + \phi(t)]$. The total detected field is then taken as the superposition of this field and an image of itself delayed and frequency shifted, $E_T(t) = E(t) + \alpha E(t + \tau_0) \exp(j2\pi f_{\text{mw}} t)$.

From Figure 1.1, three cases can be distinguished according to the total delay induced through the transmission paths. Case i refers to a large delay with respect to the laser

coherence time ($\tau_0 > 1/\Delta\nu_m$), and the resulting photocurrent power spectrum is a Lorentzian shaped curve designated by the second term in Eq 1.3. Its full width at half maximum is equal to twice the master laser linewidth. This is due to complete decorrelation of both signals. For intermediate values of the total delay, $0 < \tau_0 < 1/\Delta\nu_m$ (case *ii*), the output spectrum results in a delta Dirac function superimposed to a sinc function whose spectral zeros are separated by $1/\tau_0$. Finally in case *iii*, when the total delay is zero, both complex amplitudes are perfectly phase correlated so a delta dirac function results.

1.1.1 Differential Delay Influence on Phase Noise

The influence of the differential delay on the carrier to noise ratio C/N and on the phase noise determines the link performance. It is seen from the first term in Eq. 1.3, that an increase in a differential delay results in a decrease of the C/N . Simultaneously, this is accompanied by an increase of the phase noise (second term). For several values of the laser linewidth, the penalty induced on the C/N is represented in Figure 1.2. It can be concluded that for a conventional DFB semiconductor laser, having a linewidth $\Delta\nu \sim 10$ MHz, only a small penalty is induced for long differential delays ($\sim 10^4$ ps). In other words, for a long transmission distance, the chromatic fiber dispersion induces only a small penalty on the C/N .

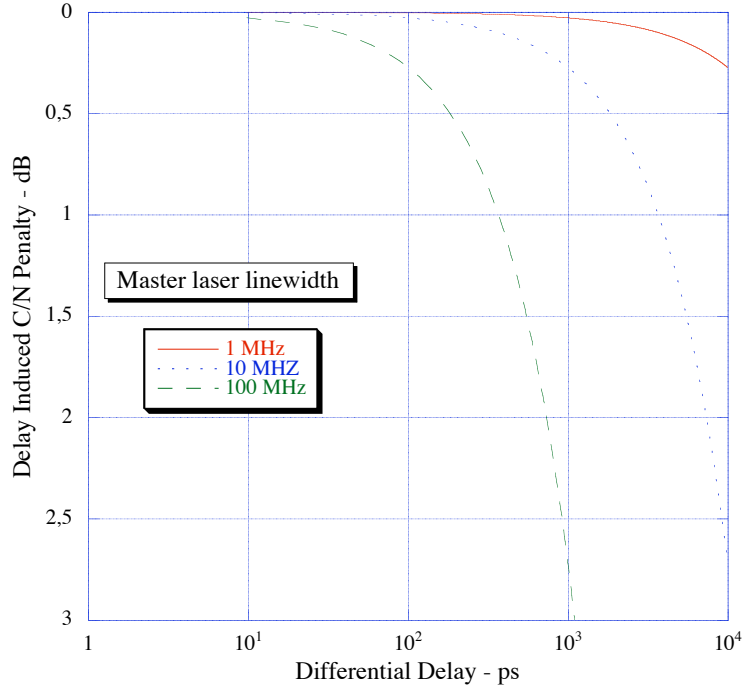


Figure 1.2: Delay induced penalty on the carrier to noise ratio.

To study the influence of the differential delay on phase noise, it is best to consider the phase fluctuation spectrum of the generated RF carrier rather than its corresponding power spectrum. Assuming a Lorentzian-line power spectrum for the master laser, the phase fluctuation spectrum is expressed as [7]

$$S_{\phi}(f) = \frac{2\Delta\nu_m}{\pi f^2} [1 - \cos(2\pi f \tau_0)] \quad \text{Eq. 1.4}$$

This spectrum is shown in Figure 1.3, as a function of the frequency with the total differential delay as a parameter. For an infinite differential delay, the $1/f^2$ shape resulting from the Lorentzian spectrum is clearly identified. For intermediate values of the differential delay, the sinc shape is observed with spectral zeros distanced by $1/\tau_0$. And for a small differential delay, the spectrum is fairly constant at small frequency values due to the large separation between spectral zeros. In this case, the filtering performed in the microwave receiver would remove a significant amount of the delay induced phase noise.

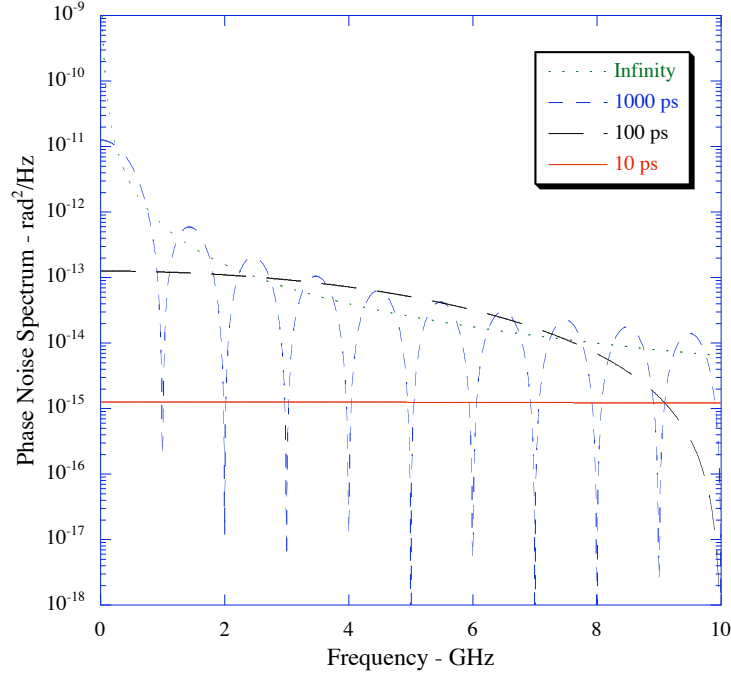


Figure 1.3: Phase noise spectrum in function of the frequency.

To calculate the exact amount of delay induced rms phase noise σ_ϕ , the receiver noise bandwidth B_n should then be taken into account giving

$$\begin{aligned}
 (\sigma_\phi)^2 &= \int_0^{B_n} S_\phi(f) df \\
 &\approx 2\pi\Delta\nu_m B_n \tau_0^2
 \end{aligned}
 \tag{Eq. 1.5}$$

This result is only valid for $B_n \ll 1/\tau_0$ where the phase fluctuation spectrum is approximated as constant. The rms phase error is represented in Figure 1.4 as a function of the differential delay with the product of the laser linewidth and noise bandwidth as a parameter. It is seen that the phase error increases with an increasing differential delay or with an increasing laser linewidth times noise bandwidth product. In practical systems, for example the INTELSAT earth station [8] where QPSK modulation is used, the maximum allowable rms phase error is 2.2° . The differential delay is shown in Figure 1.5 as a function of the distance times carrier frequency product with the path imbalance delay as a parameter. A wavelength of 1550 nm and a dispersion of 17 ps/km/nm were used. It is observed that the delay increases with transmission distance and carrier frequency. A positive path imbalance delay results in a delay floor equal to its value. The total differential delay can be cancelled for a given distance times carrier frequency product as can be seen for a negative path imbalance delay. Consequently, an intentionally induced path imbalance delay can be used to compensate the

dispersion delay for a fixed value of the carrier frequency times transmission distance product. The total differential delay is then cancelled leading to a null phase noise. Figure 1.6 shows the path imbalance in function of the transmission distance with the carrier frequency as a parameter. It is seen that a path imbalance of a few centimeters (< 25 cm) suffices to compensate the dispersion induced delay for long transmission distances (~100 km). Even as the microwave carrier frequency increases up to 60 GHz, the compensation distance required remains less than 25 cm.

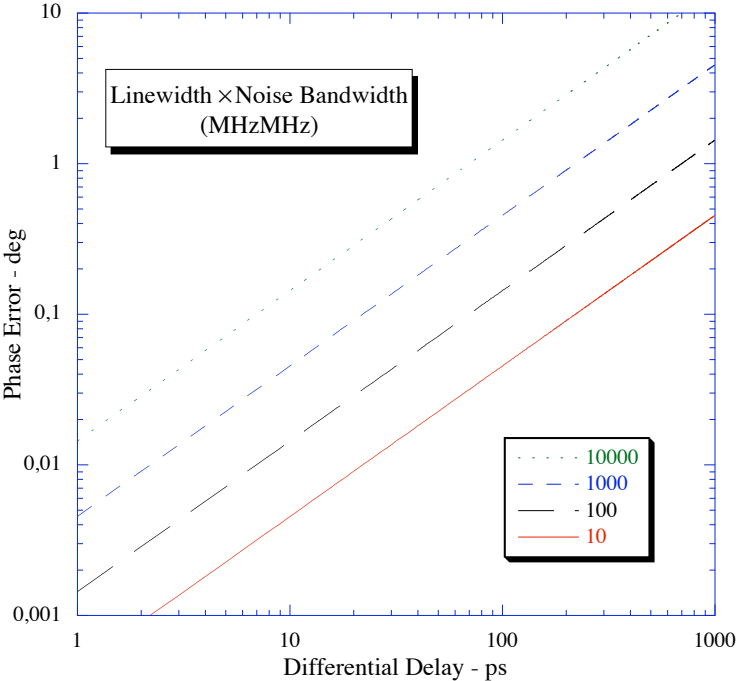


Figure 1.4: Phase error in function of the total differential delay.

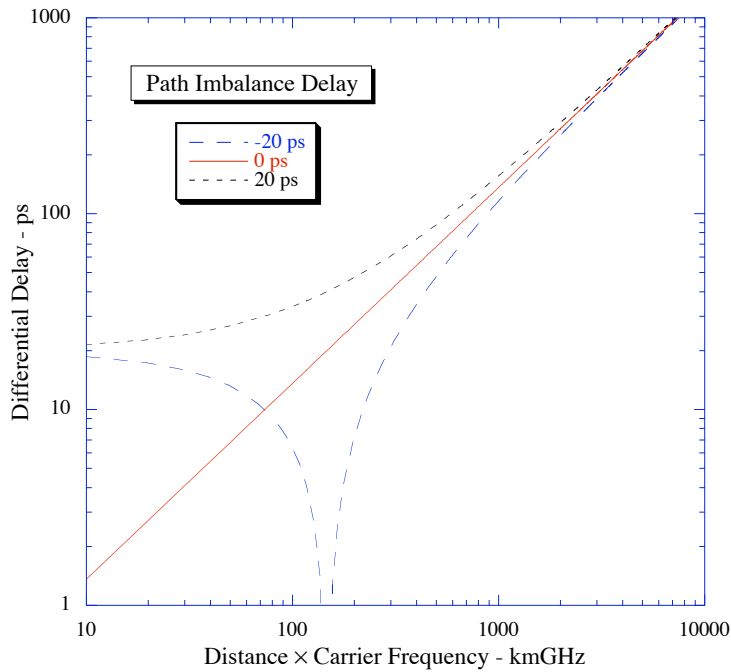


Figure 1.5: Total differential delay in function of the transmission distance and carrier frequency product.

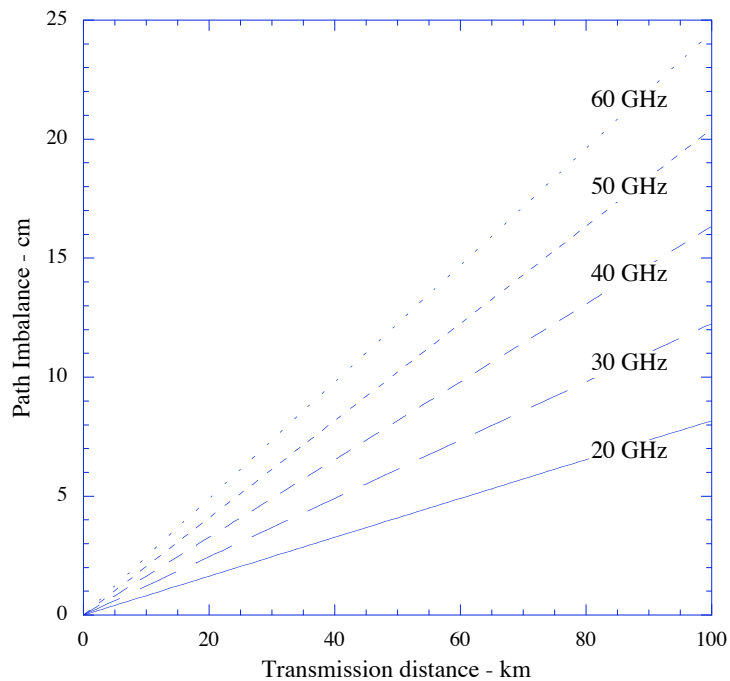


Figure 1.6: Path imbalance needed for fiber dispersion compensation.

Even though phase noise can be eliminated under certain conditions, the phase diffusion is a random process so its probability density should be taken into account in order to quantify its influence on link performance in function of the design parameters. Furthermore it will be seen how sensitive the phase noise effect is to fiber dispersion.

1.1.2 Bit Error Rate Analysis

The bit error rate (BER) in the described link will now be analyzed for the m-ary phase shift keying (M-PSK) modulation format. Assuming that a Gray code is used for symbol mapping and that the phase diffusion is sufficiently low that the probability of a symbol error P_{sym} only results in a single bit error, the bit error rate is given by:

$$BER = \frac{P_{\text{sym}}}{\log_2 M}. \quad \text{Eq. 1.6}$$

A symbol decision error is made when the receiver detects a phase that falls outside the range $-\pi/M \leq \phi \leq \pi/M$ relative to its ideal value. The contributions to phase noise are basically considered to be additive Gaussian noise and carrier phase noise [6]. The symbol error probability is obtained by weighing the mean phase error by its probability:

$$P_{\text{sym}} = 1 - \sum_{k=0}^{M-1} P_k \int_{-\pi/M}^{\pi/M} p(\phi) d\phi \quad \text{Eq. 1.7}$$

where P_k is the probability of a phase change $\Delta\phi = 2\pi/M$ during a symbol transition. Assuming negligible symbol interference and equiprobable m-ary symbols, this probability is easily seen to be:

$$\begin{aligned} P_{k \cdot \Delta\phi | k=0} &= 1/M, \\ P_{k \cdot \Delta\phi | k \neq 0} &= 2(M-k)/M^2. \end{aligned} \quad \text{Eq. 1.8}$$

The probability density function of ϕ depends on additive Gaussian noise as well on the residual phase noise of the microwave carrier. The probability density function for the additive Gaussian noise is given by [9]

$$p_1(\phi) = \frac{\exp^{-\gamma}}{2\pi} \left(1 + \sqrt{2\gamma} \cos \phi \cdot \exp^{\gamma \cos^2 \phi} \cdot \int_{-\infty}^{\sqrt{2\gamma} \cos \phi} \exp^{-x^2/2} dx \right) \quad \text{Eq. 1.9}$$

where γ is the carrier to noise ratio of the M-PSK carrier signal. For simplicity, it is assumed that the residual carrier phase noise has a Gaussian probability density function given by:

$$p_2(\phi) = \frac{1}{\sqrt{2\pi}\sigma_\phi} \exp^{-\frac{\phi^2}{2\sigma_\phi^2}} \quad \text{Eq. 1.10}$$

where σ_ϕ is the rms phase error calculated previously. Since $p_1(\phi)$ and $p_2(\phi)$ are independent random processes their joint probability density function is given simply by their convolution:

$$p(\phi) = \int_{-\pi}^{+\pi} p_1(x) p_2(\phi - x) dx \quad \text{Eq. 1.11}$$

As it was previously discussed, the influence of the total differential delay on carrier to noise ratio is negligible. In the following, the carrier to noise ratio will then be taken as delay-independent for simplicity without loss of generality. The BER is shown on Figure 1.7 in function of the path imbalance for a 2 and 5 MHz laser linewidth and for different carrier to noise ratios. The generated carrier frequency used was set at 64 GHz, the transmission distance was taken as 15 km, and the receiver noise bandwidth was 200 MHz. Errorless transmissions are possible for a path imbalance between -14 and 6 cm with a 10 MHz linewidth and a 17 dB carrier to noise ratio.

The BER minimum for a given transmission distance, carrier frequency, noise bandwidth, and laser linewidth depend on the carrier to noise ratio. This is shown in Figure 1.8 for different m-ary modulation formats. A linear dependency is found with a slope approximately equal to -2. Increasing the spectral efficiency of the modulation format by two results in a penalty of 5 dB on carrier to noise ratio. This is generally a drawback in design issues which will be accounted for once decided the number of channels required for a given carrier frequency.

The width of the BER curve at 10^{-9} in Figure 1.7 is called here the dispersion compensation tolerance. It is the maximum path imbalance allowable for an errorless transmission. Figure 1.9 shows this tolerance in function of the master laser linewidth. It is seen that even for large values of the laser linewidth, the tolerance remains in the tenths of centimeter range. Remembering from Figure 1.6 that the dispersion compensation distance is less than 25 cm., an imprecision of some centimeters in the path imbalance does not change the BER drastically. So, it is relatively easy to compensate for fiber dispersion.

To really have a good grasp on how sensitive the link is on fiber dispersion, the BER was calculated for the QPSK modulation format and without a path imbalance in function of the transmission distance. This is shown on Figure 1.10 where a fixed carrier to noise ratio of 16 dB was used. It is observed that transmission distances up to 60 km keep the BER less than 10^{-10} .

Summarizing, the BER increases as the carrier to noise ratio decreases. Increasing the transmission distance or the carrier frequency results in a shift to the left of the whole BER curve of Figure 1.7. Increasing either the master laser linewidth or the receiver noise bandwidth results in a reduction of the dispersion compensation tolerance. Having analyzed the influence of every design parameter on the BER, it can be concluded that such a remote heterodyne system easily permits errorless transmissions for high frequency carriers and long transmission distances; and that it is sufficiently robust to fiber dispersion. Although, close attention has to be given to the true delays which ultimately limits the system performance.

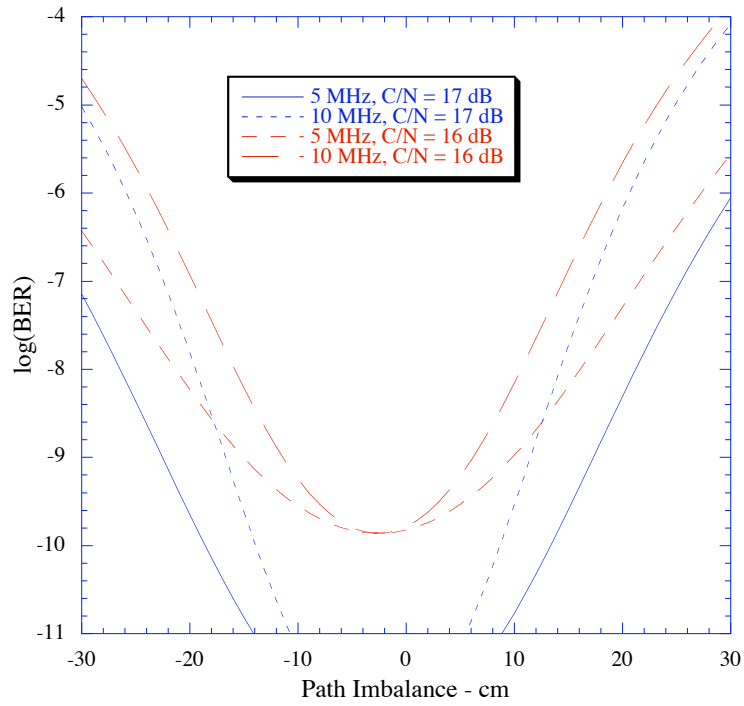


Figure 1.7: Bit error rate in function of the path imbalance for a 15 km transmission distance.

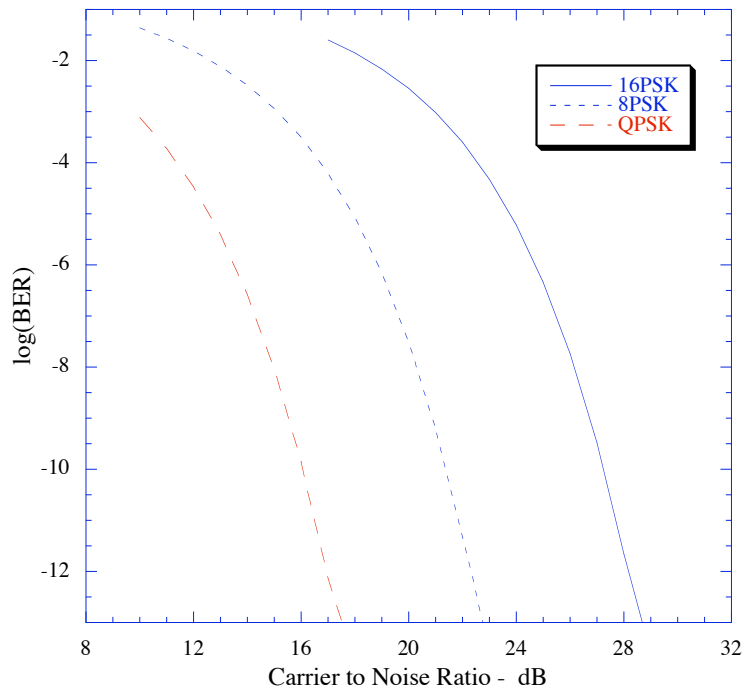


Figure 1.8: Bit error rate in function of the carrier to noise ratio for different modulation formats.

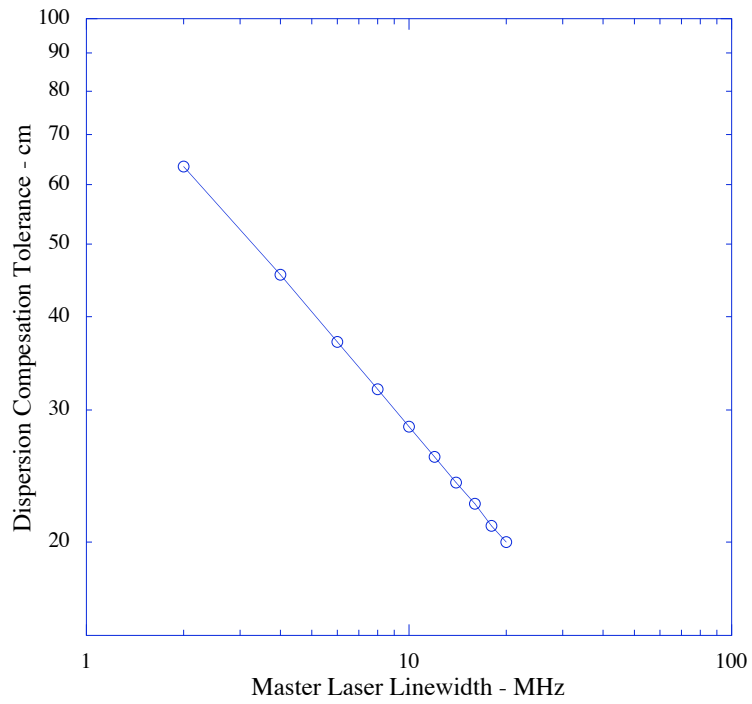


Figure 1.9: Dispersion compensation tolerance at BER of 10^{-9} .

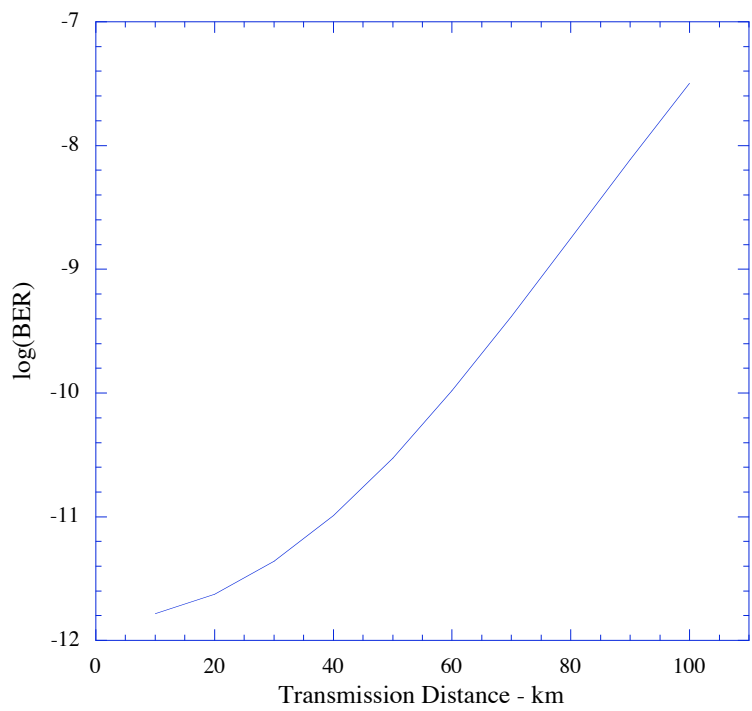


Figure 1.10: Bit error rate in function of the transmission distance for a carrier to noise ratio of 16 dB and without dispersion compensation.

1.1.3 RF Output Power

A basic requirement in a hybrid optical/microwave link is to get a high RF output power at the base station [10]. A simplified diagram of the heterodyne detection link is represented in Figure 1.11 where the quantities necessary to calculate the RF output power are shown.

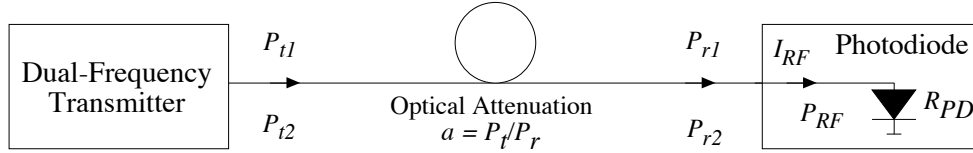


Figure 1.11: Heterodyning at the photodiode

The photocurrent mean value, in terms of the transmitted mean optical powers P_{t1} and P_{t2} of both signals in the dual-frequency optical transmitter, is written as:

$$\langle i \rangle = I_{RF} = \left(\eta \cdot \frac{e}{h \cdot \nu} \right) \cdot 2 \cdot \sqrt{P_{t1} \cdot P_{t2}} \cdot \frac{1}{a} \quad \text{Eq. 1.12}$$

The term in parenthesis is just the detector responsivity R and a is the fiber attenuation. An ideal photodetector has a maximum responsivity of 1.25 A/W for a wavelength of 1550 -nm. Realistic values of the responsivity of different photodetectors will be discussed in the next section. The RF output power at the photodiode is calculated by including the load resistance R_{PD} of the photodiode, typically equal to 50Ω , and using the rms value of the photocurrent to give,

$$P_{RF} = 2 \cdot P_{t1} \cdot P_{t2} \cdot R^2 \cdot R_{PD} \cdot \frac{1}{a^2} \quad \text{Eq. 1.13}$$

If a microwave amplifier is used to amplify the photocurrent, then the RF output power should just be multiplied by the electrical gain of the amplifier. Similarly if optical amplifiers are used within the transmission fiber, the RF output power should be multiplied by the square of the optical gain of the amplifier. For a given total transmitted power, the optic/microwave conversion efficiency is maximum when both optical carriers have the same power [5]. Assuming this, Figure 1.12 depicts the RF output power in function of the received optical power of one of the carriers. The 14 dB value comes from the fact that the RF output power depends quadratically on the responsivity. Increasing five times the detector

quantum efficiency results then on a 14 dB gain. It should be noticed that a 2-factor (3 dB) change in the received optical powers corresponds to a 4-factor (6 dB) change in the RF output power. This is because there are two optical carriers.

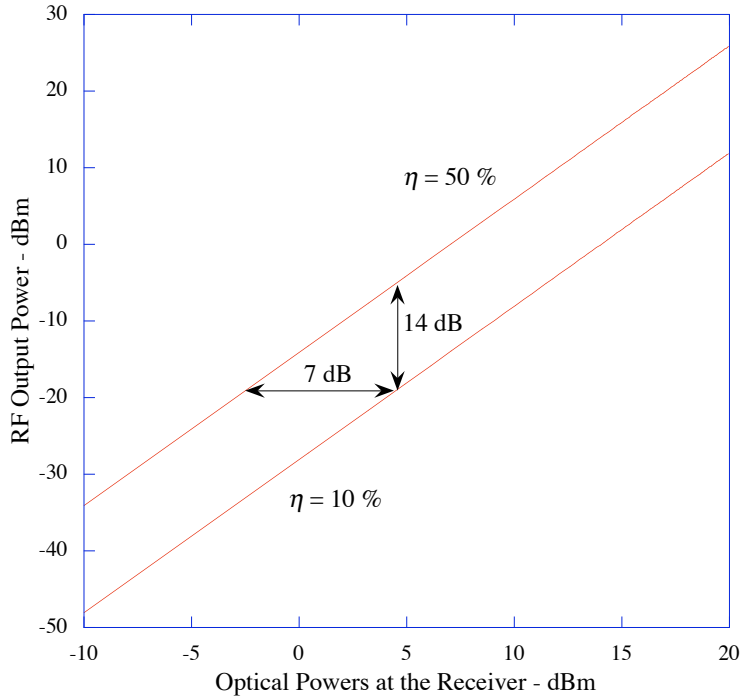


Figure 1.12: RF output power in function of the received optical power of each carrier.

In direct detection schemes, be it by using direct intensity modulation or external modulation, the link gain is independent of the supplied RF input power [11]. This is no more the case in heterodyne detection schemes. It is interesting to see then the RF output power as a function of the RF input power. If one of the lasers in the dual-frequency transmitter is directly modulated with the data signal to be transmitted, and, by assuming that the modulation results in small signal regime, its mean optical power can be written in the form, $P_{t1} = P_0 + \Delta P_{t1}$. P_0 represents the optical output power of slave laser 1 without modulation and ΔP_{t1} arises when a modulation current $I_{RF,in}$ is applied. The optical power amplitude ΔP_{t1} is related to the slope efficiency S_{laser} of the semiconductor laser by, $\Delta P_{t1} = S_{laser} \cdot I_{RF,in}$. Typical orders of magnitude of slope efficiency are in the range 0.01 – 0.10 W/A. With the larger value of the slope efficiency, the ratio of conversion is approximately 4 electron/hole pairs per photon. Factors that reduce the net efficiency of the laser from its ideal value are the two reflecting facets of the laser, Auger nonradiative recombination, waveguide absorption, scattering losses, and interfacial carrier recombination due to leakage current. The RF electrical power supplied to the laser is simply given by,

$$P_{RF,in} = \frac{I^2}{2} R_{LD} \quad \text{Eq. 1.14}$$

where R_{LD} is the resistance of the laser diode whose order magnitude lies within a few ohms. The total output power of slave laser can then be written as:

$$P_{t1} = P_0 + S_{laser} \cdot \sqrt{\frac{2 \cdot P_{RF,in}}{R_{LD}}} \quad \text{Eq. 1.15}$$

By introducing Eq. 1.15 in Eq. 1.13, it can be seen that the RF output power no more linearly depends on the RF input power. Figure 1.13 however shows that the RF output power is nearly constant for practical values of the RF input power. This occurs because the RF output power appears as the sum of two terms, one proportional to static power product of both slave lasers and one proportional to the square root of the RF input power. As a result, heterodyne detection schemes present higher sensitivity than direct detection schemes. In contrast, the link gain is strongly dependent on the RF input power (Figure 1.14). The link gain quickly decreases as the RF input power increases. For comparison purposes, the link gain of a direct detection-direct intensity modulation scheme is represented by the dotted lines. The scenario is even worse for external intensity modulation.

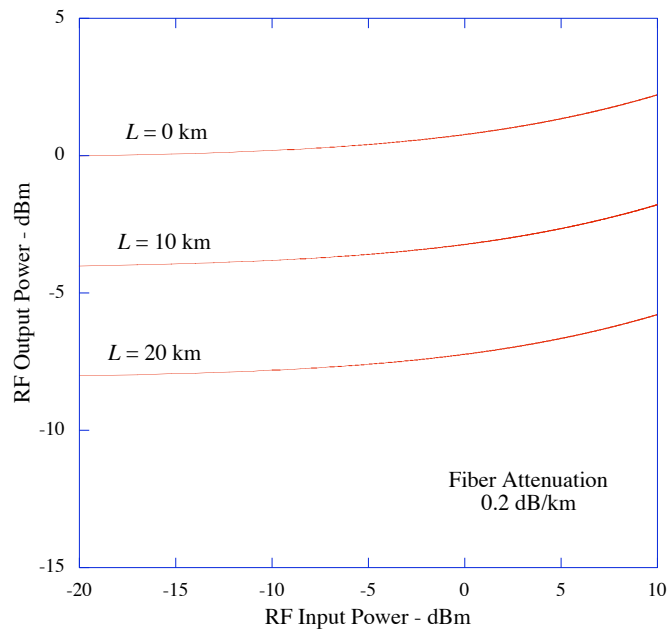


Figure 1.13: RF output power in function of RF input power for several transmission distances.

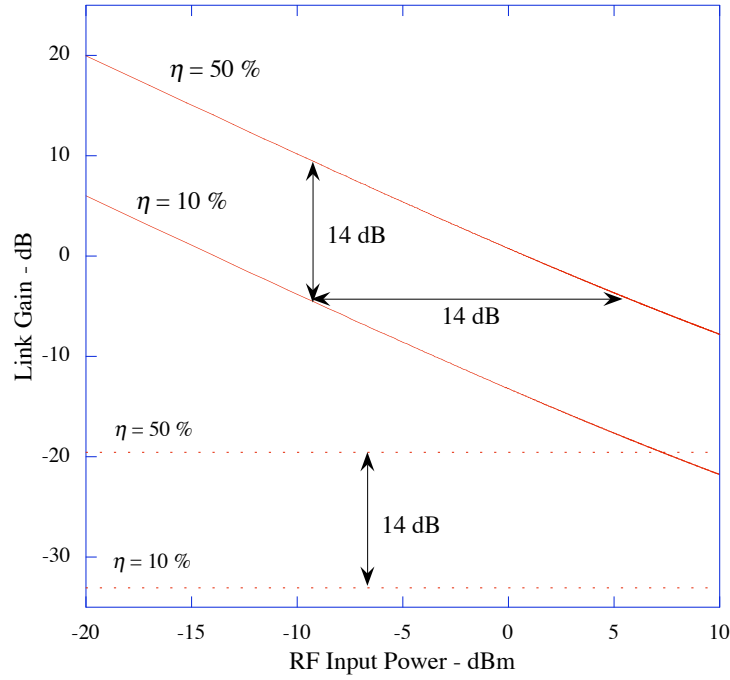


Figure 1.14: Link gain for two different detector quantum efficiencies (dotted line id for direct detection)

To achieve high RF output power several approaches are possible. First, a low-noise microwave amplifier could be used to amplify the photodiode current and this way, the output RF power will increase by G_{mw} times, the gain of the amplifier. Next, the optical powers at the receiver should be maximized. To compensate for fiber attenuation, an erbium-doped fiber amplifier can be placed in the transmission fiber, making the RF output power G_{EDFA}^2 times higher. Of course, power-handling requirements of the photodetector should be considered. The photodiode should be able to handle high input powers. Furthermore, high efficient detectors should be used so as to have a high responsivity.

1.2 Photodetectors

A key component in fiber radio access systems is the optic/microwave converter at the numerous base stations. It consists mainly of a high-speed photodetector, a low noise preamplifier, filters, and an RF power amplifier for feeding the antenna of the base stations [12]. The photodetector must be able to detect the beat signal between the slave lasers optical waves in a 3-dB bandwidth imposed by the data signal. Research on new photodetector

technology is out of the scope of this thesis. Recent research activity will, however, be discussed here with the objective to propose the most interesting solutions for photodetection in fiber radio access system applications.

1.2.1 Recent Photodiode Technology

As time goes by, photodetectors with higher electrical bandwidths and higher external quantum efficiencies are developed. For example, using an optical heterodyne technique at an optical wavelength of $1.55 \mu\text{m}$, an electrical bandwidth of 110 GHz has been measured with a waveguide p-i-n photodiode [13]. Generally, to increase the external quantum efficiency, depletion photodetectors are used. The upper limit to depletion photodiode frequency response is set by transit time effects [14] and by the depletion capacitance of the diode. Optimization involves a trade-off between speed and efficiency. Reducing the depletion width to increase the transit time limited frequency reduces the efficiency by incomplete absorption of light in geometries where light is incident normal to the junction plane. This is due to an increase of the depletion capacitance. For high-speed operation, multimode waveguide photodiodes with light incident parallel to the junction plane offer better performance, for instance a 110-GHz bandwidth with 50% quantum efficiency [15]. In addition to the trade-off mentioned above, there are conflicting requirements between speed (requiring thin active regions), power and link loss (requiring high optical power), and nonlinearity (requiring low optical power densities). The solution to circumvent the depletion capacitance limit and the nonlinearities arising from space charge density is then to (i) spread photon absorption over a thin depletion region, (ii) use multimode waveguide devices to increase efficiency, and (iii) spread photon absorption over a larger volume. All this can be done by applying, for example, traveling-wave velocity-matched design techniques [16]. To increase power-handling capabilities, use of carrier velocity overshoot effects as in the uni-traveling-carrier photodiode [17] is possible. In this structure the absorption and thin drift regions are separate and the absorption region is doped so that the holes are majority carriers. The electrons are injected at high energy into the thin drift region where they travel at overshoot velocity, thus giving rise to much reduced space charge for a given terminal current. These devices have been reported with bandwidths exceeding 300-GHz [17] and output powers exceeding 8-dBm [18]. Higher efficiencies and consequently, better system

performance are obtainable by combining photodiodes with low-noise amplifiers. Separate chips of photodiodes and amplifiers have been combined in hybrid technology, depicting a responsivity of more than 1 mA/mW of optical input power [19]. Monolithic integration of subsequent amplifiers has led to impressive demonstrations of this type of devices [20].

1.2.2 Three-port Detectors

Great efforts are carried out to develop optic/microwave converters with high efficiency using three-port devices. The device technology is based on the monolithic microwave integrated circuit (MMIC) process, which offers the advantage of integrating both the photodiode and the amplifier on the same chip, [21]. Very promising results have been obtained with devices such as, heterojunction bipolar transistor's, high electron-mobility transistors, or field effect transistors [22]. An optically generated continuously tunable 49–67-GHz microwave generation was demonstrated using high electron-mobility transistors. The optical wavelength was at 0.632-nm. The feasibility of a 50-GHz subcarrier transmission link using a heterojunction bipolar transistor photodiode in the 1.3-nm wavelength range has been demonstrated in [23]. Compared to a p-i-n photodiode, the same responsivity, flatness, and signal-to-noise were obtained. Using metal–semiconductor–metal photodetectors, bandwidths as high as 78 GHz have been reported [24] with an external quantum efficiency of 7.5% due to electrode blockage effects. The main attraction is their compatibility for integration with field-effect-transistor devices in optically controlled monolithic microwave integrated circuits. These experiments showed that MMIC-compatible devices fulfill the optic/microwave converter requirements.

1.2.3 Optical Control of MMIC Devices

An alternative signal detection approach is to directly introduce optical signals into microwave devices. This approach has several attractions such as (i) that optical control provides an extra control port to the microwave device, (ii) that no extra electronic circuits are required to process the detected signals before application to the microwave device, and (iii)

that the optical control signal is immune to electromagnetic interference. The physical process used in this approach is usually optically induced carrier generation through intrinsic absorption. In undepleted material, the photoconductive effect increases the conductivity of the semiconductor material. In depletion regions, this produces a photocurrent and alters the built-in potential, thus changing the device capacitance. Recent results are encouraging and some examples follow.

i) Amplifiers: Illuminating the gate region of field effect transistors, gain changes up to 20 dB can be controlled with optical powers of a few microwatts [25]. Using high electron-mobility transistor amplifiers an optical sensitivity 7–10 times higher is typically obtained [26].

ii) Oscillators: Optical control of oscillators using avalanche diodes [27], MESFETs [28], and bipolar transistors [29] may be performed with optical injection locking. The applied optical control signal is intensity modulated at a frequency close to the free-running frequency of the oscillator, of one of its harmonics, or one of its subharmonics. This gives rise to a current flow at the modulation frequency, leading to injection locking of the oscillator output frequency. Poor tuning is obtained because efficient coupling of light to the active region of the device is difficult.

iii) Opto-Electronic Mixers: Integrating the photodetection and mixing functions offers the attraction that electrical coupling between a separate detector and mixer with consequent matching and parasitic component problems is not required. Opto-electronic mixers have been demonstrated with photoconductive devices [30], diodes [31], field-effect transistors [32], and bipolar transistors [33].

Summary

Most recent developments in high-speed photodetectors together with their performance in terms of quantum efficiency and bandwidth have been discussed. To wisely choose a photodetector and to fully exploit the advantages of fiber radio access systems, the bandwidth, operating frequency, efficiency, saturation power, cost and linearity of the detector should be

taken into account. In addition, better performance is obtained if the detector can suppress the laser relative intensity noise and the amplified spontaneous emission noise from erbium-doped fiber amplifiers. This enables the link to achieve shot noise-limited performance at high optical powers. The link gain, spurious-free dynamic range, and noise figure should also be optimum. To realize these advantages, balanced photodetectors with high saturation photocurrents and broad bandwidth are needed.

1.3 Conclusion

The best choice for selecting the photodetector technology among equally performant devices will be cost-effectiveness. This is radically important for base stations in picocellular systems. The heterodyne detection scheme has been characterized in terms of RF output power, link gain, phase noise, and carrier to noise ratio. Dispersion compensation, if really needed, can be easily treated for with a phase-opposed path imbalance in the dual-frequency optical transmitter. Notably, link performance will be optimal if both optical carriers are phase correlated. It was assumed that the master laser imposes its phase noise, through injection locking, to the slave lasers thus, making them completely phase-correlated. So now a closer look at optical injection will be taken.

1.4 References

- [1] A. J. Seeds, "Microwave Photonics," *IEEE Transactions on Microwave Theory and Techniques*, Vol. 50, No. 2, march 2002, pp. 877–887.
- [2] C. H. Henry, "Phase noise in semiconductor lasers," *Journal of Lightwave Technology*, Vol. 4, 1986, pp. 298–311.
- [3] G. P. Agrawal and N. K. Dutta, *Semiconductor Lasers*, 2nd ed. New York: Van Nostrand Reinhold, 1993.
- [4] C. H. Henry, "Theory of the Linewidth of Semiconductor Lasers", *IEEE J. Quantum Elec.*, vol. 18, pp. 259-264, 1982.
- [5] P. Gallion et G. Debarge, "Quantum Phase Noise and Field Correlation in Single Frequency Semiconductor Lasers Systems", *IEEE J. Quantum Elec.*, vol. 20, pp.343-349, 1984.
- [6] U. Gliese, S. Norskov et T.N. Nielsen, "Chromatic Dispersion in Fiber Optic Microwave and Millimeter-Wave Links", *IEEE Trans. Microwave Theory Tech.*, vol 44, pp. 1716-1724, oct. 1996.
- [7] H. E. Rowe, *Signals and Noise in Communication Systems*, New York:Van Nostrand, 1965, pp. 113-116.
- [8] Intelsat earth station standards (IESS), "Performance characteristics for open-networkk digital television transmission", Document IESS-503, Feb 10, 2000, p. 11.
- [9] J. G. Proakis, *Digital communications*, New York: McGraw-Hill, 1989.
- [10] R.P. Braun, G. Grosskopf, D. Rohde et F. Schmidt, "Optical Millimeter-Wave Generation and Transmission Experiments for mobile 60 GHz Band Communications", *Elec. Lett.*, vol 32, pp. 626-627, mars 1996.
- [11] R.-P. Braun, "Fiber Radio dystems, Applications and Devices", *ECOC'98 Tutorial.*, pp. 89-119, sept. 1998.
- [12] A. Umbach, G. Unterborsch, R.P. Braun, G. Grobkopf, "Stable optical source and high-speed photodetector used for remote fiber-optic 64-GHz mm wave generation, " *OFC'98, Technical Digest*, 1998. Pp. 260-261.
- [13] K. Kato, Y. Muramoto, A. Kozen, Y. Itaya, T. Nagatsuma, and M. Yaita, "110-GHz 50%-efficiency waveguide p-i-n photodiode for a 1550 nm wavelength," in *5th Optoelectron. Conf. Tech. Dig.*, 1994, pp. 66–67.
- [14] W. Gartner, "Depletion layer photoeffects in semiconductors," *Phys.Rev.*, vol. 116, pp. 84–87, 1959.

-
- [15] K. Kato, A. Kozen, Y. Muramoto, Y. Itaya, T. Nagatsuma, and M. Yaita, "110 GHz 50% efficiency mushroom mesa waveguide p-i-n photodiode for a 1550 nm wavelength," *IEEE Photon. Technol. Lett.*, vol. 6, pp. 719–721, 1994.
- [16] D. Jager, R. Kremer, and A. Stohr, "High speed travelling-wave photodetectors, modulators and switches," in *IEEE/LEOS RF Opto-Electron. Summer Topical Meeting*, Keystone, CO, Aug. 1995, pp. 57–58.
- [17] H. Ito, T. Furata, S. Kodama, and T. Ishibashi, "InP/InGaAs uni-travelling- carrier photodiode with 310 GHz bandwidth," *Electron. Lett.*, vol. 36, pp. 1809–1810, 2000.
- [18] H. Fukano, Y. Muramoto, K. Takahata, and Y. Matsuoka, "High efficiency edge illuminated uni-travelling-carrier structure refracting facet photodiode," *Electron. Lett.*, vol. 35, pp. 1664–1665, 1999.
- [19] D. Rohde, H. Ehlers, R. Ziegler, R.-P. Braun, J. Braunstein, W. Bronner, and G. Grosskopf, "Optic/millimeter-wave converter for 60 GHz radio-over-fiber systems," in *Proc. 9th Microwaves Optron. Conf.*, Sindelfingen, Germany, April 1997, pp. 311–315.
- [20] A. Umbach, S. V. Waasen, U. Auer, H. G. Bach, R. M. Bertenburg, V. Breur, W. Ebert, G. Janssen, G. G. Mekonnen, W. Passenberg, W. Schlaak, C. Schraam, A. Seeger, G. J. Tegude, and G. Unterbosch, "Monolithic pin-HEMT 1.55 μ m photoreceiver on InP with 27 GHz bandwidth," *Electron. Lett.*, vol. 32, pp. 2142–2143, 1996.
- [21] A. Umbach, W. Passenberg, G. Unterborsch, G. G. Mekonnen, W. Schlaak, C. Schramm, W. Ebert, P. Wolfram, H.-G. Bach, S. van Waasen, R. M. Bertenburg, G. Janssen, R. Reuter, U. Auer, and F.- J. Tegude, "27 GHz bandwidth integrated photoreceiver comprising a waveguide fed photodiode and a GaInAs/AlInAs-HEMT-based travelling wave amplifier," presented at the 54th Annu. Device Res. Conf., Univ. California at Santa Barbara, 1996.
- [22] D. V. Plant, D. C. Scott, H. R. Fetterman, L. K. Shaw, W. Jones, and K. L. Tan, "Optically generated 60 GHz millimeter-waves using AlGaAs/InGaAs HEMT's integrated with both quasi-optical antenna circuits and MMIC's," *IEEE Photon. Technol. Lett.*, vol. 4, pp. 102–105, Jan. 1992.
- [23] E. Suematsu and N. Imai, "Fiber optic/millimeter-wave subcarrier link using InP/InGaAs HBT optical/RF transducer," in *Tech. Dig. OEC'94*, Makuhari Messe, Tokyo, Japan, July 1994, pp. 396–397.
- [24] E. Droge, E. H. Bottcher, S. Kollakowski, A. Strittmatter, O. Reimann, R. Steingruber, A. Umbach, and D. Bimberg, "Distributed MSM photodetectors for the long wavelength range," in *Eur. Opt. Commun. Conf.*, vol. 1, Oslo, Sweden, 1998, pp. 20–24.

-
- [25] A. A. A. de Salles, "Optical control of GaAs MESFET's," *IEEE Trans. Microwave Theory Tech.*, vol. MTT-31, pp. 812–820, 1981.
- [26] R. N. Simons, "Microwave performance of an optically controlled AlGaAs/GaAs high electron mobility transistor and GaAs MESFET," *IEEE Trans. Microwave Theory Tech.*, vol. MTT-35, pp. 1444–1455, 1987.
- [27] A. J. Seeds, J. F. Singleton, S. P. Brunt, and J. R. Forrest, "The optical control of IMPATT oscillators," *J. Lightwave Technol.*, vol. LT-5, pp. 403–411, 1987.
- [28] A. A. de Salles and J. R. Forrest, "Initial observations of optical injection locking of GaAs metal semiconductor field effect transistor oscillators," *Appl. Phys. Lett.*, vol. 38, pp. 392–394, 1981.
- [29] H.W. Yen and M. K. Barnoski, "Optical injection locking and switching of transistor oscillators," *Appl. Phys. Lett.*, vol. 32, pp. 182–184, 1978.
- [30] D. K. W. Lam and R. I. Macdonald, "GaAs optoelectronic mixer operation at 4.5 GHz," *IEEE Trans. Microwave Theory Tech.*, vol. ED-31, pp. 1766–1768, 1984.
- [31] N. J. Gomes and A. J. Seeds, "Tunnelling metal-semiconductor contact optically pumped mixer," *Proc. Int. Elect. Eng.*, pt. J, vol. 136, pp. 88–96, 1989.
- [32] H. R. Fetterman and D. C. Ni, "Control of millimeter-wave devices by optical mixing," *Microwave Opt. Technol. Lett.*, vol. 1, pp. 34–39, 1988.
- [33] Z. Urey, D. Wake, D. J. Newson, and I. D. Henning, "Comparison of InGaAs transistors as optoelectronic mixers," *Electron. Lett.*, vol. 29, pp. 1796–1798, 1993.

Chapter 2: **INJECTION**

LOCKED DFB LASERS

Complete comprehension of the side-mode injection locking technique requires a full characterization of semiconductor laser diodes under external optical injection. Basically, there are two classical methods for mathematically modeling the operation of semiconductor lasers. The first method conceptualizes particle exchange of photons and electrons where the rate of absorption and emission of photons along with the rate of recombination of electrons and holes are carefully balanced leading to particle and energy conservation. This is the standard volume-averaged rate-equations approach, which is robust but difficult to apply when non-uniformities and the phase of the electromagnetic field are important. For distributed-feedback semiconductor lasers (DFB), both the phase of the field and non-uniformities are important, so an approach based on interactions between electromagnetic fields and electric dipoles in an active optical medium is more appropriate. Both methods are just different aspects of the same physics of energy conservation and are compatible.

Optical injection analyses of semiconductor lasers are usually limited to the case where the intensity distribution along the cavity is supposed uniform [1]-[6]. These studies are based on a standard rate-equation analysis. As a consequence, inaccurate results regarding the stable locking bandwidth are obtained when describing optical injection in DFB semiconductor lasers, especially those where a phase shift has been inserted to improve the side-mode suppression ratio (SMSR) and for which the spatial hole burning effect becomes

important. A rate-equations approach is suitable for Fabry-Perot semiconductor lasers where mode hopping asymmetrically reduces the single mode locking range. In DFB lasers, strong mode selection due to the grating structure impedes this mode hopping. As a consequence, the stable locking bandwidth is more symmetrical in DFB semiconductor lasers as it will soon be seen. More generally, optical synchronization can be maintained even on the case of a non-cooperative injection where the phase relation between the injected and cavity field leads to a mode threshold gain that is higher than that of the free-running laser [4].

The main objective of this chapter is therefore the detailed description of optical injection of DFB semiconductor lasers using a longitudinal field analysis based on the coupled-wave equations.

2.1 Coupled-Wave Theory of DFB Semiconductor Lasers

The analysis of external optical injection in DFB semiconductor lasers is proposed here using the coupled-wave theory of DFB semiconductor lasers [7], which is directly derived from the scalar Helmholtz equation considering a periodic and complex electric permittivity. This permittivity is related to the spatial modulation of the refractive index and gain constant:

$$n(z) = n + n_1 \cos(2\beta_0 z) \quad \text{Eq. 2.1}$$

$$\alpha(z) = \alpha + \alpha_1 \cos(2\beta_0 z) \quad \text{Eq. 2.2}$$

where n and α represent the mean value of the medium parameters, n_1 and α_1 are the amplitudes of the spatial modulation, and $\beta_0 = \pi / \Lambda$ is the Bragg frequency associated to the spatial period Λ . Under the hypothesis of a plane wave with slowly varying envelope, the electric field $E(z)$ is decomposed in forward $F(z)$ and reverse $R(z)$ complex amplitudes that feed energy to each other due to Bragg scattering in the laser cavity. This field is sought in the form

$$E(z) = F(z) \exp^{-j\beta_0 z} + R(z) \exp^{j\beta_0 z}. \quad \text{Eq. 2.3}$$

Inserting Eq. 2.3 in the Helmholtz equation and neglecting second-order derivatives the coupled-wave equations are obtained as:

$$\begin{aligned}\frac{\partial F}{\partial z} &= j\kappa R + (\alpha - j\delta)F \\ -\frac{\partial R}{\partial z} &= j\kappa F + (\alpha - j\delta)R\end{aligned}\tag{Eq. 2.4}$$

where κ is the coupling coefficient which depends on the spatial modulation of the refractive index and gain constant by,

$$\kappa = \pi n_1 / \lambda_0 + j\alpha_1 / 2,\tag{Eq. 2.5}$$

and δ is the normalized detuning of the oscillating mode from the wave vector at the Bragg frequency $\beta_0 = \pi / \Lambda$ written as:

$$\delta = n\omega / c - \pi / \Lambda\tag{Eq. 2.6}$$

where Λ is the grating spatial period, c the speed of light in vacuum, and ω the angular lasing frequency. It is easily seen that the general solution of Eq. 2.4 is of the form

$$\begin{aligned}F(z) &= f_1 \exp^{\gamma z} + f_2 \exp^{-\gamma z} \\ R(z) &= r_1 \exp^{\gamma z} + r_2 \exp^{-\gamma z}\end{aligned}\tag{Eq. 2.7}$$

where γ is the complex propagation constant. The absolute field amplitudes f_1, f_2, r_1, r_2 will remain unspecified for the moment as they depend on the boundary conditions and, in addition, have to be obtained from a nonlinear calculation which takes into account gain saturation. By inserting the general solution (Eq. 2.7) in the coupled-wave equations (Eq. 2.4) it is found that nontrivial solutions require that the dispersion relation, $\gamma^2 = (\alpha - j\delta)^2 + \kappa^2$, and the following eigenvalue equation be fulfilled:

$$\begin{aligned}& e^{j\Omega} \left[1 + pe^{\gamma L} \frac{\rho_r - p}{1 - \rho_r p} \right] \left[p + e^{-\gamma L} \frac{1 - \rho_l p}{\rho_l - p} \right] \\ &= e^{-j\Omega} \left[1 + pe^{-\gamma L} \frac{1 - \rho_l p}{\rho_l - p} \right] \left[p + e^{\gamma L} \frac{\rho_r - p}{1 - \rho_r p} \right]\end{aligned}\tag{Eq. 2.8}$$

where Ω is the phase shift and, ρ_r and ρ_l are related to the amplitude reflectivities, $\hat{\rho}_r$ and $\hat{\rho}_l$, of the right and left facets by:

$$\rho_r = \hat{\rho}_r e^{-j(2\beta_0 L - \Omega)} \quad \text{Eq. 2.9}$$

and

$$\rho_l = \hat{\rho}_l e^{-j(2\beta_0 L - \Omega)}. \quad \text{Eq. 2.10}$$

Parameter p is defined by

$$p = \frac{-\gamma + \alpha - i\delta}{i\kappa}. \quad \text{Eq. 2.11}$$

The multiple solutions of Eq. 2.8 represent the different cavity modes of the laser structure and their associated threshold gain. These threshold values are different from mode to mode and only the mode with the lowest threshold gain will lase. In the following, a perturbation method of the coupled-wave theory will be used to describe external optical injection.

2.2 Optically Induced Frequency and Gain Changes

The analysis here is limited to weak injection and for the sake of simplicity, to the usual case of phase-shifted DFB lasers having a real coupling coefficient as shown schematically on Figure 2.1.

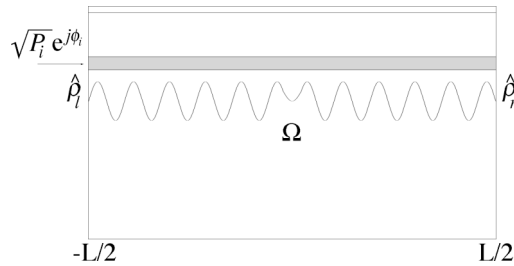


Figure 2.1: DFB semiconductor laser structure.

Generalization to other laser structures is straightforward. Such a laser is dynamically described on the free-running regime using the time-travelling coupled-wave equations [7]-[10]. To account for external optical injection, the method presented by Favre [10] for describing external optical feedback in DFB lasers is used here. In his analysis, the mirror external reflectivity is taken into account for calculating the equivalent facet reflectivity. In this case, the equivalent reflectivity is recalculated to include optical injection (assuming, for instance, that injection occurs at the left facet):

$$\hat{\rho}_{leq}(z) = \hat{\rho}_l + (1 - \hat{\rho}_l^2) \sqrt{\frac{P_i(z)}{P(z)}} e^{-j\theta(z)} \quad \text{Eq. 2.12}$$

where $P_i(z)/P(z)$ is the local power density ratio between the injected and cavity fields distributed throughout the cavity and $\theta = \phi_i - \phi$ is the relative phase between these two fields. The change in the reflectivity due to injection resulting from Eq. 2.10 and Eq. 2.12 is:

$$\Delta\rho_l(z) = (1 - \hat{\rho}_l^2) \sqrt{\frac{P_i(z)}{P(z)}} e^{-j\theta(z)} e^{-j(2\beta_0 L - \Omega)} \quad \text{Eq. 2.13}$$

Assuming a weak injection rate ($\sqrt{P_i/P} \ll 1$), the eigenvalue equation (Eq. 2.8) can be linearized about γ_0 , solution of Eq. 2.8 without injection. This leads to a relation between the variation of the complex propagation constant $\Delta\gamma = \gamma - \gamma_0$ and the reflectivity variation $\Delta\rho_l$. Differentiation of the dispersion relation allows us to express the gain $\Delta\alpha = \alpha - \alpha_0$ and the normalized detuning change $\Delta\delta = \delta - \delta_0$ as:

$$\Delta\alpha L - j\Delta\delta L = \frac{\gamma_0}{\alpha_0 - j\delta_0} \Delta\gamma L \quad \text{Eq. 2.14}$$

$\Delta\gamma$ is the only variable in the right-hand side of Eq. 2.14 that depends on the injection conditions. According to the Favre approach, a proportionality relation [10] can be assumed and write Eq. 2.14 as:

$$\Delta\alpha L - j\Delta\delta L = \frac{C_l}{2} \sqrt{\frac{P_i}{P}} e^{-j\theta} \quad \text{Eq. 2.15}$$

where C_l is just the complex coefficient introduced by Favre (the 1/2 factor arbitrarily appears here for later comparison with Fabry-Perot lasers). C_l only depends on solitary DFB laser modal characteristics, e.g. the grating position with respect to the facet, the reflectivity, the threshold gain or the phase deviation, and can be calculated using Eq. 2.13 and the logarithmic differentiation of the eigenvalue equation (Eq. 2.8).

If ΔN and $\Delta\omega$ denote, respectively, the carrier density and resonant frequency changes, the detuning induced change $\Delta\delta$ is derived from Eq. 2.6,

$$\Delta\delta = \frac{n_g}{c} \Delta\omega + \frac{\omega}{c} \frac{\partial n}{\partial N} \Delta N \quad \text{Eq. 2.16}$$

where n_g is the group refractive index. Relating the carrier density variations ΔN to the gain per unit of time variation by $\partial G / \partial N = 2\Delta\alpha c / (n_g \Delta N)$, Eq. 2.16 is rewritten as:

$$\Delta\omega = \frac{c}{n_g L} (\Delta\delta L - \alpha_H \Delta\alpha L). \quad \text{Eq. 2.17}$$

The linewidth enhancement factor α_H expresses the coupling between the phase and amplitude of the field in a semiconductor laser and is defined by

$$\alpha_H = -\frac{2\omega}{n_g} \frac{\partial n / \partial N}{\partial G / \partial N}. \quad \text{Eq. 2.18}$$

Finally, considering Eq. 2.17, the resonant frequency and gain changes are obtained by separating Eq. 2.15 into its real and imaginary parts:

$$\Delta\omega = \rho(1 + \alpha_H^2)^{1/2} \sin(\theta - \arg C_l - \tan^{-1} \alpha_H) \quad \text{Eq. 2.19}$$

$$\Delta G = 2\rho \cos(\theta - \arg C_l) \quad \text{Eq. 2.20}$$

where $\rho = c / (2n_g L) |C_l| \sqrt{P/P_i}$ is the normalized injection rate. By eliminating θ from these two equations, real values of ΔG are only obtained if

$$|\Delta\omega| \leq \rho(1 + \alpha_H^2)^{1/2}. \quad \text{Eq. 2.21}$$

This inequality defines the injection locking range. All points lying within are stationary solutions of the coupled-wave equations but they are not always stable. In the next section the stability will be fully discussed.

The complex coefficient C_l , in general, can be expressed analytically and derived from the eigenvalue equation associated to the coupled-mode equations. In homogeneous Fabry-Perot lasers (Figure 2.2), C_l is simply a constant depending on the amplitude reflectivity, whereas in DFB lasers, the coefficient strongly depends on its grating structure and consequently, so does the normalized injection rate ρ . This fact is of great importance for a stable locking range (Figure 2.3). Lasers having a weak coupling ($\kappa L \leq 1$) exhibit a large locking bandwidth and are interesting for applications such as amplifiers and optical-phase modulators where given frequency detunings must not cause unlocking of the slave laser. For strong coupling ($\kappa L \geq 4$), the locking bandwidth is largely reduced making this lasers more attractive for applications requiring narrow-band filters like dense multi-channel systems. For as to intermediate values of the coupling factor ($1 < \kappa L < 4$), a wide range of applications may be adequate like chirp reduction, phase correlation, laser array synchronization, etc., where a symmetrical locking bandwidth is important.

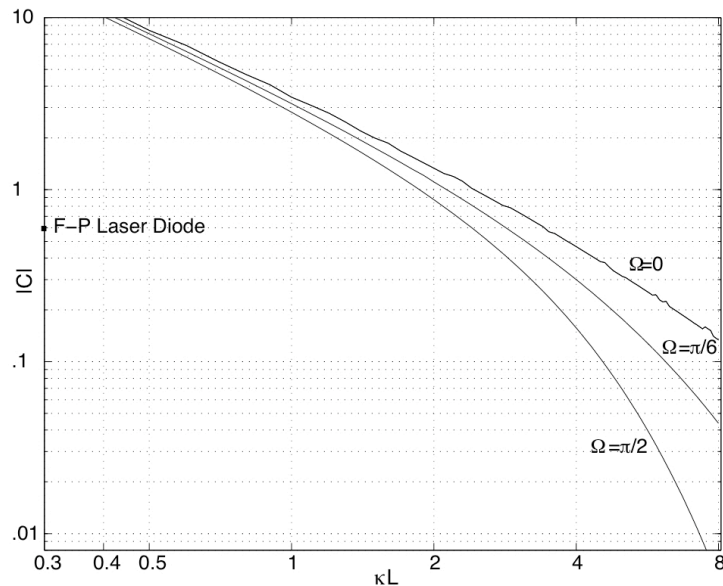


Figure 2.2: Coefficient C_l for the DFB laser structure.

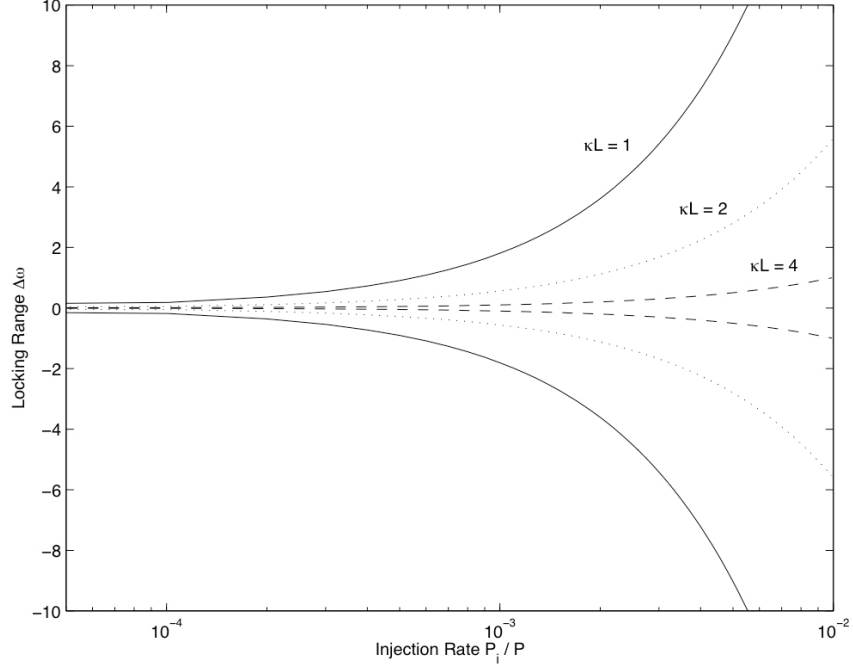


Figure 2.3: Static locking bandwidth for different coupling coefficients.

2.3 Injection Locking Dynamic Modeling

If the frequency of the injected light lies within the locking bandwidth, the injected laser will synchronize its frequency to that of injected light. For accurate modeling of this synchronization process, optically induced gain and frequency changes, ΔG and $\Delta\omega$, are included in the time-travelling coupled-wave equations describing DFB lasers [9]

$$\left(\frac{1}{v_g} \frac{\partial F}{\partial t} + \frac{\partial F}{\partial z} \right) = j\kappa R + \left[\alpha + \frac{\Delta G}{2v_g} - j \left(\delta + \frac{\Delta\omega}{v_g} \right) \right] F + i_{spf} \quad \text{Eq. 2.22}$$

$$\left(\frac{1}{v_g} \frac{\partial R}{\partial t} - \frac{\partial R}{\partial z} \right) = j\kappa F + \left[\alpha + \frac{\Delta G}{2v_g} - j \left(\delta + \frac{\Delta\omega}{v_g} \right) \right] R + i_{spr} \quad \text{Eq. 2.23}$$

$$\Gamma \left(\frac{dN}{dt} + \frac{N}{\tau_r} \right) + 2\Gamma g_m v_g \left(\frac{F^* F + R^* R}{v_g} \right) = \frac{I}{eL}, \quad \text{Eq. 2.24}$$

where I is the injection current, α the net gain, δ the phase detuning, g_m the material optical-field gain per unit distance (taken as nonlinear as in [9]), τ_r the spontaneous

recombination time constant including all mechanisms, and the terms i_{sp} represent the spontaneous excitation, evaluated from the bipolar radiative recombination, taken as locally proportional to N^2 and include the spontaneous confinement factor which is similar to the gain confinement factor Γ . The latter gives an effective gain below the material gain and reduces the effective phase shift associated with the complex gain. The optical density (photons per unit length) is given from $(F^*F + R^*R)/v_g$ in Eq. 2.24.

2.3.1 Stability

A static solution to the coupled-wave equations (Eq. 2.22-3.24) describing an injected DFB semiconductor laser requires the necessary condition that the frequency detuning between the master and slave laser remain bounded, i.e. $|\Delta\omega| \leq \rho(1 + \alpha^2)^{1/2}$ as previously established. In F-P lasers [2,3], the competition between spontaneous emission amplification and forced oscillations at the master laser frequency is accompanied with a net gain change whose sign depends on the phase detuning. For a positive net gain resulting from injection, the locking bandwidth is reduced because the spontaneous emission amplification of a cavity free mode is divergent while the injected mode is attenuated by a coherent injection in phase opposition and consequently, mode hopping is observed. In contrast, DFB lasers, having a high side-mode suppression ratio, preserve dynamic stability all throughout the static locking range [4]. Nevertheless, classical systems involving differential equations impose a stability analysis based on the Routh-Hurwitz criterion [3]. This leads in establishing the static/dynamic limit of the locking bandwidth defined in terms of the modified damping time associated to relaxation oscillations:

$$\frac{1}{\tau_r} = \frac{1}{\tau_{r0}} + 2\rho(1 + \alpha_H^2)^{1/2} \cos(\theta + \arg C + \tan^{-1} \alpha_H) \quad \text{Eq. 2.25}$$

where

$$\frac{1}{\tau_{r0}} = A + 2BN_0 + 3CN_0^2 + \frac{G_m P_0}{1 + \epsilon P_0} \left(1 + \frac{\epsilon}{G_m \tau_p} \right) \quad \text{Eq. 2.26}$$

is the damping constant of the free-running laser. Coefficients A , B , and C are, respectively, the linear nonradiative, the bipolar radiative, and the Auger recombination

coefficients. G_m' is the differential power gain, ε the gain-saturation parameter, and τ_p' the effective photon lifetime including the distribution losses. The last term in Eq. 2.26 represents the nonlinear gain saturation, which damps the relaxation oscillation and tends to stabilize the single-mode laser operation [1]. The spontaneous emission rate has been neglected because it is only important for very low values of the average power inside the laser cavity. This corresponds to a biasing current near threshold but the present study concentrates on operation above threshold.

An infinite damping time in Eq. 2.25 defines the hyperbola depicted in Figure 2.4. Its position depends on the coupling coefficient κL , the phase-amplitude coupling factor α_H , and the phase shift Ω via the complex constant C_l previously introduced. Due to spontaneous power fluctuations, the locked laser undergoes phase fluctuations around the selected operation point that may lead to an unlocked state. The locking stability is enlarged as the coupling coefficient κL increases. Lasers with low coupling factors are better for applications that require fast switching between stable-synchronized operation and optically induced modulation. Different applications of injection locking are discussed in [11]-[16].

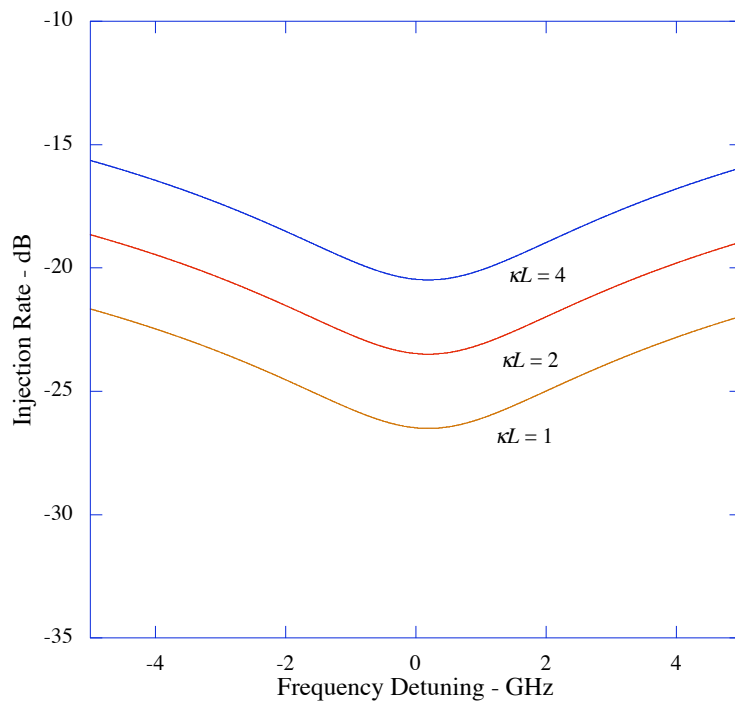


Figure 2.4: Dynamic limit of the stable locking range for different coupling coefficients.

2.3.2 Numerical Model Implementation

The system of equations Eq. 2.22-2.24 is solved numerically using a central finite-difference method [9]. Since the carrier density varies, in general, on a lower time scale than the optical fields, several key approximations are made in the numerical model: (i) the carrier density is approximately constant over two or three time steps even though the optical field may change significantly over them; (ii) a forward-finite difference scheme has adequate accuracy for the carrier equation, which is composed entirely of real quantities; (iii) as for the rapidly changing complex optical fields, a second-order central-difference is used giving greater accuracy. Appropriate boundary conditions have to be carefully included to describe optical injection; namely, the field at the injection facet has to be equal to the master laser field except for a proportionality constant η to account for coupling losses. This coupling factor is taken as real since the lasers are assumed to have anti-reflection coated facets (the equivalent facet reflectivity is taken into account by the gain and frequency variations due to injection derived in section 2.2). To observe the different injection regimes the coupling factor η is varied in the numerical simulations from 10^{-6} to 10^{-2} . A similar system of equations is used for modeling the master laser whose field solution is used as the injection field. The system inputs are then the biasing current, the modulation current, and the injection coupling factor. Table 1 shows the laser structure and computational parameters used for the simulation. The model predicts the injection characteristics like the locking range and chirp reduction in function of the power supply conditions and laser structure parameters.

	symbol	value
Free space wavelength	λ	1.55 μm
Group refractive index	n_g	3.7
Spontaneous emission bandwidth	$\Delta\lambda_{spont}$	0.08 μm
Nominal length of laser	L	400 μm
Average value kappa L product	κL	2
Confinement factor	Γ	0.35
Spontaneous emission coupling factor	β_{spont}	1.2×10^{-6}
Guide loss parameter	aL	1.6
Linear nonradiative	A	0
Spontaneous recombination coefficient	B	10^{-10} cm^2
Auger recombination coefficient	C	$3 \times 10^{-29} \text{ cm}^5$
Electron density at transparency	N_0	$1.5 \times 10^{18} \text{ m}^{-3}$
Differential gain length product at transparency	$g'_m L$	20
Henry's linewidth factor	α_H	3
Gain saturation factor	ϵ	0.05
Complex coefficient	C_l	$0.874 e^{-j\pi/2}$
Number of steps over laser length		63
Order of FFT		19
Step length		6.35 μm
Time step		12.8 ps

Table 2.1: Laser structure and computational parameters used for the large-signal simulation

2.3.3 Injection Regimes

Depending on the injection rate and frequency detuning, the operation point of the injected laser can lie inside or outside the stable locking range. Putting together Figure 2.3 and Figure 2.4 with, for instance, $\kappa L = 2$, the unconditionally stable locking range is obtained (Figure 2.5). The different regions represented by roman numerals indicate the different injection regimes. Regime *i* depicts the stable locking bandwidth where the laser is unconditionally stable within the whole locking band. The width of regime *i* is given by the locking range defined in Eq. 2.21 and the height is the range of injection ratios, $0 < \rho \leq 1/[\tau_{r0}(1 + \alpha_H^2)^{1/2}]$, obtained with Eq. 2.25. The stable locking range in regime *iii* is separated by an instability interval. The injection ratio range of this regime is calculated by finding the cross points between the static (Eq 3.21) and dynamic limit (Eq. 2.25), thus

obtaining $1/[\tau_{r0}(1 + \alpha_H^2)^{1/2}] \leq \rho \leq 1/[\tau_{r0}(1 + \alpha_H^2)^{1/2} \sin 2\phi_0]$, where $\phi_0 = \tan^{-1} \alpha_H$. It is important to notice that the symmetry of the locking range in regime *i* and the existence of another stable locking range with positive detuning in regime *iii*, have been experimentally observed only in DFB semiconductor lasers, as opposed to F-P lasers. Intuitively, it could be believed that in DFB lasers, in which a high side-mode suppression ratio is obtained, the gain change expressed by Eq. 2.20 makes the stable locking impossible for positive detunings, because the positive values of ΔG may induce the appearance of the free-running main mode of the injected laser. However, simulations presented following this paragraph show that in regime *i*, stable locking is always maintained within the static locking range, as experimentally observed. It was found that the time-averaged photon density within the locking range decreases as the frequency detuning increases. Out of the locking range in regime *ii*, the photon density loses its time-independence with the induced modulation. The time-averaged photon density converges gradually to the value of the free-running laser. In F-P semiconductor lasers, the photon density decrease of the locked main mode for positive detunings is compensated by the contribution of the side longitudinal modes, which have a small gain margin. This is why no output optical power decrease can be found [2], [3].

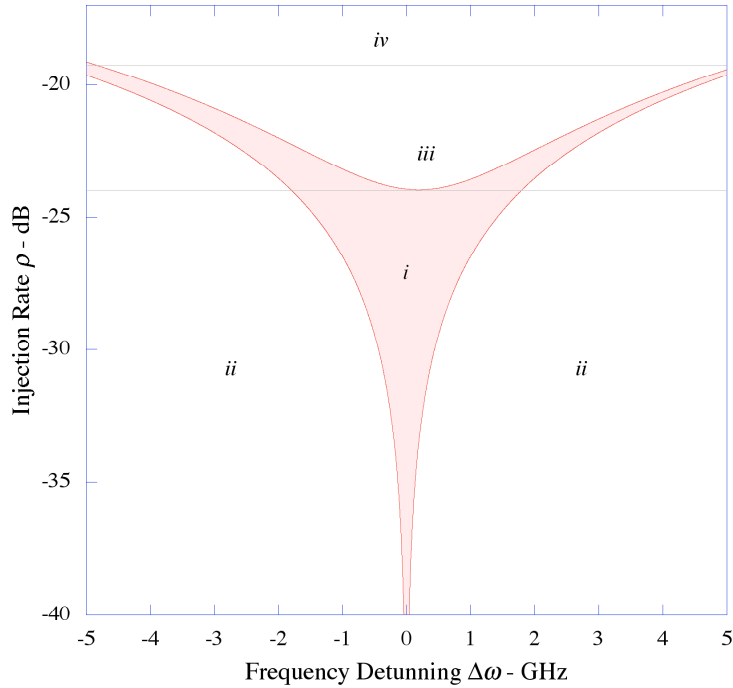


Figure 2.5: Stable locking bandwidth depicting the different injection regimes.

Large-signal simulations of the injected DFB semiconductor laser were carried out for operation on different regimes in order to observe the changes of the power spectrum. These

results are represented in Figure 2.6 to Figure 2.10. Operation within the stable-locking bandwidth (regime *i*) results in a power spectrum only dominated by the master laser frequency (Figure 2.6). No relaxation oscillation sidebands can be observed. On Figure 2.7 to Figure 2.10, the biasing current of the slave laser and the injection coupling factor are simultaneously adjusted to increase the frequency detuning between the master and slave laser, and also, to vary the injection rate. This corresponds in selecting an operation point on different regions on the injection rate - frequency detuning plane [17]. At the edge of the locking bandwidth (Figure 2.7), the slave laser does not synchronize on the master laser frequency, but competes with it for gain saturation and the two frequencies appear in the spectrum. A higher frequency detuning (regime *ii*) results in a modulation regime (Figure 2.8), which is just the result of nonlinear mixing between the injected and the free-running field, as the appearance of the master laser frequency image with respect to the free-running lasing frequency suggests it [18]. Increasing the injection rate, as to operate in regime *iii*, results in an induced multi-modal operation associated to a self-pulsating regime (Figure 2.9). A further increment of the injection level (regime *iv*) renders the slave laser operation chaotic and is characterized by a noisy spectrum on the vicinity of master laser frequency (Figure 2.10). It is usually accompanied by strong output power suppression.

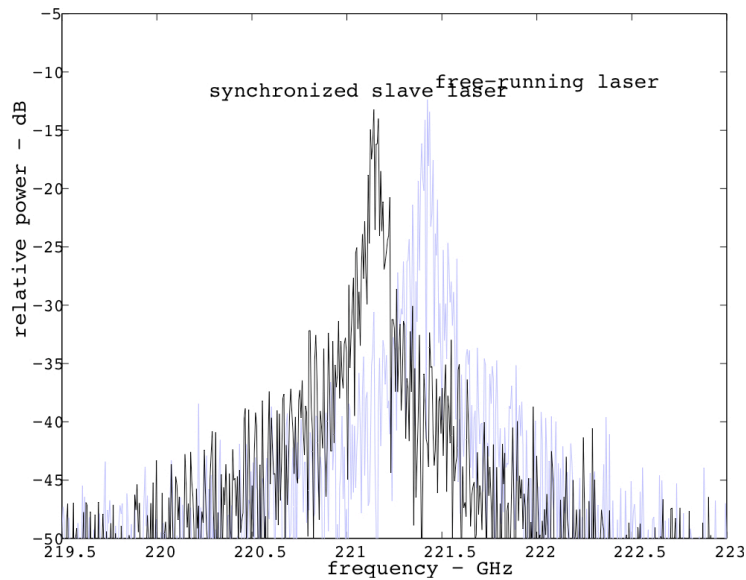


Figure 2.6: Frequency synchronization of the slave laser to the master laser.

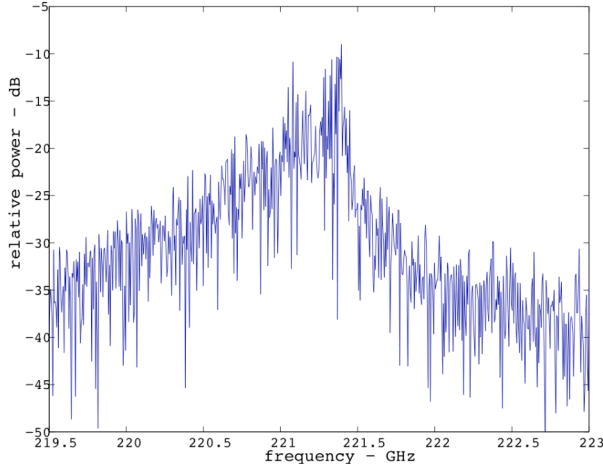


Figure 2.7: Operation at the edge of the static locking bandwidth.

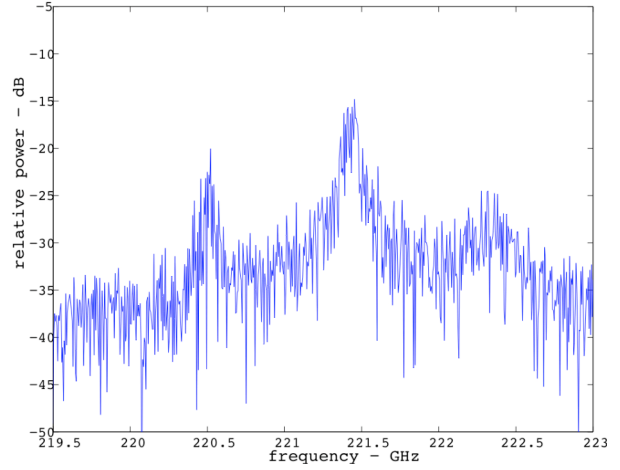


Figure 2.8: Nonlinear mixing between the master laser frequency and the slave laser free-running frequency.

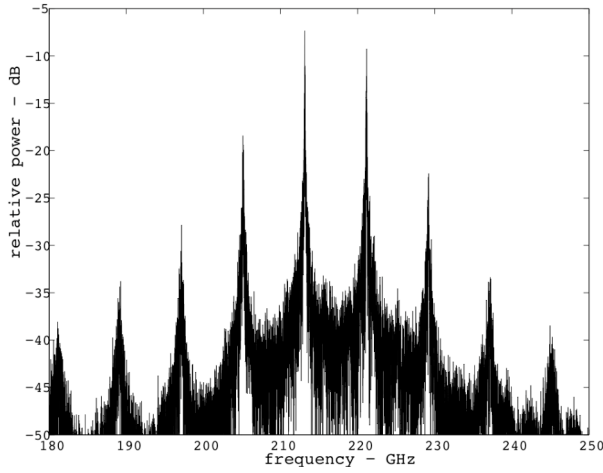


Figure 2.9: Self-pulsating regime.

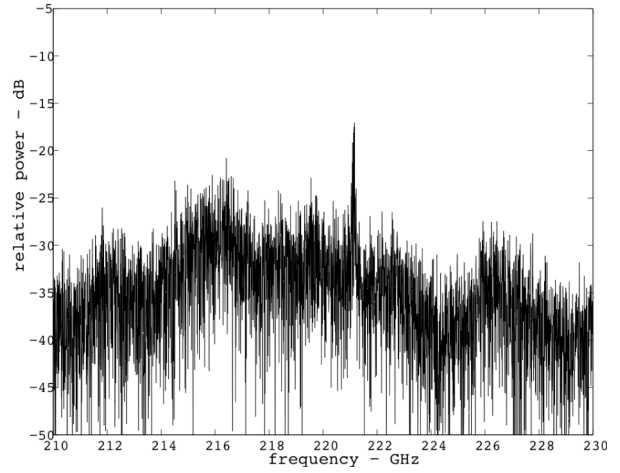


Figure 2.10: Chaotic behavior provoked by a high injection rate.

2.3.4 Chirp Reduction and Optical PSK Modulation

When a semiconductor laser is directly modulated in intensity, the simultaneous frequency modulation is accompanied by a continuous frequency variation called chirping produced by the phase-amplitude coupling factor α_H . It is well known that these effects can be largely reduced when the laser is injection-locked to a master laser [19]. To validate the model to this respect, the power spectral density of a modulated free-running laser and a synchronized laser were simulated. Due to simultaneous intensity and frequency modulation, the free-running laser spectrum is strongly asymmetrical (Figure 2.11). Thanks to the chirp reduction obtained (Figure 2.12), the sidebands are now symmetrical with respect to the

optical carrier and are reduced by more than 8 dB. Chirp reduction is only attainable for strong optical injection and of course, for modulation frequencies less than the locking range [20]. The modulation bandwidth can be dramatically enhanced by injection because the total modal photon density also depends on the phase detuning, which varies during modulation, due to the refraction index dependence on carrier density. This results in an increased coupling between the carriers and photons, leading to a higher effective differential gain.

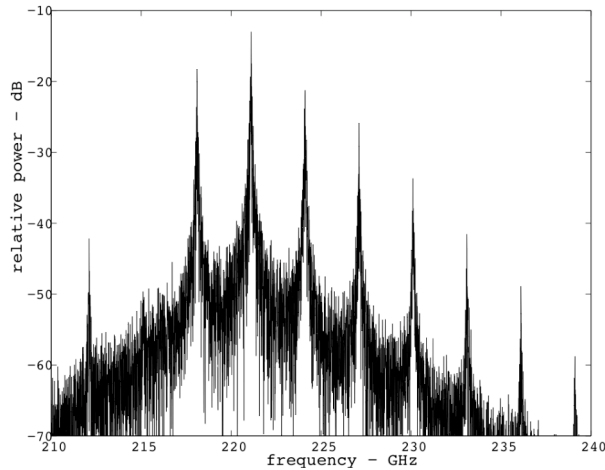


Figure 2.11: Free-running spectrum of the modulated DFB laser.

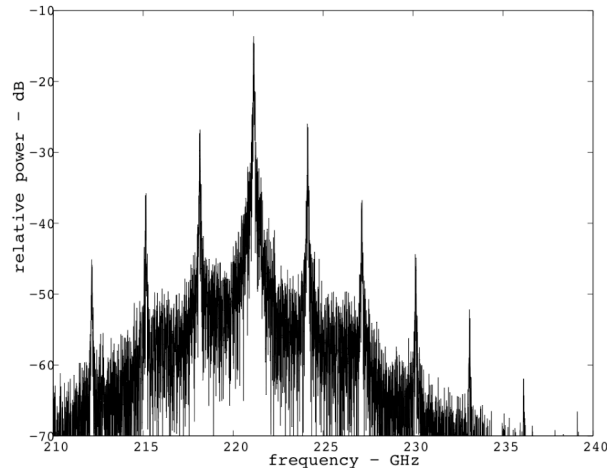


Figure 2.12: Injection-locked spectrum of the modulated DFB laser.

The frequency modulation induced in a directly intensity-modulated semiconductor laser is converted to phase modulation when the laser is injection-locked to a master laser. The presence of a symmetric stable locking range in DFB semiconductor lasers opens the possibility of using optical PSK modulation, which is the scheme achieving highest sensitivity. Given the locking range symmetry, the optical phase may vary between $\pm\pi/2$, thus being compatible with practical PSK modulation systems where the phase is usually shifted by a total amount equal to π .

2.3.5 Microwave Generation

An attractive technique for optically generating microwaves can be designed by synchronizing two slave lasers to different phase correlated IM-FM sidebands of a modulated master laser in which the optical frequency difference equals the desired microwave frequency [21]. The spectral purity of the RF signal depends then on the strength of this

phase correlation. The beat signal power spectrum simulated with free-running lasers is shown on Figure 2.13. It was confirmed that the linewidth of the RF signal is the sum of the linewidths of each laser. When the slave lasers (Figure 2.14) are synchronized on different modulation sidebands of the master laser, the beat signal linewidth (Figure 2.15) is drastically reduced with comparison to the beat signal of the free-running lasers. The linewidth observed is just the numerical resolution used on the computer simulation. The synchronized slave lasers reject their own phase noise [22] and a very pure signal is obtained. The desired applications have, of course, to maintain the phase relation that is very vulnerable to the true delays and to the fiber dispersion.

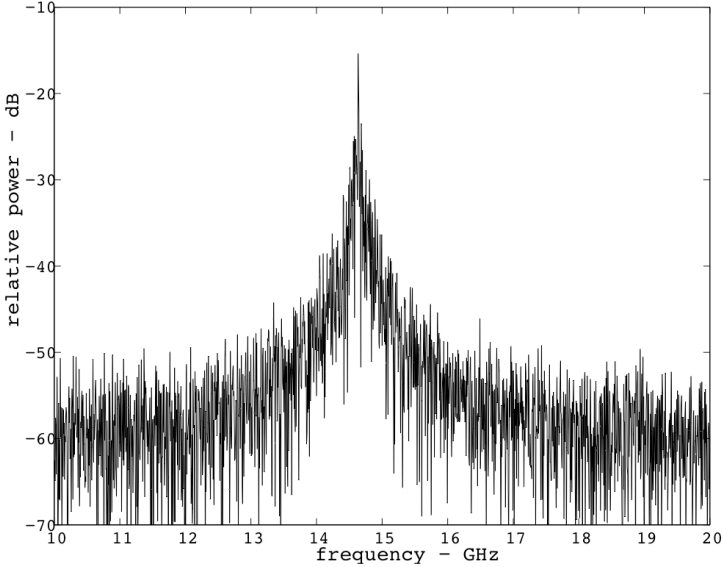


Figure 2.13: Free-running spectrum of the beat signal between the slave lasers.

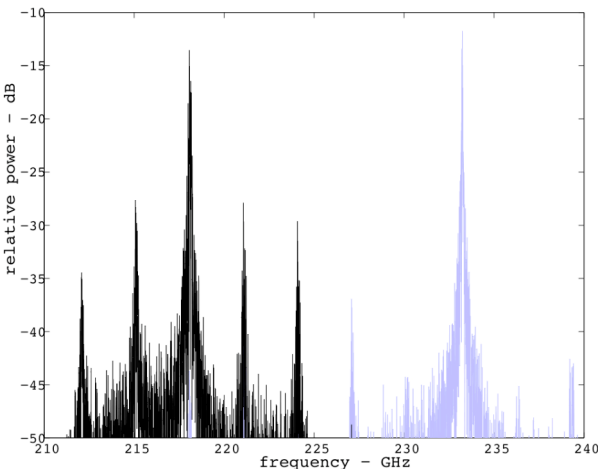


Figure 2.14: Power spectrum of the slave lasers synchronized to different IM-FM sidebands.

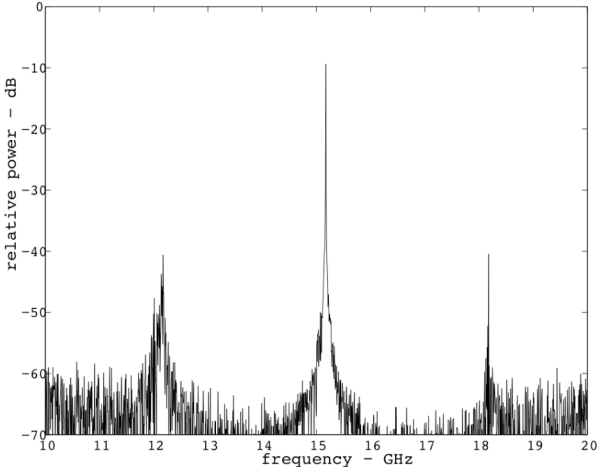


Figure 2.15: Power spectrum of the beat signal between the injection-locked slave lasers.

2.4 Conclusion

A model for describing injection locking in DFB semiconductor lasers was presented. The locking bandwidth together with the optically induced change was derived. It was found that the stable locking range depends on the DFB laser modal characteristics. Furthermore, the model predicts the optical injection characteristics in function of the power supply conditions and laser structure parameters. This theory was verified experimentally in chapter 4 and also compared to other experimental results, leading to a good agreement between theory and experiment. Besides the applications of the model presented through large-signal simulations, the model makes possible the study of phase noise rejection and spectral purity transfer in injected DFB lasers. Moreover, the model permits DFB laser design to favor injection locking according to the application expected.

2.5 References

- [1] O. Lidoyne, P. Gallion, C. Chabran and G. Debarge, "Locking range, phase noise and power spectrum of an injection-locked semiconductor laser," *IEE Proceedings*, vol. 137, no. 3, 1990.
- [2] R. Lang, "Injection *Locking* Properties of a Semiconductor Lasers," *IEEE J. Quantum Elec.*, vol 18, pp. 976-983, 1982.
- [3] I. Petitbon, P. Gallion, G. Debarge and C. Chabran, "Locking Bandwidth and Relaxation Oscillations of an Injection-Locked Semiconductor Laser," *IEEE J. Quantum Elec.*, vol 24, pp. 148-154, 1988.
- [4] R. Hui, A. D'Ottavi, A. Mecozzi and P. Spano, "Injection Locking in Distributed Feedback Semiconductor Lasers," *IEEE J. Quantum Elec.* , vol. 27, pp. 1688-1695, 1991.
- [5] C.H. Henry, N.A. Olsson et N.K. Dutta, "Locking Range and Stability of Injection Locked 1.54 μm InGaAsP Semiconductir Lasers," *IEEE J. Quantum Elec.*, vol 21, pp. 1152-1156, 1985.
- [6] N. Schunk et K. Petermann, "Noise Analysis of Injection-Locked Semiconductor Injection Lasers," *IEEE J. Quantum Elec.*, vol 22, pp. 642-650, 1986.
- [7] H. Kogelnik and C.V. Shank, "Coupled-Wave Theory of Distributed Feedback Laser," *J. Appl. Phys.*, vol 43, pp. 2327-1335, 1972.
- [8] G. Morthier, "An Accurate Rate-Equation Description for DFB Lasers and Some Intresting Solutions," *IEEE J. Quantum Elec.*, vol. 33, pp. 231-237, 1997.
- [9] J. Carroll, J. Whiteaway, and D. Plumb, *Distributed Feedback Semiconductor Lasers*. IEE and SPIE Press, London, 1998, pp. 116-126.
- [10] F. Favre, "Theoretical Analysis of External Optical Feedback on DFB Semiconductor Lasers," *IEEE J. Quantum Elec.*, vol 23, pp. 81-88, jan. 1987.
- [11] O. Lidoyne, P. Gallion et D. Erasme, "Modulation Properties of an Injection-Locked Semiconductor Laser," *IEEE J. Quantum Elec.*, vol 27, pp. 344-351, 1991.

-
- [12] X. Jun Meng, T. Jung, T. Chau, and M.C. Wu, "Gain and bandwidth enhancement of directly modulated analog fiber optic links using injection-locked gain-coupled DFB lasers," MWP, 1999, pp. 141–144.
- [13] S. Shimada, K. Nakagawa, M. Saruwatari, and T. Matsumoto, "Very-high-speed optical signal processing," Proceedings of the IEEE, vol. 81, 1993, pp. 1633-1646.
- [14] L. Shenping, K.T. Chan, and L. Caiyun "Wavelength switching of picosecond pulses in a self-seeded Fabry-Perot semiconductor laser with external fiber Bragg grating cavities by optical injection," IEEE Photonics Technology Letters, vol. 10, pp. 1094-1096, aug. 1998.
- [15] T. B. Simpson and F. Doft, "Double-Locked Laser Diode for Microwave Photonics Applications," IEEE Photonics Technology Letters, vol. 11, no. 11, pp. 1476-1478, nov. 1999.
- [16] A.J. Lowery and P.C.R. Gurney, "Comparison of optical processing techniques for optical microwave signal generation," IEEE Transactions on Microwave Theory and Techniques, Volume: 46 Issue: 2, Feb. 1998, pp. 142–150.
- [17] G. Stéphan, P. Besnard, M. Bondiou, R. Gabet, and M. Têtu, "Properties of a distributed feedback laser submitted to optical injection," Industrial Laser, 1999, pp. 28-37.
- [18] P. Gallion, G. Debarge, and C. Chabran, "Output spectrum of an unlocked optically driven semiconductor laser," Optics Lett., 1985, pp. 294-296.
- [19] H.L.T. Lee, R.J. Ram, O. Kjebon, and R. Schatz, "Bandwidth enhancement and chirp reduction in DBR lasers by strong optical injection," CLEO, 2000, pp. 99-100.
- [20] S. Piazzolla, P. Spano, M. Tamburrini, "Small signal analysis of frequency chirping in Injection-Locked Semiconductor lasers," IEEE J. Quantum Elec., vol 22, pp. 2219-2223, 1986.
- [21] L. Goldberg, R.D. Esman, and K.J. Williams, "Optical techniques for microwave generation, transmission and control," in IEEE MTT-S International, 1990, pp. 229–232.
- [22] P. Gallion, H. Nakajima, G. Debarge, and C. Chabran, "Contribution of spontaneous emission to the linewidth of an injection-locked semiconductor laser," Electron. Lett., 1985, pp. 626-628.

Chapter 3: **Experimental Study I, Laser Characteristics and Injection Locking Properties**

To investigate optical generation of microwaves using the sideband injection locking technique, a full characterization of the DFB semiconductor lasers used is first required. Moreover, the specific injection locking properties have to be determined in order to assure stable RF properties. In addition, complex index changes in a DFB semiconductor laser due to an external optical injection are investigated using an optical low-coherence reflectometer.

3.1 Description of DFB semiconductor lasers used

The semiconductor lasers used on all experiences were provided by Alcatel R&I and are index-coupled buried ridge stripe multi-quantum well DFB lasers. Their structure is shown in Figure 3.1. It consists of two sections: one contains a straight section with the Bragg grating and the other a tapered section that works as a spot-size converter to reduce fiber/laser coupling losses. In the tapered section, the width of the active MQW layer is linearly decreased as the passive waveguide underneath it increases. In this manner, the optical mode is transferred from the active MQW layer to the passive waveguide. A mean divergence angle of 15° degrees is obtained when the tip width of the active region is 200 nm at the left facet. The active layer consists of six 8 nm thick undoped InGaAsP strained multi-quantum wells and five 10 nm thick unstrained InGaAsP barriers. An antireflection and high-reflectivity coatings have been applied to the front- and end-facet, respectively. As a result, a high front-to-back emission ratio is obtained making the structure deliver high powers through the front facet. The device fabrication process is described in [1].

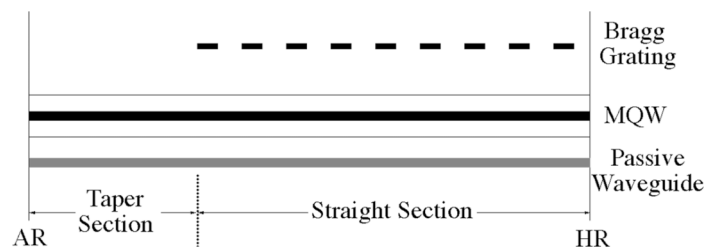


Figure 3.1: DFB Laser structure

3.1.1 Laser Chip Assembly

To guarantee stable laser operation, the assembly shown on Figure 3.2 was adopted. The tapered lensed fiber enables a simple and good coupling of the laser output power. The fiber is firmly mounted on a base having three degrees of liberty in translation, whereas the laser chip is mounted in a base having two degrees of liberty in translation and one in rotation. This assures a great adjustment precision and generally less than two minutes are required to obtain the same power coupled to the fiber than the day before for a given biasing

current. The electrical needle used to inject carriers through the laser contact has a miniature spring system to ensure a constant pressure on the contact. It is well known that the contact resistance is very vulnerable to temperature fluctuations and, consequently, so is the emission frequency of the laser. The whole assembly was then placed on a wooden box so as to avoid frequency variations due to air currents. A Peltier cooler is sandwiched between two copper blocks to control the temperature of the laser. A $10\text{ k}\Omega$ thermistor (Wavelength Electronics model TCS610) was inserted in the copper block just beneath the laser chip to monitor its temperature. The operating temperature on all experiences was set between 20° and 30° C with a short-term stability better than 0.005° C provided by the temperature controller (Microwave Electronics model MPT-5000). As a result of this assembly, the output power stability is better than 0.01% in a minute and better than 0.3% in an hour.

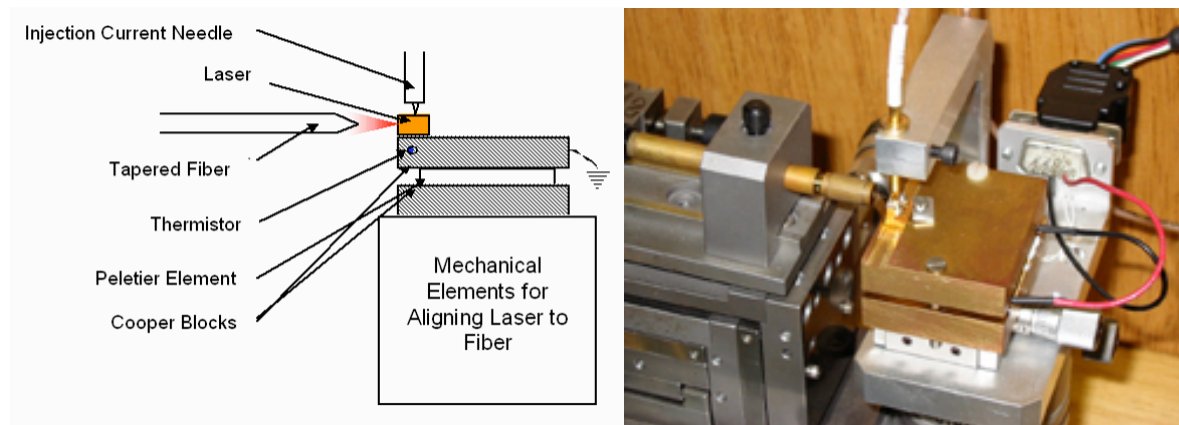


Figure 3.2: Mechanical assembly

3.1.2 Static Characteristics

The power/current characteristics of device 72114A.209 and its spectrum for a 70 mA bias are shown on Figure 3.3 for a temperature of 25° C . The power readings indicate the power coupled to the fiber. Comparing this measured data with the data provided by the manufacturer, a total fiber/laser coupling loss of 6.8 dB is obtained. The slope efficiency was found to be 0.25 W/A and the threshold current 9.4 mA. The side-mode suppression ratio is better than 50 dB for a power output of 18 mW.

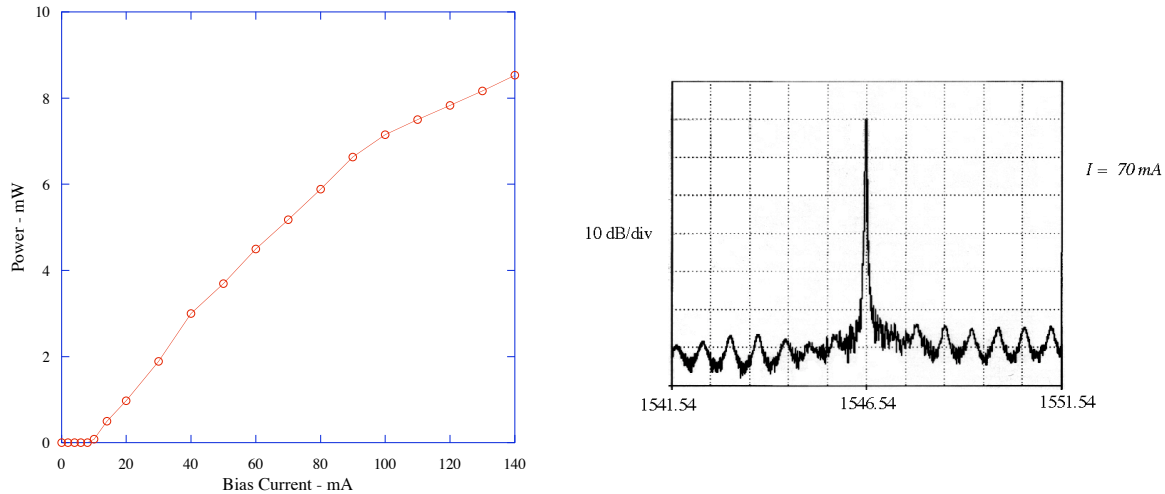


Figure 3.3: Power-current characteristics of the laser diode and its optical spectrum above threshold.

For injection locking experiences, lasers having approximately the same wavelength are required. This is a difficult task, even if the lasers come from the same wafer. Nevertheless, frequency control done through temperature for wide tuning and through the biasing current for fine tuning allows for frequency matching between the master and slave laser. Precise frequency dependence on temperature and on the bias current has then to be established. These measurements were performed with an optical spectrum analyzer (Advantest Q8384) having a resolution of 0.01 nm at a wavelength of 1550 nm. On Figure 3.4, the wavelength dependence on bias current is represented for three different lasers, all fixed at a temperature of 25° C. The frequency change resulting from a change in the biasing current is then $\sim -1.63 \text{ GHz/mA}$. It should be noticed that increasing the injection of charge carriers into the laser causes a decrease of wavelength as the carrier density rises and reduces the refractive index, but on a longer time scale the wavelength increases because of the rise in temperature induced by the additional current. The temperature of importance is that of the active area, which could differ from that of the heat sink by 2-10°C because of the heating from injected carriers [2].

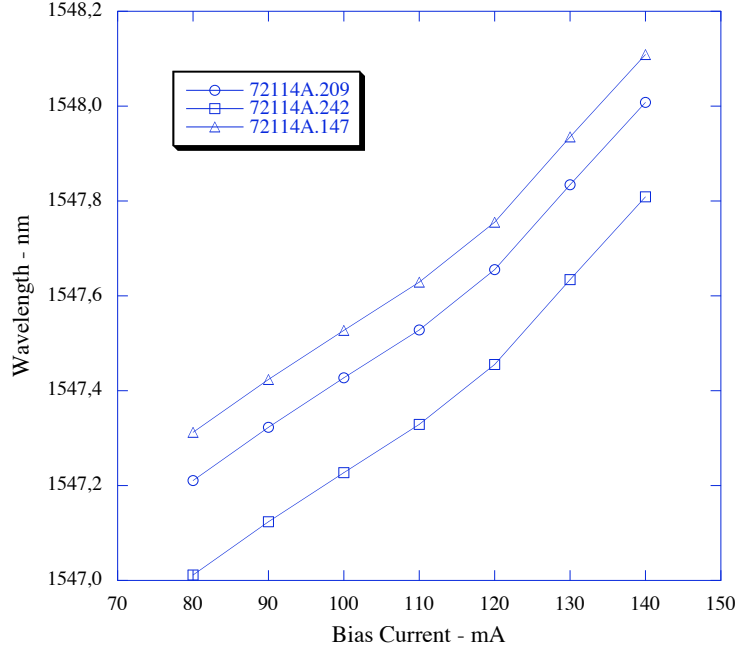


Figure 3.4: Wavelength dependence on biasing current

On Figure 3.5, the wavelength dependence on temperature is represented for three different lasers, all biased at 110 mA. The temperature showed is that measured by the thermistor. In frequency, the slope is measured to be ~ -11 GHz/ $^{\circ}$ C. There is considerable interest in understanding the changes in laser performance as temperature changes [3]. An estimate of the temperature coefficient of wavelength may be given by [4]:

$$\frac{\Delta\lambda}{\lambda_0\Delta T} = \frac{\Delta\Lambda}{\Lambda\Delta T} + \frac{\Delta n_{eff}}{n_{eff}\Delta T} \quad \text{Eq. 3.1}$$

where λ_0 is the Bragg wavelength in free space for the maximum reflection and $\Lambda = \lambda_0/(2n_{eff})$ is the spatial period of the effective refractive index n_{eff} . The material expansion coefficient, given by the first term of the right side of Eq. 3.1, for InP between 0° C and 100° C is $\sim 4.5 \times 10^{-6} \text{ K}^{-1}$. It is often ignored because it is an order of magnitude smaller than the coefficient of refractive-index change with temperature (second term of Eq. 3.1). This coefficient is difficult to measure close to the bandgap due to strong lattice resonance effects. Estimates of this coefficient are in the order of $6 \times 10^{-5} \text{ K}^{-1}$ for InP around 1530 nm leading to the conclusion that wavelength increases with temperature because the refractive index becomes larger. From the practical view of stabilizing the laser optical output, the effect of temperature on the threshold is most important. Although reduction in gain with temperature increases the threshold, the more significant increase with temperature arises

because of: (i) carrier leakage over the heterojunction barriers, (ii) increased recombination at material interfaces, (iii) increased non-radiative recombination, but specially (iv) increased Auger recombination which rises more rapidly with temperature than any of the other effects [4].

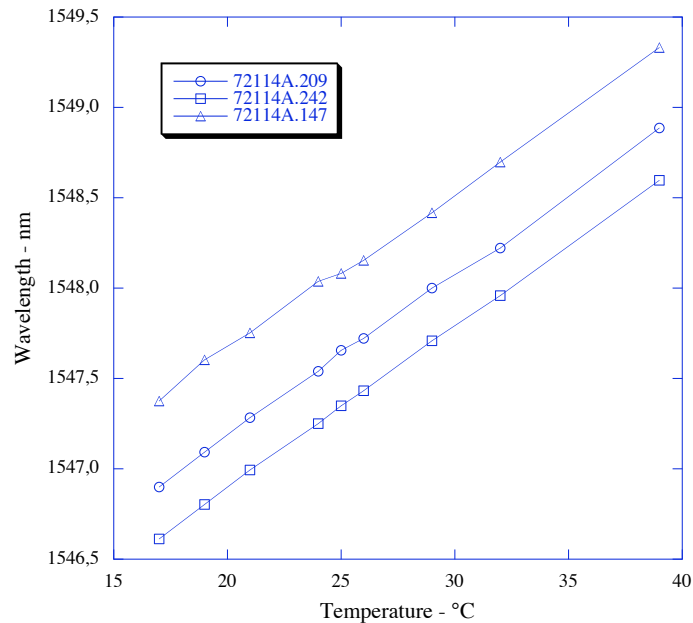


Figure 3.5: Wavelength dependence on temperature

3.1.3 Modulation Properties

The modulation properties of semiconductor lasers have been exhaustively studied in recent years. It is well known that direct intensity modulation is always accompanied by frequency modulation because of the refractive index dependence on carrier density. In the sideband injection locking technique for optically generating microwaves, the master laser is directly modulated via its injection current at a subharmonic of the RF carrier frequency. The maximum modulation frequency in the experimental setup is limited by the 3-dB bandwidth of the coaxial cable used to inject carriers into the laser (Figure 3.2). This bandwidth was measured to be 6.3 GHz, which is lower than the intrinsic relaxation oscillation frequency of the laser. The slave lasers have to be synchronized then, to two distant modulation peaks. The modulation index of the master laser should be high enough so as to have a "sufficient"

number of modulation peaks and with "sufficient" power as it will be explained in the next chapter.

An RF signal generator is used to sinusoidally modulate the laser at a frequency of 2-5 GHz via its injection current. Since there is no impedance matching between the RF generator and the laser diode, only a small portion of the generator power is injected to the laser cavity. The rest is either reflected back to the generator or radiated by the injection needle which functions as an antenna. To estimate the resulting modulation depth for a given power of the RF generator, the fundamental peak wavelength change, due to the presence of the effective modulation current, is measured using an optical spectrum analyzer. Then, using the wavelength dependence on bias current from Figure 3.4, the effective modulation current is calculated. For a biasing current of 80 mA, a 3 GHz modulation frequency, and an electrical power of the RF generator of 0 dBm an effective modulation current of 10.5 mA is found, giving a modulation depth ~13%. The optical spectrum of the modulated master laser for these conditions is found in Figure 3.6. In order to increase the relative power of each modulation sideband, an electrical amplifier with a 35-dB gain and 10-W saturation power was used to amplify the RF generator signal before applying it to the laser. The modulated power applied to the laser was adjusted to 36 dBm. The resulting optical spectrum is shown in Figure 3.7, where three effects are confirmed: (i) the total power has increased, (ii) the fundamental peak wavelength has shifted by 0.1 nm, and (iii) the relative power of distant sidebands has increased. All this is due to the increase of the effective modulation current. The modulation depth in this case is estimated to be ~24%. Given the relatively low power of distant sidebands, an EDFA amplifier can be used to considerably increase this power.

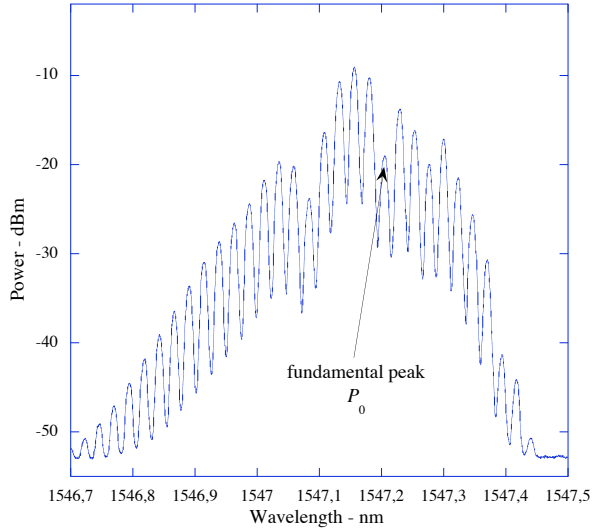


Figure 3.6. Modulated master laser optical spectrum with no drive current amplification.

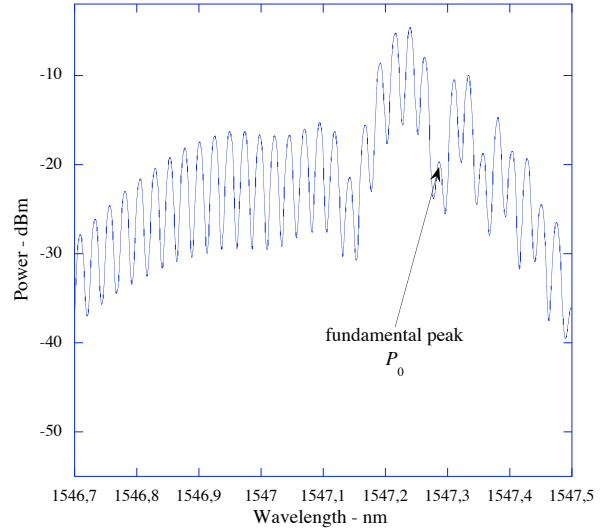


Figure 3.7. Modulated master laser optical spectrum with drive current 35 dB amplification.

3.1.4 Laser Linewidth

In the sideband injection locking technique, and more generally, for any heterodyne detection scheme, the link performance is limited by the phase correlation between the transmitted signals. It is then important to characterize the semiconductor lasers used in terms of their phase noise. Recalling, a random increase in the spontaneous emission reduces the carrier density and hence reduces the gain, which reduces the mode intensity allowing the carrier density to recover to reestablish the round-trip gain close to unity. Fluctuations in the net gain are limited, it is the phase fluctuations that are important and add to the linewidth through frequency modulation. Given the stationary nature of the phase noise $\Delta\phi(\tau)$, the second order moment σ_ϕ of the phase fluctuation probability density, is sufficient to characterize the phase noise. Its dependence on linewidth of the spectrum can then be used to estimate the linewidth enhancement factor α_H . All this leads to the necessity of measuring the laser linewidth.

The self-homodyne technique [5] was used to measure the laser linewidth. The setup is illustrated on Figure 3.8. The laser diode is directly modulated with a generator power of – 10 dBm at a frequency of 500 MHz. The optical output is coupled to a Mach-Zehnder interferometer with only a delay line on one of its arms. The signal is detected by a p-i-n

photodiode (22 GHz bandwidth) and measured with an electrical spectrum analyzer. If the delay τ_0 is greater than the coherence time of the lasers $1/\Delta\nu$, the delayed field decorrelates from the non-delayed field and the measured spectrum represents the laser power spectrum. Under these conditions, the linewidth of the modulation sidebands equals twice the linewidth of the laser.

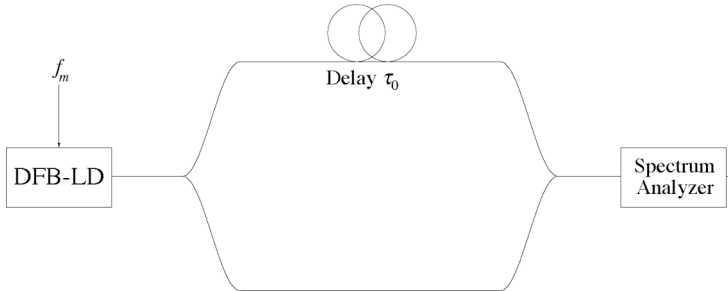


Figure 3.8: Self-homodyne technique for measuring the laser linewidth.

The measured spectrum is shown on Figure 3.9 where the first two modulation sidebands are shown. The measured linewidth of a modulation sideband is twice the linewidth of the laser, which was measured to be ~ 946 kHz.

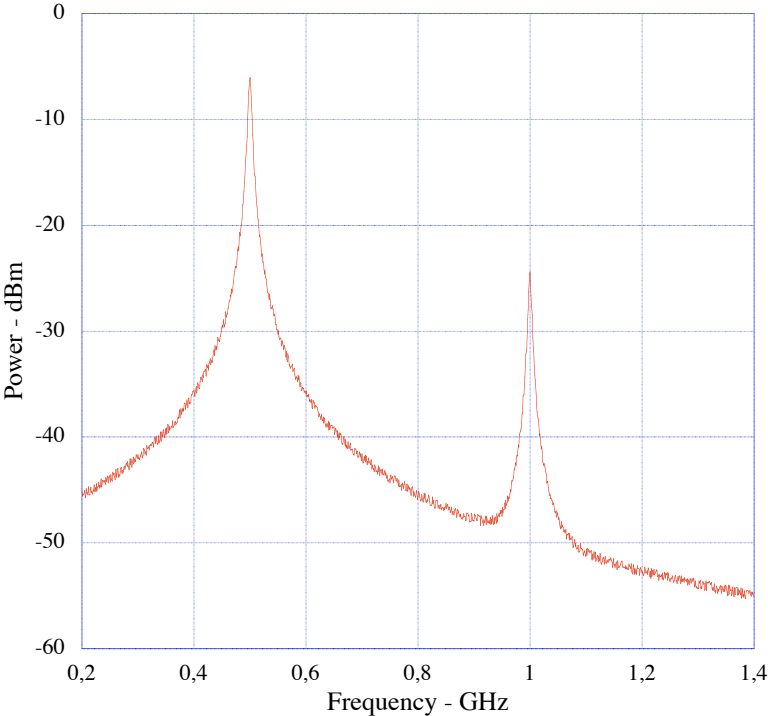


Figure 3.9: Self-homodyne spectrum.

3.2 Injection Locking Characteristics

The interest here in studying the injection locking properties of semiconductor lasers is basically to synchronize the slave laser to a master laser. In unconditional stable conditions, as seen in chapter 2, the slave laser frequency and phase follow that of the master laser. In this manner, the master laser can be used to frequency synchronize and phase correlate several slave lasers.

The experiments performed here were all done using standard single-mode optical fibers, as opposed to having the light travel in free space. The problem with free-space configurations, is the uncertainty of the spatial overlap between the optical mode in free space and in the slave laser waveguide. With such systems it is difficult to estimate the injected optical power and is incompatible with modern measurement equipment. By using the fiber optics setup, model and measurements can be linked together using a simple formula without the indirect methods normally used in free-space systems (e.g. four-wave mixing sideband comparison [6,7], gain measurement [8]).

3.2.1 Schema and Control Parameters

To experimentally study the dependence of the stable locking bandwidth on the injection conditions, the setup shown in Figure 3.10 was adopted. Two types of laser were used as the master laser to compare results between different isolation and different laser linewidths. The first laser is a commercial Alcatel laser 1915LMI (isolation ~ 30 dB, $\Delta\nu \sim 5$ MHz) and the second laser is laser 72114A.209 previously described (isolation ~ 60 dB, $\Delta\nu \sim 1$ MHz). The master laser output is coupled to a tapered lensed fiber and an attenuator placed between the isolators is used to control the injected optical power. The lasers current and temperature are adjusted to establish a desired frequency detuning. Reflected feedback into the laser cavities is avoided by splicing the fibers instead of using connectors and by using isolators with better than 60 dB of isolation. The overall fiber length

between the master and slave laser is about 5 m and reflections due to Rayleigh back-scattering are estimated to be 50 dB below the free-running laser power.

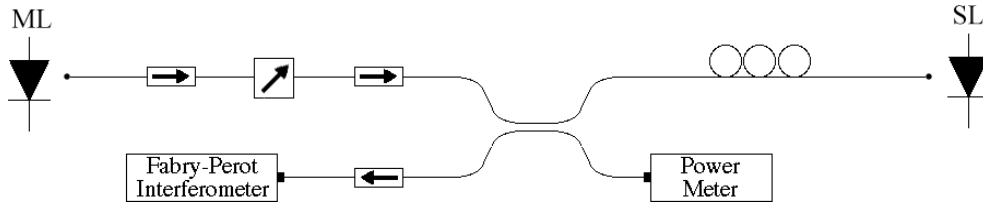


Figure 3.10: Setup for injection locking experiments.

The polarization of the intracavity and the injected fields has to be identical in order to maximize their interaction and to avoid polarization switching between TE and TM modes. The effect of polarization on the locking bandwidth in DFB semiconductor lasers has been previously studied [9]. Mainly, the locking bandwidth decreases and the static/dynamic limit increases as the injected field polarization becomes perpendicular to the slave laser. Exact polarization matching is then not necessary for the considered applications. Nevertheless, polarization matching is optimized by adjusting the polarization controller to maximize the power of the relaxation oscillation sidebands appearing typically for strong injection rates. Surely, the slave laser could be replaced by a linear polarizer and maximization of the master laser output power by adjusting the polarization controller would guarantee parallel polarization at the interface [10]. Unfortunately, the mechanical assembly makes this task difficult.

3.2.2 Locking Bandwidth

Measurement of the locking bandwidth is usually done by varying either the slave or the master laser biasing current until reaching the locking bandwidth edge and then evaluating the frequency change due to a current change. The problem with this method is that the injection rate changes as the biasing current is varied. An alternative method is proposed here to overcome this problem consisting in varying the injected optical power for a fixed frequency detuning. The free-running slave laser power remains constant, so that the master laser power is proportional to the injection rate.

Simultaneously observing the master and the free-running slave laser spectrum on a Fabry-Perot interferometer allows for direct measurement of the frequency detuning within the spectral-free range (~ 50 GHz) and with a precision set by the interferometer resolution (~ 15 MHz). In this manner, the master laser current is first adjusted to achieve a desired frequency detuning. The master laser is then unplugged from the interferometer and plugged to a power meter and to the slave laser fiber for injection. Next, the injected power is varied by means of the attenuator and recorded when the edge of locking bandwidth is reached. It is relatively easy to see when the locking bandwidth is reached because the slave laser frequency synchronizes to the master laser frequency. For example, in Figure 3.11, the unlocked slave laser spectrum presents modes at the free-running frequency, at the master laser frequency, and at its opposing frequency with respect to that of the free-running laser. Increasing the injected optical power in small steps (~ 0.01 dB) eventually leads to a locked state where all the slave laser power is concentrated at the master laser frequency. Further increasing the injected optical power drives the laser to an unlocked state where undamped relaxation oscillations and chaotic behavior are observed. For this experiment the commercial laser (1915LMI) was used as the master laser. The periodic noise found on the spectrum is due to feedback in the master laser. Replacing the commercial laser with laser 72114A.209 that has 60 dB of isolation confirms this. Consequently, laser 72114A.209 will be used as the master laser for the remaining experiments.

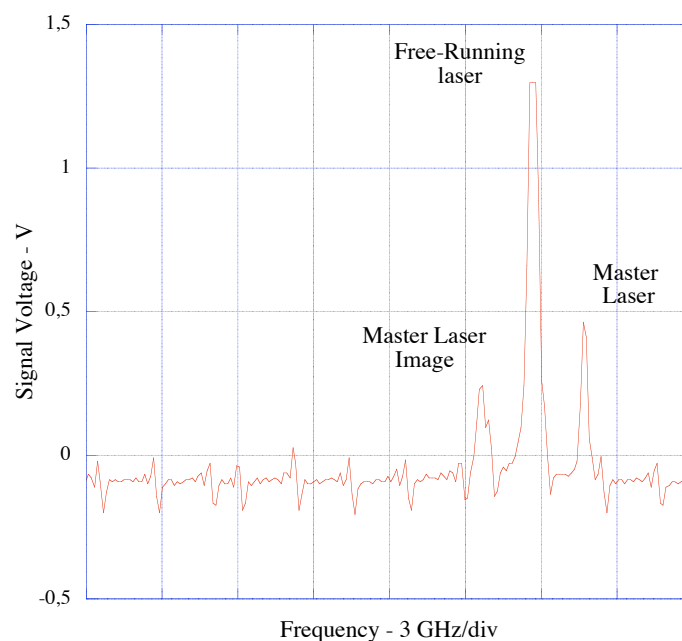


Figure 3.11: Non-synchronized slave laser spectrum.

Following the procedure described above, the locking bandwidth was measured in function of the injection rate and Figure 3.12 represents these results. The biasing current of the slave laser (72114A.147) was fixed at 90 mA while the master laser current and temperature were adjusted so as to make the frequency detuning small (< 10 GHz). It was found that the transition from the locked to the unlocked state is very sharp in the symmetric region *i* at weak injection, but gets more and more fuzzy for positive detunings at higher injection, where undamped relaxation oscillation sidemodes occur (regime *iii*). Description of the different injection regimes together with their characteristic power spectrum will be discussed in the next section.

In reality, precise knowledge of the absolute injected photons into the slave laser cavity is not essential for optical generation of microwaves. Nevertheless, evaluation is possible by fitting the measured data to theoretical results or by alternative methods [10,11] that will require considerable modifications of the experimental setup. The important feature searched here is a way to guarantee the repeatability of measurements from one day to another. This is done by carefully adjusting the tapered lensed fiber assuring that the power coupled into the fiber is always the same for a given biasing current. As long as the fibers remain unmoved the injection conditions can be reproduced to yield comparable results from one day to another.

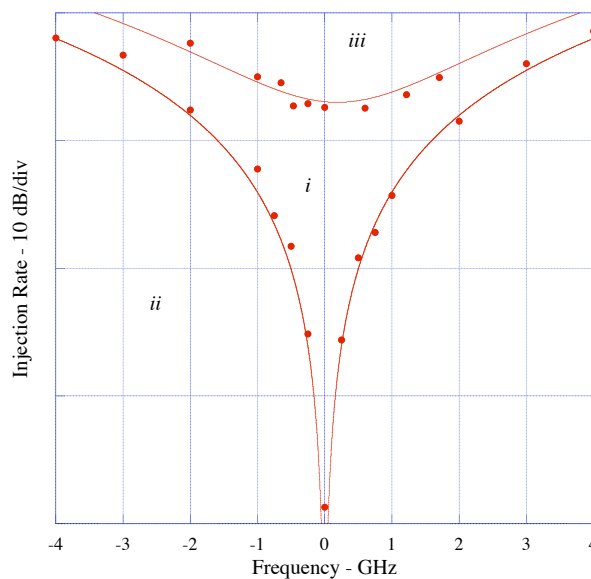


Figure 3.12: Theoretical fit (continuous line) and measured data (dots) of the locking bandwidth.

3.2.3 Injection Regimes

Four injection regimes were distinguished. In region *i*, locking is unconditionally stable for low injection rates. A typical power spectrum of the locked slave laser is shown in Figure 3.13 where the frequency detuning was made zero and the injection rate is estimated to be ~ -42 dB. The most striking feature in this regime is that the locking bandwidth is symmetrically centered on the frequency of the free-running laser. With the same injection rate of -42 dB, the frequency detuning was increased to around 3 GHz. The power spectrum for these conditions is shown on Figure 3.14 where the free-running mode, the master laser mode, and its image can be distinguished. This regime (*ii*) corresponds to an optically induced modulation regime and not to four-wave mixing as it is frequently described. The reason is that only one mode is injected to the slave laser and the appearance of master laser image in the power spectrum is explained by the optically induced modulation of the refractive index, which depends on carrier density.

For a higher injection rate (~ -27 dB) and zero frequency detuning the relaxation oscillation sidebands start to appear, as can be seen in Figure 3.15. The exact definition of the frontier between regions *i* and *iii* from a practical point of view is uncertain because the injection rate necessary for the sidebands to appear is limited in the experiment by the dynamic range of the interferometer (~ 20 dB). The limit is then taken experimentally when the relaxation oscillation sidebands become visible. Further increasing the injection rate to around -21 dB and keeping the frequency detuning equal to zero, a chaotic behavior is obtained in the power spectrum (Figure 3.16). The transition between undamped relaxation oscillations and chaotic behavior is quite abrupt. Experimentally, it is arbitrarily defined when the relaxation oscillation peaks are 20 times lower than the free-running slave peak. All these measured spectra have a correspondence with the theoretically obtained in chapter 2. Exact comparison, however, requires a slight modification of the laser structure simulated to describe the actual lasers used. The theoretical results were obtained way before the arrival of the lasers to the lab.

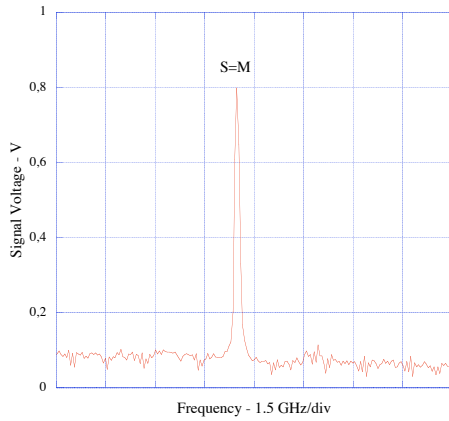


Figure 3.13: Stable locking (i).

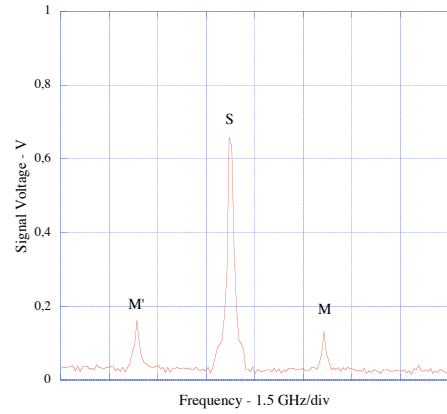


Figure 3.14: Unlocked slave laser spectrum (ii).

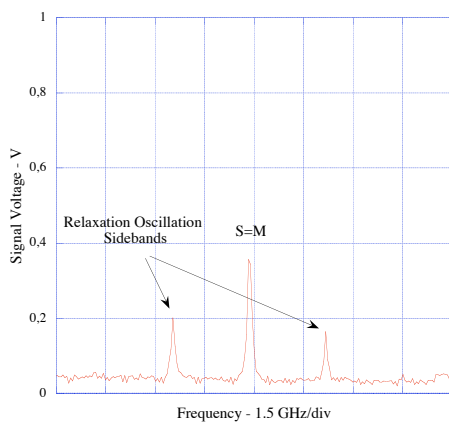


Figure 3.15: Relaxation oscillations sidebands (iii).

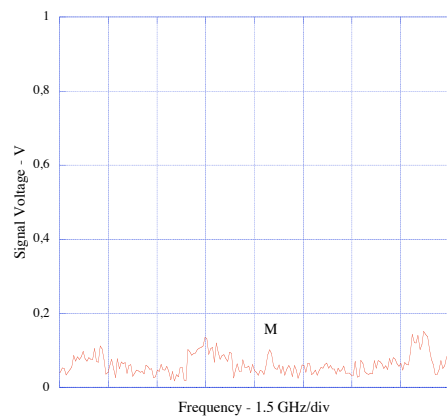


Figure 3.16: Chaotic behavior (iii).

3.3 Optically Induced Index Changes

Taking advantage of the lab resources, optically induced index changes were measured with an optical low-coherence reflectometer (OLCR) mounted by C. Palavicini. The OLCR allows detection, localization, and quantification of scattering discontinuities and manufacturing irregularities in photonic devices [12-14]. With a special set-up involving a precise control of the optical path difference (OPD) between the two arms of the interferometer, the complex reflectivity of the Device-Under-Test (DUT) can be measured, thus enabling exact determination of spatial phase-shifts and spectral characteristics like chromatic dispersion and group delay.

Since external optical injection of active devices is becoming an essential technique in all-optical networks and in future broadband wireless access systems, it is interesting then to characterize these devices using the OLCR. With external optical injection, optical functions such as phase recovery using self-pulsating lasers, multi-wavelength conversion in SOAs, high-speed dispersion compensation, or remote generation and control of RF signals using DFB lasers can be accomplished. This requires an understanding of how the semiconductor device reacts to an optical injection. The proposed phase-sensitive OLCR allows a full characterization of active devices under operation. In particular, the complex index changes in a DFB semiconductor laser due to an external optical injection were measured and will be presented here after a brief description of the OLCR.

3.3.1 OLCR Technique

A phase-sensitive OLCR is basically a Michelson interferometer illuminated with a broadband source (BBS) with a translating mirror in one of its arms and the DUT in the other (Figure 3.17). The BBS is a superfluorescent source based on an Er^{3+} doped fiber amplifier. The spatial resolution is limited by the coherence length of the BBS, i.e. $\Delta l = 3.5 \mu\text{m}$. The DUT is laser 72114A.147. The reflectogram is obtained by varying the OPD at a constant velocity. The mirror scanning speed is 1 mm/s. The interference fringe-pattern corresponding to a localized position inside the DUT is detected with a low-noise PIN-FET photodetector (PD) when the OPD is less than the coherence length of the BBS. In order to keep track of the absolute position of the reference mirror (M1), a coherent interferometer signal is used as a zero-crossing trigger allowing to periodically sample the OLCR data as it is recorded in a computer (PC). The 633 nm He-Ne laser wavelength determines a 316 nm sampling period for the measurement points. The phase shift of a known π -phase-shifted fiber grating was measured with a very good accuracy ($<2\%$), thus validating the phase-sensitive OLCR.

All measurements were performed with a scanning distance of 2.5 mm, which is slightly longer than the optical length of the DUT. It should be noticed that the distance representing the scanning position is in air and it should be corrected by the effective group refractive index to obtain the physical distance.

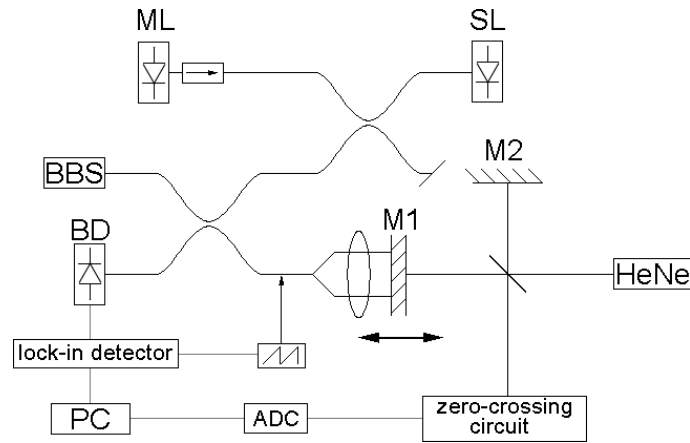


Figure 3.17: Experimental setup for the OLCR measurements.

3.3.2 Reflection Coefficient of a DFB Laser

In order to understand experimentally obtained reflectograms of the DFB laser, a theoretical reflectogram $R(x_{opt})$ is calculated by means of the device reflectivity $r(f)$. The reflectogram and the reflectivity form nearly a Fourier transform pair, so that:

$$R(x_{opt}) = \int_{-\infty}^{+\infty} S(f)r(f)e^{j2\pi f\tau} df \quad \text{Eq. 3.2}$$

where $\tau = x_{opt}/c$ is the time difference between the two interferometer arms, x_{opt} is the optical path length, and $S(f)$ is the power spectral density of the BBS. The reflectivity coefficient of the DUT is calculated using the structure depicted in Figure 3.18.

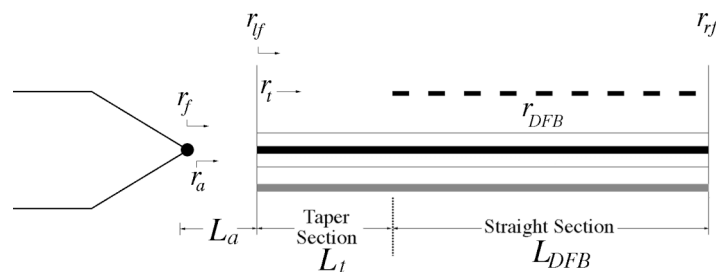


Figure 3.18: Structure used to calculate the reflectivity coefficient as seen from the fiber/air interface.

The reflectivity and transmission spectra of the grating can be easily calculated using the coupled-wave theory presented in chapter two. They are written as:

$$\begin{aligned} r_{DFB} &= \frac{j\kappa / \gamma \cdot \sin(\gamma L_{DFB})}{\cos(\gamma L_{DFB}) - (\alpha - j\delta) / \gamma \cdot \sin(\gamma L_{DFB})} \\ t_{DFB} &= \frac{1}{\cos(\gamma L_{DFB}) - (\alpha - j\delta) / \gamma \cdot \sin(\gamma L_{DFB})} \end{aligned} \quad \text{Eq. 3.3}$$

where L_{DFB} is the length of the grating section equal to $345 \mu\text{m}$ and the other parameters are as defined in chapter two. The reflectivity including the tapered section and the amplitude reflectivity of the right facet (0.99) is then given by

$$r_t = \frac{r_{DFB} - (r_{DFB}^2 - t_{DFB}^2) \cdot r_{rf}}{1 - r_{DFB} \cdot r_{rf}} \exp(j \frac{4\pi n_g L_t}{\lambda}) \quad \text{Eq. 3.4}$$

where $L_t = 135 \mu\text{m}$ is the length of the tapered section. Now, the total reflectivity of the laser structure as seen from the left facet is:

$$r_{lf}' = \frac{r_{rf}' - r_t}{1 - r_t \cdot r_{rf}'} \quad \text{Eq. 3.5}$$

where r_{rf}' is the left facet amplitude reflectivity taken as 0.01. Finally, the total reflectivity including the fiber reflection and the transmission in air distance is written as:

$$r_f = \frac{r_f' - r_a}{1 - r_f' \cdot r_a} \quad \text{Eq. 3.6}$$

where r_f' is the fiber end reflectivity taken as 0.005, $r_a = r_{rf}' \exp(j4\pi L_a / \lambda)$ is the reflectivity of the structure including the air distance $L_a = 79 \mu\text{m}$. The coupling factor κ of the grating is obtained by measuring the stop band and is approximately $\sim 20 \text{ cm}^{-1}$.

3.3.3 Free-Running Lasers at 0 mA Bias

Figure 3.19 represents the measured OLCR data for the free-running laser biased at 0 mA. The fiber and front facet reflection peaks can be clearly distinguished and are separated by $79 \mu\text{m}$. The actual laser cavity is composed of a tapered straight section and an active Bragg grating section as can be seen in the phase reflectogram in Figure 3.21. Dividing the optical length of the device as measured in the reflectogram by the physical length provided by an atomic force microscope, the effective group refractive index is obtained (~ 3.35). The slope of the reflectogram in the grating section is due to absorption losses of the injected light. The amplitude reflectogram, shown in Figure 3.20, was calculated for several cavity losses. It was found that in this section, the loss is nearly equal to half the slope observed and it is measured to be 6 dB/mm for a biasing current of 0 mA (Figure 3.19). Using the law $P(z) = P_0 e^{-\alpha z}$, the absorption coefficient is estimated at 40 cm^{-1} . Since the phase increases linearly inside the grating section it is deduced that the coupling grating is uniform. The small irregularities observed near the rear facet are due to a grating phase mismatch with respect to the facet. It is important to notice that the different section lengths are better determined from the phase results when the laser diode is biased around threshold [13].

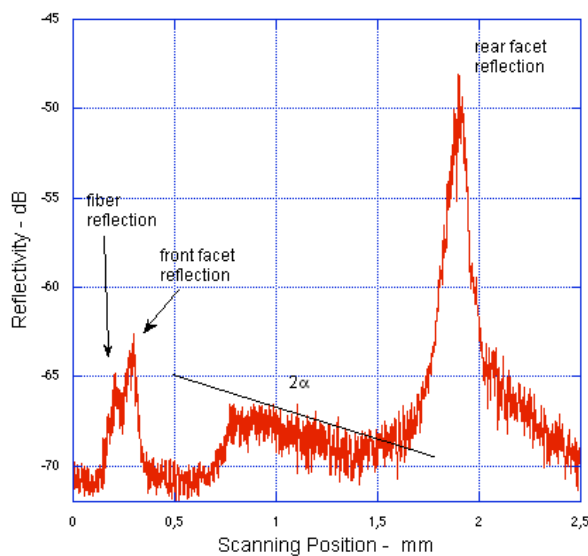


Figure 3.19: Measure magnitude of the OLCR data.

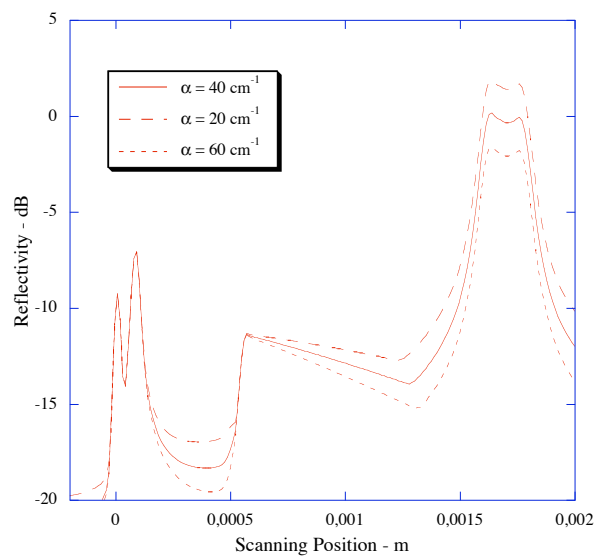


Figure 3.20: Theoretical OLCR data.

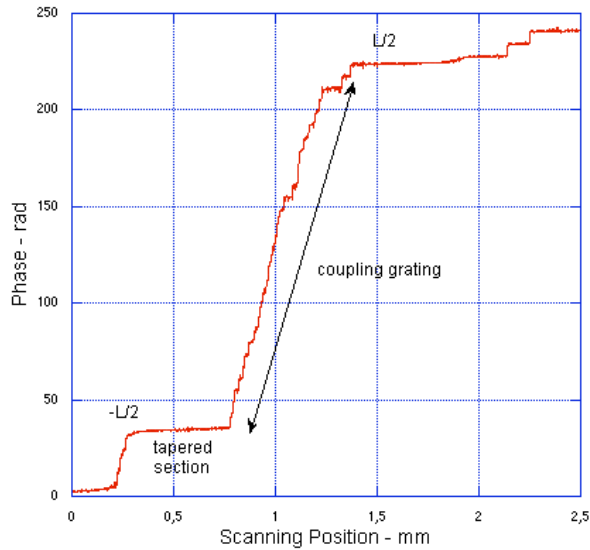


Figure 3.21: Phase of the OLCR data.

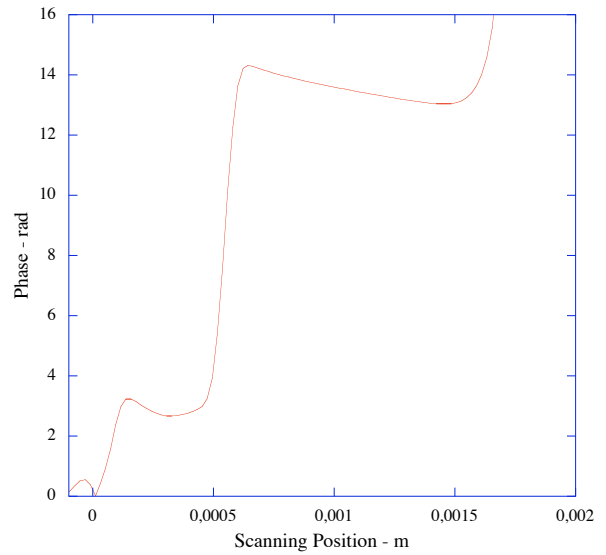


Figure 3.22: Theoretical phase of the OLCR data.

3.3.4 Free-Running Lasers Above Threshold

The amplitude reflectogram obtained for a free-running laser biased just above threshold is depicted in Figure 3.23. The difference between two consecutive minima (m_1 and m_2) is known as the beat length (L_B) and can be used to calculate the refractive index modulation of the grating, $\Delta n = \lambda_0 / 2L_B$. For this case, $\Delta n = 2.12 \times 10^{-3}$ is measured. Taking this measurement into account, the coupling coefficient determination yields $\kappa = 42 \text{ cm}^{-1}$, which is almost twice the value provided by the manufacturer. This coefficient is defined as $\kappa = \pi\Delta n / \lambda_0$ [15]. To obtain the true κ value, simulations were carried out (Figure 3.24) showing that the beat length should be divided by two. The logarithmic difference between Figure 3.23 and Figure 3.19 gives the net gain change due to an increase in current (0.4 dB/mA) [16].

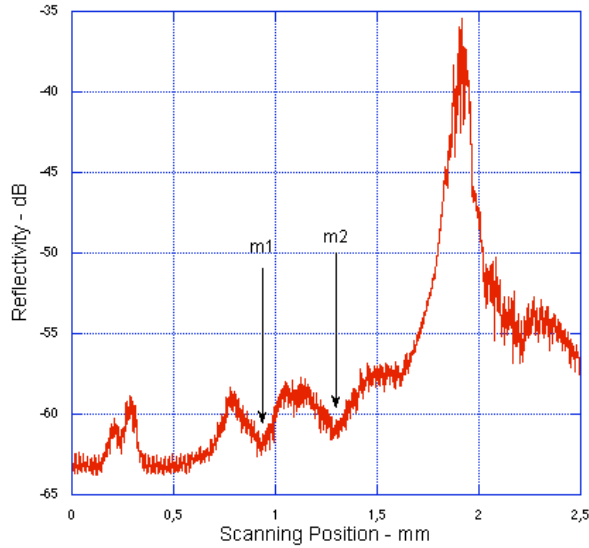


Figure 3.23: OLCR data above threshold.

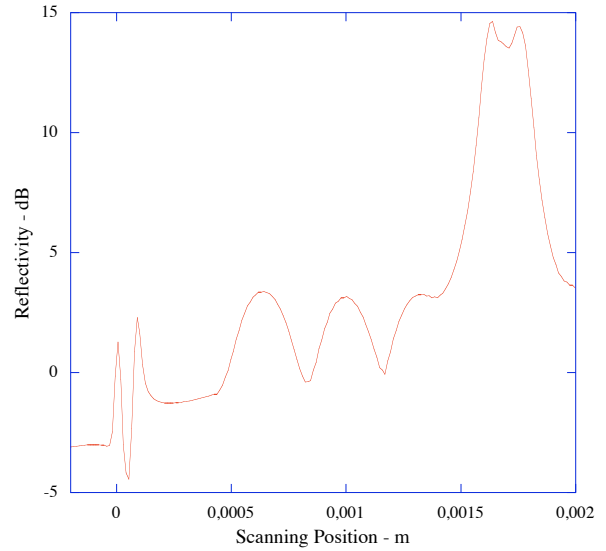


Figure 3.24: Calculated reflectogram above threshold.

3.3.5 Injection-Locked Lasers

When an external optical injection is applied to a semiconductor laser, the complex refractive index undergoes a perturbation inducing a variation of the emission frequency [17]. The imaginary part variation $\Delta n'' = -\lambda_0 / 2\pi \cdot \Delta g$ due to the injected field results is described by a gain change Δg , because the net gain is now different from the cavity losses. The linewidth enhancement factor relating the real and the imaginary variations of the refractive index causes, then, a static variation of the real refractive index $\Delta n' = \alpha_H \Delta n''$.

The reflectogram of an externally optical injected laser can be used to measure both, the real and imaginary variations of the refractive index due to injection. The reflectogram of an injected laser manifests an optical length change due to injection. Division by the physical length permits, then, to obtain the modification of the real refractive index $\Delta n'$. The logarithmic difference between the injected and free-running reflectograms determines the net gain change Δg due to injection. The determination of the imaginary variation of the refractive index is then straightforward. Figure 3.25 represents the measured variation of the complex refractive index in function of the injection rate for a small frequency detuning (~ 500 MHz). A mean linewidth enhancement factor of 2.86 was measured. In the theoretical calculation of the reflectogram, the reflectivity of the front facet was substituted with the

equivalent facet reflectivity obtained in chapter two to include the optical injection conditions. This caused a change in the net gain and a change in the optical length in the cavity thus assuring ac correspondance with measured data.

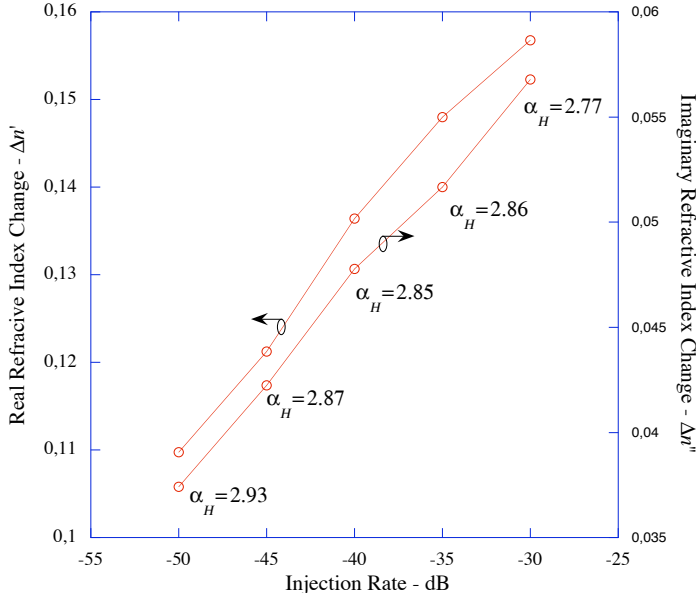


Figure 3.25: Complex index changes due to optical injection.

3.4 Conclusion

The DFB semiconductor lasers used on the experiments were characterized in terms of their static and dynamic characteristics. In addition, the injection locking properties of a slave laser were experimentally investigated yielding the locking bandwidth in function of the injection rate. This characterization will be useful in the next chapter where two slave lasers will be synchronized on the different modulation sidebands of a master laser. The method used to optically inject the slave laser guarantees repeatability and reproducibility of results. The OLCR technique was then used to obtain the complex-modal index changes due to injection. The linewidth enhancement factor of the laser is estimated to be ~ 2.86 . The technique allows the determination of the injection rate and linewidth enhancement factor by comparing to theoretical results for frequency and gain changes obtained in chapter two.

As a result of using high performance lasers, the strong mode selection of the DFB grating induces a symmetrical locking bandwidth. The reduced linewidth obtained thanks to the multi-quantum well material and the decreased damping time associated to the relaxation oscillations improve the locking characteristics. Namely, a larger range of injection rates and a wider locking bandwidth are permitted for unconditional stability operation.

3.5 References

- [1] V. Voiriot, B. Thedrez, J.L. Gentner, J-M. Rainsant, V. Colson, C. Duchemin, F. Gaborit, S. Hubert, J.L. Lafrayette, A. Piquier, L. Roux, B. Fernier, "1.55 μm High Efficiency Tapered DFB Laser Using UV 250 2-IN Technology Process," 11th Intern. Conf. On Indium Phosphide and Related Materials, 1999, pp. 33-36.
- [2] J. Carroll, J. Whiteaway, and D. Plumb, Distributed Feedback Semiconductor Lasers. IEE and SPIE Press, London, 1998, pp. 116-126.
- [3] X. Li, W.P. Huang, "Simulation of DFB semiconductor lasers incorporating thermal effects," *IEEE J. Quantum Electron.*, 1995, vol. 31, pp. 1848-1855.
- [4] J.A. Mccauley, V.M. Donelley, M. Vernon, I. Taha, "Temperature dependance of the near infrared refractive index of silicon, gallium arsenide and indium phosphide," *Phys. Rev. B.*, 1994, vol. 49, pp. 7408-7417.
- [5] D.M. Baney, P. Gallion, "Power Spectrum Measurement of a Modulated Semiconductor Laser Using Interfeometric Self-Homodyne Technique: Influence of Quantum Phase Noise and Field Correlation," *IEEE J. Quantum Electron.*, 1989, vol. 25, pp. 2106-2112.
- [6] T. B. Simpson, J. M. Liu, A. Gavrielides, V. Kovanis, and P. M. Alsing, "Period-doubling cascades and chaos in a semiconductor laser with optical injection," *Phys. Rev. A*, vol. 51, no. 5, pp. 4181–4185, 1995.
- [7] V. Kovanis, A. Gavrielides, T. B. Simpson, and J. M. Liu, "Instabilities and chaos in optically injected semiconductor lasers," *Appl. Phys. Lett.*, vol. 67, no. 19, pp. 2780–2782, 1995.
- [8] S. Kobayashi and T. Kimura, "Injection locking in AlGaAs semiconductor laser," *IEEE J. Quantum Electron.*, vol. QE-17, pp. 681–689, May 1981.

-
- [9] R. Gabet, G. Stéphan, P. Besnard, "Polarization effects in the laser response to a small injected field," PELS'2000, Southampton, U.K., Sept. 2000.
- [10] J. Troger, P.-A. Nicati, L. Thévenaz, and Ph. A. Robert, "Novel Measurement Scheme for Injection-Locking Experiments," IEEE J. Quantum Electron., vol. QE-35, pp. 32–38, Jan 1999.
- [11] G. Stéphan, P. Besnard, M. Bondiou, R. Gabet, M. Têtu, "Properties of a distributed feedback semiconductor laser submitted to optical injection," Industrial Laser'99, Wuhan, China, SPIE vol. 3862, pp. 28–37, Oct. 1999.
- [12] P.Y. Fonjallaz et al IEE Proc.-Optoelectron., 141 (1994), pp. 141-144.
- [13] U. Wiedmann et al J. Lightwave Technol., 16 (1998), pp. 1343-1347
- [14] Y. Gottesman et al J. Lightwave Technol., 20 (2002), pp. 489-493.
- [15] H. Kogelnik and C.V. Shank, "Coupled-Wave Theory of Distributed Feedback Laser," J. Appl. Phys., vol 43, pp. 2327-1335, 1972.
- [16] E. Brinkmeyer et al Opt. Lett., 17 (1992), pp. 1441-1443.
- [17] P. Gallion, H. Nakajima, G. Debarge, and C. Chabran, "Contribution of spontaneous emission to the linewidth of an injection-locked semiconductor laser," Electron. Lett., 1985, pp. 626-628.

Chapter 4: **Experimental Study II, Microwave Generation**

Laser synchronization by optical injection has proven to be an effective technique for generating phase-correlated signals. Consequently, generating and remote controlling RF signals by optically heterodyning two lasers injection-locked to different modulation sidebands of a master laser is a very attractive solution that is experimentally investigated in this chapter.

Although this technique has been experimentally demonstrated, the conversion efficiency, the differences between locking to adjacent and distant sidebands and the performance of the lasers remain key issues. This is important because desirable characteristics of optical-millimeter sources like wide and continuous tunability, high-output power after photo-detection, and spectral purity depend largely on the laser characteristics. Lasers with spectrally poor performance could be used since the phase correlation between the slave lasers cancels out the phase noise of the generated RF carrier. Nevertheless, we demonstrate that high-performance lasers can be very advantageous because the locking properties and the conversion efficiency are improved.

4.1 Experimental Procedure

The experimental setup shown in Figure 4.1 was used to optically generate and control microwaves. Reflected feedback into the laser cavities is avoided by splicing the fibers instead of using connectors and by using isolators with better than 60 dB of isolation. The modulating current was electrically amplified before applying it to the laser diode in order to have a better control of the modulation depth. Recall that there is no impedance matching between the RF generator and the laser diode. The modulated master laser power is injected to both slave lasers whose current and temperature are adjusted to tune them in to the desired modulation sidebands. The injected optical power is controlled by the attenuator placed between the isolators at the master laser output. An EDFA amplifier is used to increase the available power under distant modulation sidebands before injection power control via the attenuator. Polarization matching between the master and slave lasers is optimized using the technique described in chapter 3. The slave lasers output is analyzed using a Fabry-Perot interferometer, an optical spectrum analyzer and a pin photodiode coupled to an RF spectrum analyzer. The experiences will be limited to beating frequencies lower than 22 GHz, which is the bandwidth of the photodiode. Nevertheless, generalization of results can be extended to higher frequencies since the RF characteristics depend mainly on the locking conditions of the slave lasers to the modulation sidebands of the master laser.

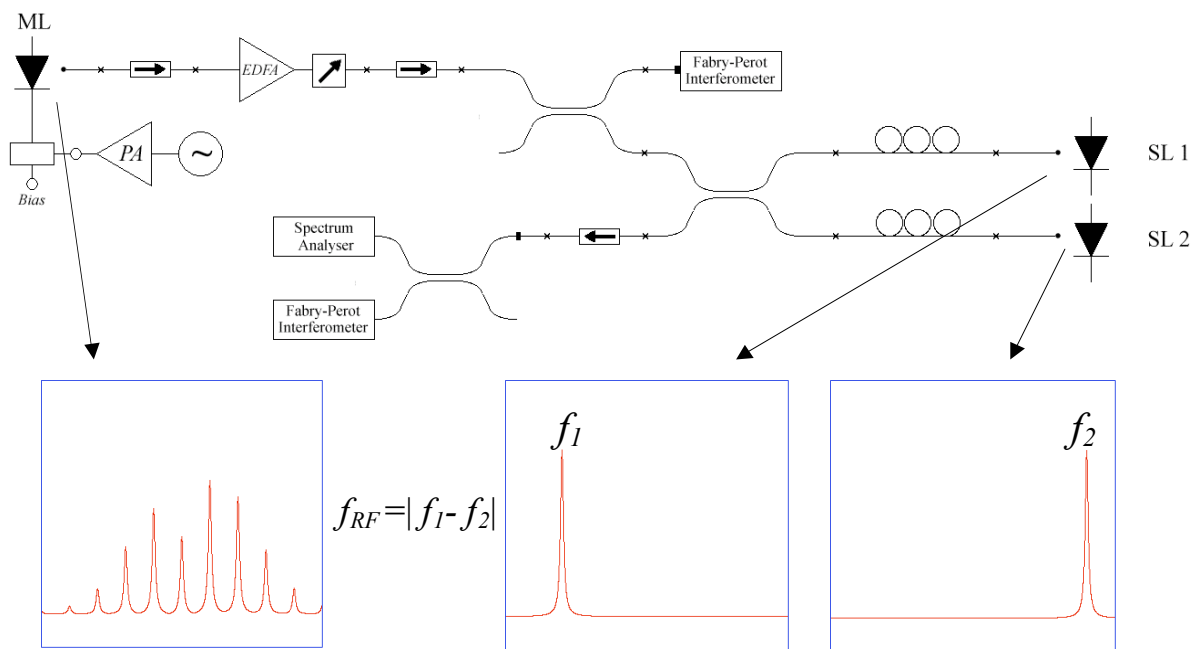


Figure 4.1: Experimental setup used to optically generate microwaves.

4.2 Modulation Conditions for the Master Laser

4.2.1 Master Laser Modulation

The optical spectrum of the modulated master laser in Figure 4.2 shows the different sidebands that may be used to lock each slave laser. A modulation frequency of 3 GHz and an electrical driving power of 36 dBm was used given that no impedance matching circuit was implemented (effective modulation depth $\sim 24\%$).

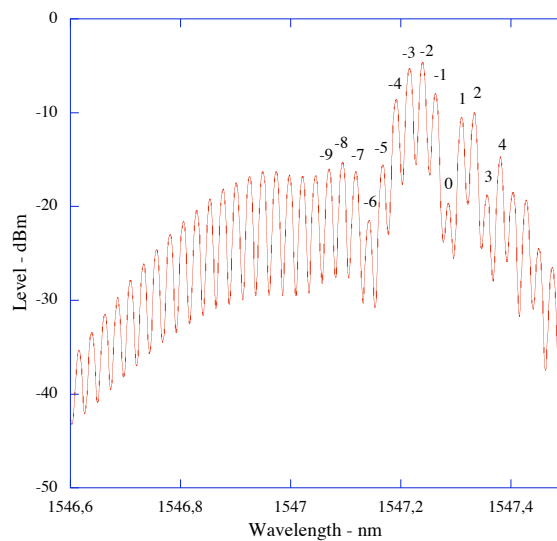


Figure 4.2: Optical spectrum of the modulated master laser.

These operating conditions as well as the choice of sidebands should be carefully selected to obtain the desired RF spectral properties. Several constraints on the modulation conditions have to be considered. First of all, the modulation frequency should be a subharmonic of the desired RF frequency. Low-frequency microwave oscillators (< 5 GHz) are preferred so as to keep the cost low and so as to modulate at a frequency lower than the laser bandwidth. The lower limit on the modulation frequency is fixed by the injection locking stability conditions of the slave laser to avoid bandwidth overlapping as it will be explained shortly. Conditions on the modulation depth should also be taken into account.

Basically, the power of the distant modulation sidebands used to lock each slave laser should be high enough in order to investigate spectral properties of the RF generated signal as the injected optical power is varied with the optical attenuator. Since the optical power is spread over a large number of modulation sidebands, an EDFA optical amplifier is used to increase the power under each sideband (Figure 4.1). Furthermore, it will be shown that the power of the sideband adjacent to the chosen sideband for injection locking is a mayor factor in avoiding signal degradation and frequency instabilities.

4.2.2 Free-Running Beating

The first experience realized was detecting the beat signal between the free-running lasers frequency separated by 15 GHz. Although the lasers are free from external optical injection, the master laser modulation was kept on to evaluate the impact of the high RF modulating power on the slave lasers. The modulating power of the master laser is quite high (~ 4 W) so that the desirable modulation depth is obtained. This modulation and the physical proximity of the slave lasers to the master laser provoke a parasitic modulation of the slave lasers. The radiated RF power from the injection needle of the master laser is captured by the injection needles of the slave lasers, thus modulating them. The impact of this on the RF spectrum is schematically explained by Figure 4.3.

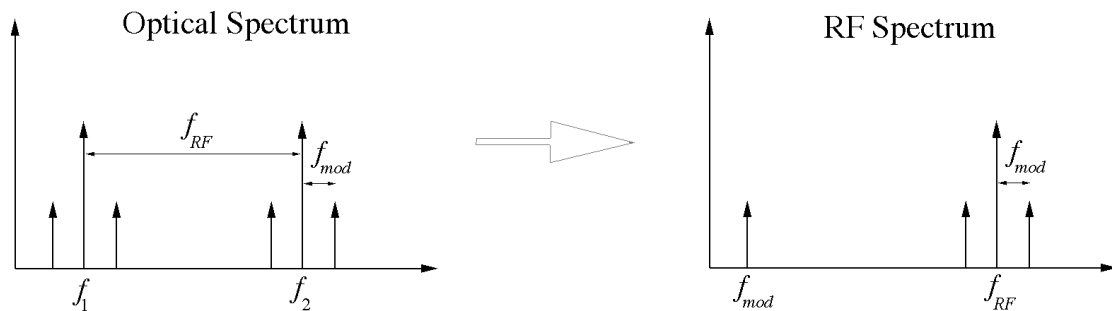


Figure 4.3: Parasitic modulation of the slave lasers

Figure 4.4 shows the RF spectrum of the beating between the free-running lasers. The slave lasers are effectively modulated by the radiated RF power from the master laser current injection needle. RF absorbers are consequently used around the master laser to block the radiated power. In addition, the slave lasers are placed in a Faraday trap to isolate them from any electromagnetic interference. As a result, the unwanted modulation sidebands appearing

in the RF spectrum have practically disappeared (Figure 4.5). Nevertheless, the stability of the system is compromised given that the power of the parasitic modulation sidebands tends to vary a lot (~ 20 dB) when the position of the RF absorbers is slightly changed. When characterizing the RF generated signal, careful attention has to be given so that the parasitic modulation sidebands do effectively disappear.

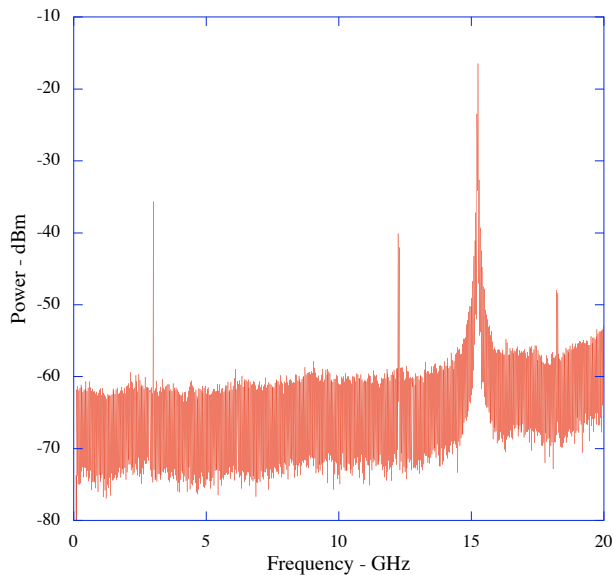


Figure 4.4: RF spectrum without microwave absorbers.

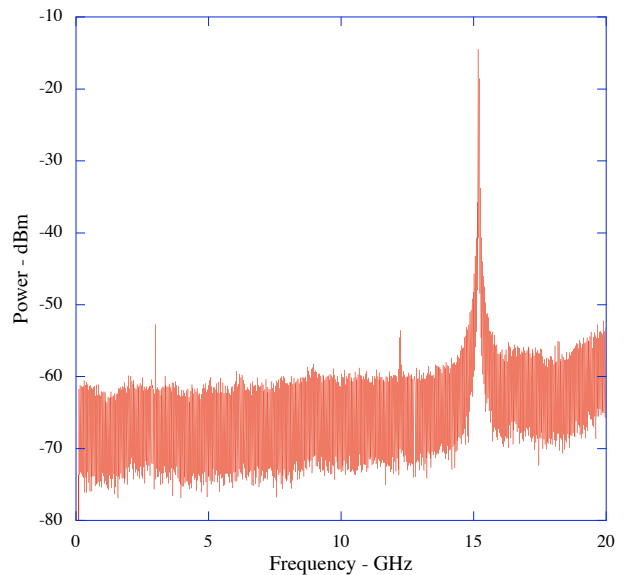


Figure 4.5: RF spectrum with microwave absorbers.

4.3 Sideband Injection Locking Characteristics

Sideband injection locking characteristics are similar than fundamental peak injection locking characteristics. Nevertheless, the gain available in semiconductor lasers has a wide bandwidth and consequently, all modulation sidebands are amplified. In stable locking conditions there is, however, an important overtone rejection rate that depends mainly on the frequency detuning and on the injection rate of the concerned sideband, as well as on the injection rate of the adjacent overtones.

As mentioned before, synchronizing two slave lasers to different sidebands of a modulated master laser should generate a very pure microwave carrier. To obtain a stable locking regime, the following parameters should be optimized: (i) the injection rate between

the modulation sideband chosen and the slave laser, (ii) the frequency detuning, and (iii) the polarization difference between the master and slave laser. For a given injection rate, the locking bandwidth decreases as the polarization of the injected light is rotated towards a perpendicular axis. Moreover, the locking bandwidth stretches as the injection rate increases until the relaxation oscillations begin to appear, followed with chaotic behavior. To better understand the influence of the injection conditions on the slave lasers the concept of locking bandwidth overlapping is introduced.

4.3.1 Locking Bandwidth Overlapping

Recalling that the master laser spectrum presents several modulation sidebands, it is possible to synchronize the slave lasers to one or another sideband. It is possible then, to associate a different locking bandwidth to each modulation sideband as shown in Figure 4.6. For certain values of the relative frequency detuning of the slave laser and the injection rate, the operation point may lie on the stable-locking region associated to two or more different modulation sidebands. In this case, the slave laser emits over different frequencies and the single-mode stability is compromised. For RF generation applications, operation in these regions should be avoided because they generate residual microwave frequencies. This is why the modulation conditions and the choice of sidebands to injection-lock the slave lasers should be carefully selected.

The modulation frequency of the master laser is then a key parameter. The upper limit (<5 GHz) was discussed in the previous section. The lower limit is imposed by the criterion that complete bandwidth overlapping provokes a very low overtone rejection rate. So, the modulation frequency should not only be higher than the desired bandwidth imposed by the bit-rate, but should be high enough to avoid complete bandwidth overlapping. Considering the modulation properties of the master laser, a modulating frequency between 3 and 4 GHz is well suited for microwave generation. In the following, the injection rate and frequency detuning influence on the optical spectrum of the slave lasers is investigated.

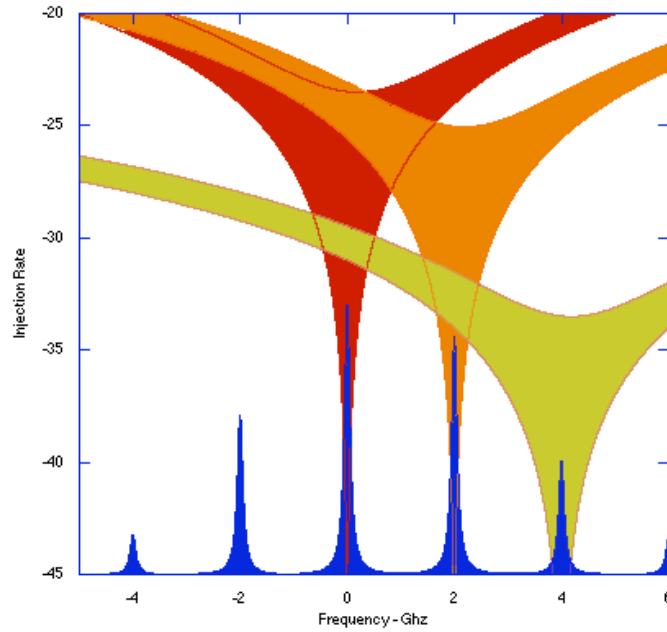


Figure 4.6: Locking bandwidth overlapping.

4.3.2 Injection Rate Influence

To evaluate the influence of the injection rate on the power spectrum of the slave lasers, the experimental setup in Figure 4.1 was adopted using only one slave laser. The master laser was biased at 80 mA and the total modulation power at 3 GHz was 36 dBm. The slave laser current was adjusted so as to cancel the frequency detuning between the slave laser and sideband number -3 from Figure 4.2. The attenuator allows control of the injected power and consequently, control of the injection rate. The evolution of the slave laser power spectrum measured by a Fabry-Perot interferometer as the attenuation varies is shown in Figure 4.7.

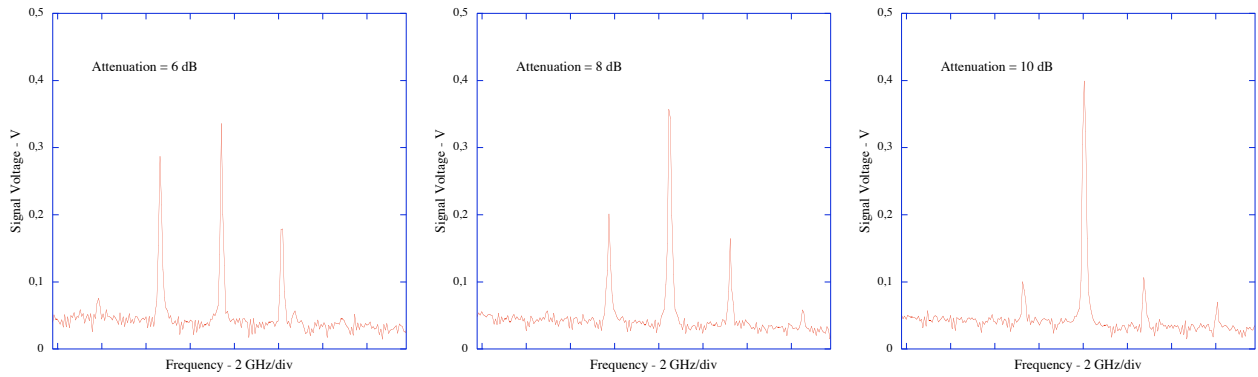


Figure 4.7: Slave laser spectrum evolution as the injection rate varies.

The first results show that it is difficult to obtain a high overtone rejection rate when the attenuation is less than 10 dB. In other words, as the injection rate increases the adjacent sideband power is better amplified and the power diminution of the locked sideband indicates that operation lies close to the relaxation oscillations regime. Increasing the attenuation over 10 dB results in a better overtone rejection and since the dynamic limit of the Fabry-Perot interferometer is attained, the slave laser power spectrum is measured using an optical spectrum analyzer. The results for two injection rates are represented in Figure 4.8. With a high injection rate (attenuation ~ 10 dB), the power spectrum of the injection-locked slave laser is spread over 100 GHz meaning that secondary modulation sidebands are also amplified. The minimum overtone rejection in this case is measured to be 8 dB. The presence of the sideband at a wavelength of 1446.38 nm with a high overtone rejection does not indicate the presence of relaxation oscillations. It may be considered wrongly that the relaxation oscillation sideband is synchronized to the modulation sideband number +4. This is not the case: it can be seen on the optical spectrum of the modulated master laser (Figure 4.2) that the modulation sideband +4 has considerable more power than its adjacent sidebands and this is why the slave laser spectrum has greater overtone rejection around peak +4. Notice the power of the main locked mode equal to -6.9 dBm. Increasing the attenuation to 20 dB (decreasing the injection rate) results in a main-locked mode power increment of 2 dB. The minimum overtone rejection rate also increases to 14 dB. Furthermore, the spectrum presents less spreading. Therefore, it can be concluded that the slave laser acts as a pass-band filter with a 3-dB bandwidth controlled by the injection rate. Further increasing the attenuation results in the unlocking of the slave laser due to the relative low locking bandwidth associated to small injection rates.

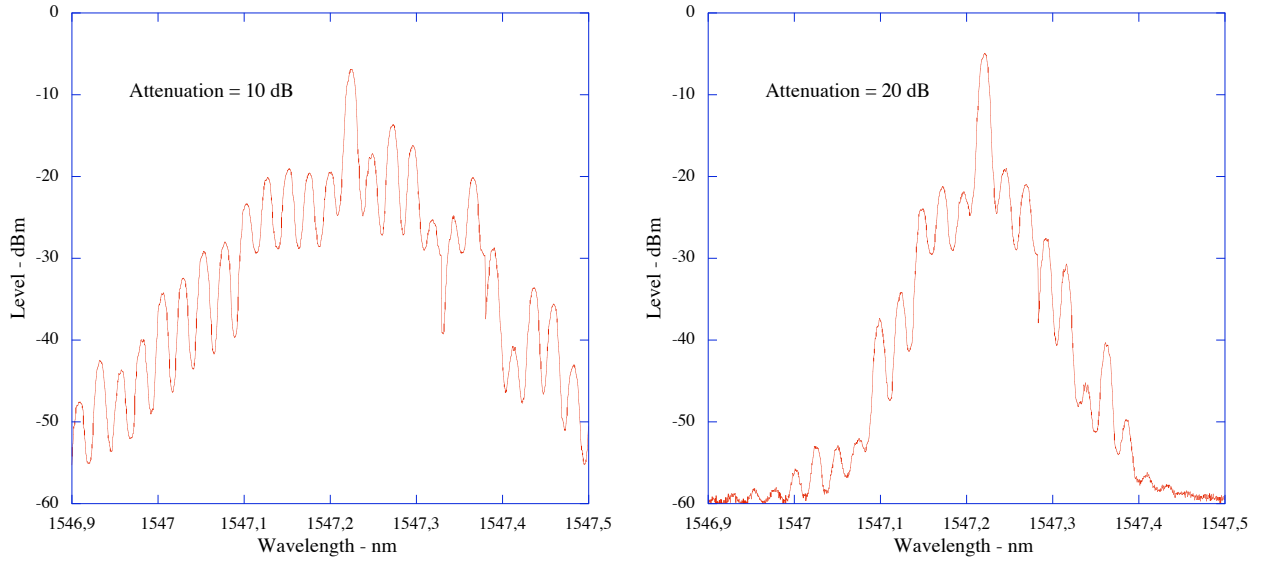


Figure 4.8: Optical spectrum of the locked slave laser at the injection rate limits for stable locking.

4.3.3 Frequency Detuning Influence

To investigate the frequency detuning $\Delta\omega/2\pi = \nu_{master} - \nu_{slave}$ influence on the slave laser power spectrum the same experimental setup as before was used but with different conditions. Mainly, the modulation sideband chosen for injection locking was peak number – 8. The slave laser biasing current was varied, creating a change in the frequency detuning. The optical attenuation was slightly adjusted so that the optical injection rate remained constant for different frequency detunings. The measurements were done with an optical spectrum analyzer because the dynamic range of the Fabry-Perot interferometer is not sufficient to measure simultaneously the main-peak power and the adjacent sideband power. The power spectrum of the injected slave laser is shown in Figure 4.9 for positive and negative detuning, which is obtained by slightly varying the biasing current of the slave laser. It is observed that for a positive detuning of 650 MHz, the adjacent sideband rejection rate is 13 dB, whereas a frequency detuning of –650 MHz results in a rejection rate of 20 dB. This is explained by the fact that near the static limit for positive detunings, the threshold gain of the locked mode is higher than that of the free-running mode. The frequency detuning also has an influence on the power under the locked-peak. Since the overtone rejection rate is stronger for negative detunings, more power is concentrated under the main-locked peak. The power change was 1.5 dB for frequency detuning change of 1.3 GHz. Considering the slave laser as

an optical filter, the frequency detuning has little influence on the 3-dB bandwidth since distant sidebands are almost equal in power for different frequency detunings.

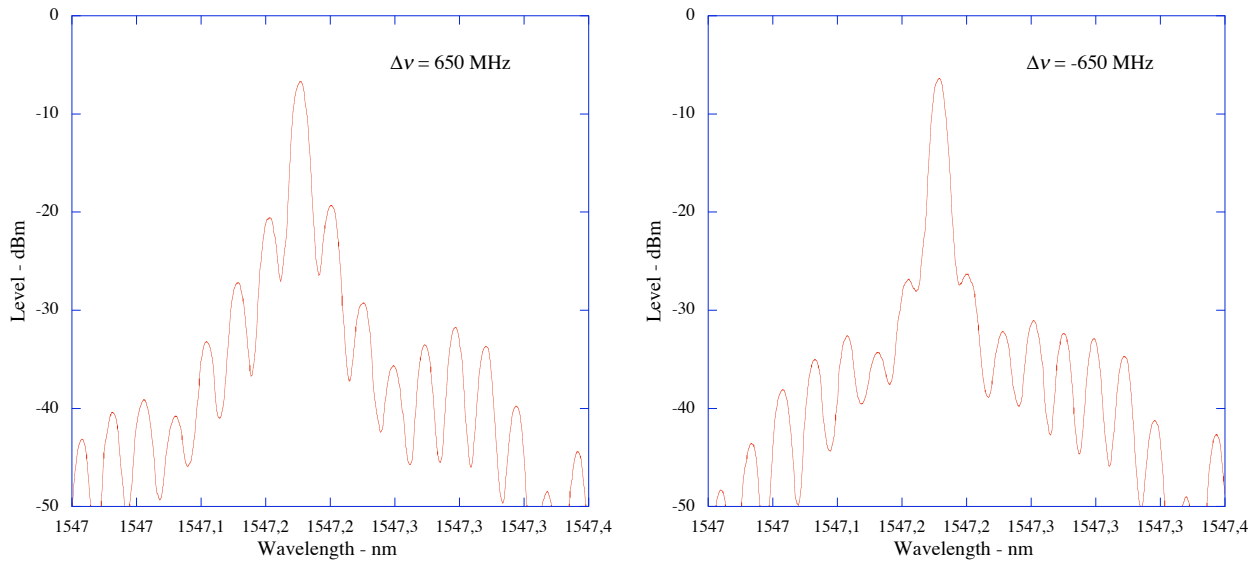


Figure 4.9: Slave laser spectrum near the positive and negative detuning edge of the locking bandwidth.

4.3.4 Injection Locking Stability

Long-term stability (>1 hr) of the sideband-injected mode was rarely obtained. The main reason is due to thermal instability, which provokes a frequency variation. This causes a continuous frequency-detuning change until the slave laser no longer operates within the stable locking bandwidth and desynchronizes from the modulation sideband and depending on the injection rate it can synchronize to an adjacent modulation sideband. Fortunately however, the time taken for the slave laser to desynchronize once set at the edge of the stable locking bandwidth is greater than 25 min, so there was time enough to make the measurements.

Another type of instability was detected. The fiber/laser coupling factor deteriorates with time, but the time constant of this phenomenon (~ 4 hrs) is much greater than for the phenomenon previously described. As a consequence, the power injected to the slave laser, and therefore, the injection rate decrease. This instability can be attributed to the mechanical assembly used. In fact, the heated face of the Peltier cooler diffuses heat to the ensemble of the mechanical elements used to align the laser with the tapered lensed fiber. The dilatation of the different mechanical elements conducts then to a partial misalignment between laser

and fiber. This phenomenon is accompanied by a decrease of the slave laser power coupled to the fiber. Taking into account the expansion coefficient and the mass of all the mechanical elements, several hours can pass by before the whole system arrives to thermal equilibrium.

To obtain a better thermal stability, direct improvements can be realized by modifying the heat sink structure. Notably, by adding a radiator to the heated face of the Peltier cooler and by thermally isolating the slave laser base from the rest of the mechanical elements. A more comfortable solution, would be to use packaged-commercial lasers with no optical isolation and preferably with a polarization maintaining fiber. The small elements inside the package would then increase the thermal reactivity and the fiber/laser coupling would remain constant. The system would then be less sensitive to external electromagnetic perturbations and more mechanically robust.

4.4 Experimental Demonstration of Microwave Generation

In a master/slave laser configuration, the locking bandwidth is defined as the maximum frequency detuning range that keeps the slave laser locked for a given injection rate. In principle, the slave laser externally locked to a single sideband should reject all other frequencies, but actually, because of the large gain bandwidth of semiconductor lasers, several adjacent sidebands are also amplified. The impact of these overtones on the RF properties is investigated. Optimization of injection conditions is discussed with the objective to understand the difficulties of the technique. A characterization of the optically generated RF carrier is presented as well.

4.4.1 Optimal Sideband Injection Locking

The Fabry-Perot (FP) interferometer spectrum of the modulated master laser is simultaneously observed with the slave lasers FP and electrical spectrum after conversion with a high-speed photodetector. The modulation frequency together with the generator electrical power was varied, respectively, from 1 to 5 GHz and from 0 dBm to 35 dBm. Each slave laser is frequency tuned to different IM-FM sidebands of the master laser and it was observed that the conversion efficiency strongly depends on the master laser modulation properties. In order to have a stabilized and pure RF signal, the resulting point of operation should be within the stable locking bandwidth; to achieve this, the choice of the modulation sidebands has to be optimized. This means that the modulation frequency should be sufficiently high (≥ 1 GHz) to prevent overlapping of the locking bandwidths associated to each modulation. On the other hand, the modulation depth determines the power under each sideband, so it should be carefully chosen to favor the desired power ratio. Figure 4.10 illustrates the peak power of different overtones for a modulated master laser in function of the modulation depth (modulation frequency = 3 GHz). It is observed that it's not always best to lock the slave lasers to corresponding overtones around the fundamental frequency (i.e. $-n$ th and $+n$ th) because the phase-amplitude coupling factor causes a disymmetrical spectrum. In other words, the conversion efficiency is not optimal when the relative weight between the slave lasers amplitude is not equal. Consequently, the sidebands should be chosen near an

intersection point in the peak power curves. Although there exists intersections at higher modulations depths, this region corresponds to nearly gain-switching operation and the time interval between pulses could be comparable to the time it takes the slave lasers to fully synchronize.

The beat spectrum is shown on Figure 4.11 where a signal-to-noise ratio of over 35 dB is obtained. The slave lasers were injection-locked to the +1 and -2 harmonics of the master laser, which had a modulation depth of ~24%. Usually, if a slave laser is well locked on a specific modulation sideband it has the ability to reject all other frequencies. In practice this not the case as can be seen from the high power reading of the side peaks. This residual power is mainly induced by the injection of the carrier component, which modulates the slave laser even though it's found outside the locking range. Anyway, electrical filtering necessarily done in any receiver will eliminate spurious frequencies for specific applications. The resulting RF linewidth was limited by the spectrum analyzer resolution but it is estimated to be in the sub-hertz region.

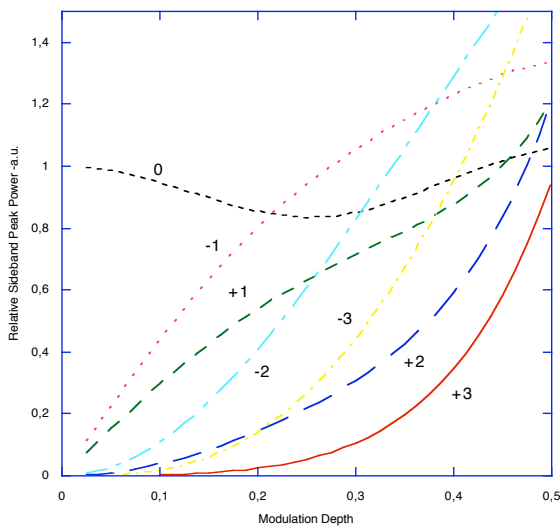


Figure 4.10: Sidebands peak power in function of the modulation depth with the overtone number as parameter.

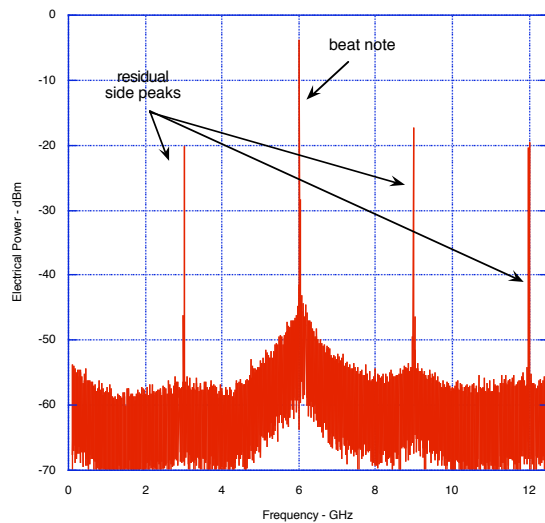


Figure 4.11: Beatnote power spectrum of the detected current.

4.4.2 Spectral Analysis of RF Frequencies

The master laser was biased at 80 mA and the modulating power at 4 GHz was 39 dBm giving an effective modulation depth of ~26%. The modulation sidebands were chosen so as to minimize the bandwidth overlapping. The slave laser frequencies were adjusted to lock them in to the -3 and -8 modulation sidebands (Figure 4.12) in order to produce a beating frequency of 20 GHz. The RF spectrum of the free-running laser beating was first measured without electromagnetic isolation and without RF absorbers. This explains the available power at the frequencies of 4 and 16 GHz.

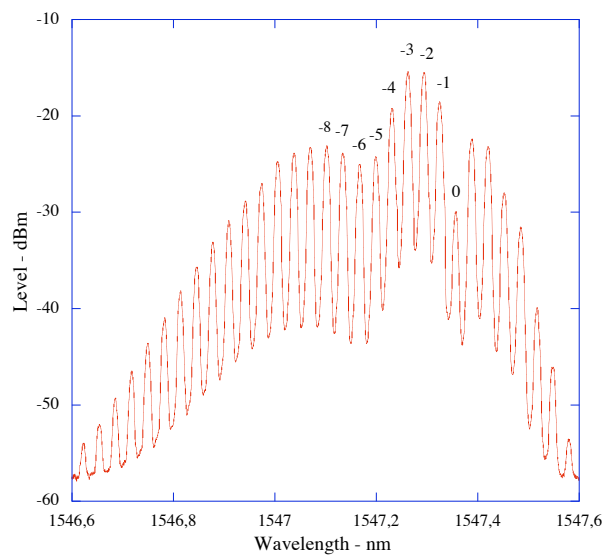


Figure 4.12: Master laser spectrum modulated at 4 GHz.

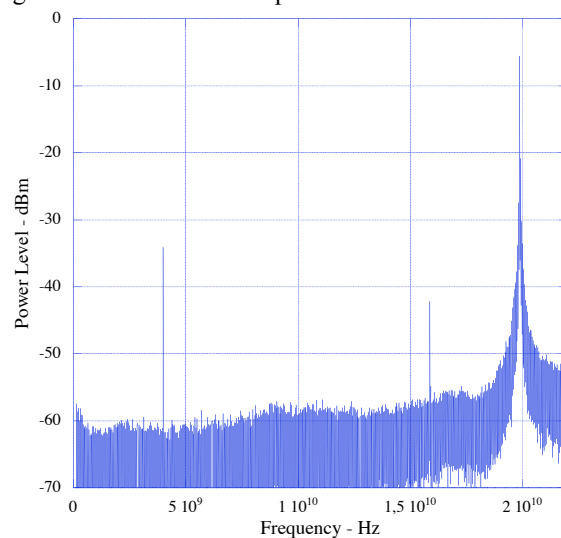


Figure 4.13: RF Spectrum of free-running beating at 20 GHz.

The slave lasers were then optically injected by the modulated master laser. Figure 4.14 represents the results for two optical attenuations of the master laser corresponding to two different values of the optical injected power. The RF power of the free-running beatnote at 20 GHz is almost equivalent to that of the injection-locked slave lasers. The spectral linewidth of the injection-locked lasers has obviously decreased due to strong phase correlation.

As previously stated, the apparition of several unwanted RF frequencies is inevitable. These frequencies are due to the fact that each slave laser emits over the adjacent modulation sidebands separated by 4 GHz. However, it is observed that some of the residual RF frequencies do not correspond to 4 GHz multiples but to multiples of 2 GHz. The origin of this periodicity doubling can be understood by noticing that the injection rate for the -8 modulation sideband is 10 dB less than the -3 modulation sideband. The slave laser synchronized to the latter sideband presents an operation regime characterized by undamped relaxation oscillations with period doubling. Evidence of operation on this regime is found by observing that an increase of the master laser optical attenuation results in decrease of the half-frequency residual peaks. Furthermore, observation of optical spectrum of this slave laser confirms it. The RF power of peaks at 2, 6 10, 14 and 18 GHz is very sensible to the injection rate as can be seen in Figure 4.14. In contrast, the RF power of peaks at 4 GHz multiples appears unaffected by the optical attenuation of the injected light. The overtone rejection rate with respect to the adjacent sidepeak at 18 GHz is increased from 27 to 35 dB when the optical injection rate is decreases by 3 dB. The overtone rejection rate with respect to the peak at 16 GHz remains constant at 16 dB. This leads then to the assumption that the residual frequencies multiples of 4 GHz are due to the induced modulation on the slave lasers, caused by electromagnetic interference.

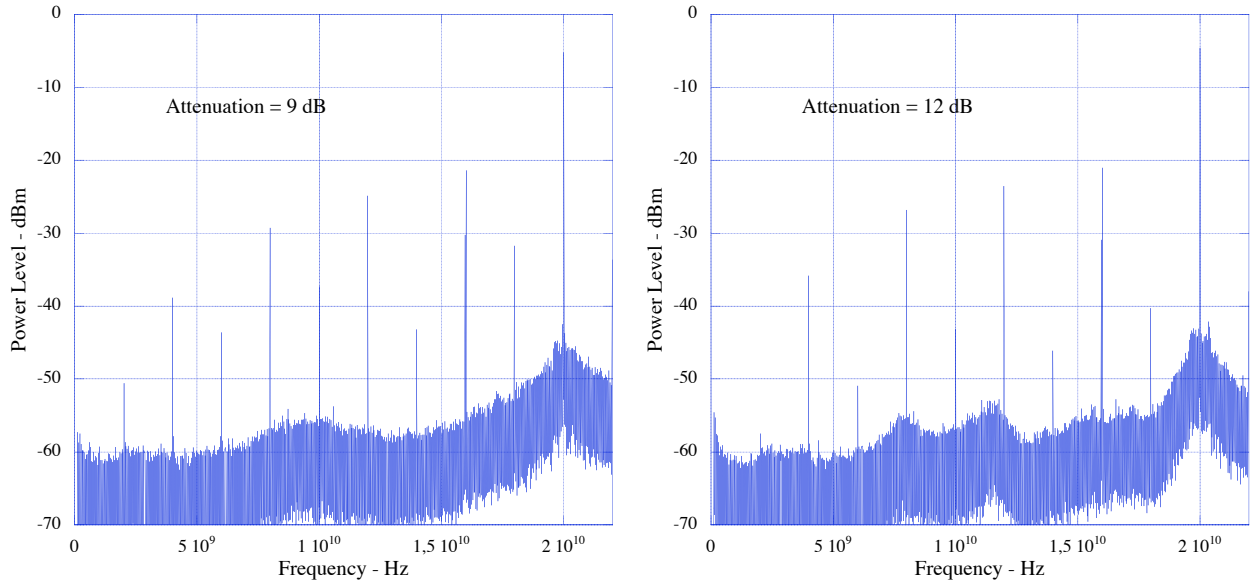


Figure 4.14: RF spectrum of the beating signal for different injection rates.

4.4.3 Influence of the Injection Rate on RF Spectrum

Now the master laser is modulated at a frequency of 3 GHz (Figure 4.15) with an electrical driving power of 10 dBm (effective modulation depth $\sim 16\%$). These operating conditions as well as the choice of sidebands were carefully selected to obtain the desired RF spectral properties. The injection rate for a negative frequency detuning (-500 MHz) is varied. The decrease of the overtone rejection rate as the injection rate increases arises from the following physical mechanism: the relaxation frequency resonance is modified by optical injection and defines a static/dynamic limit (undamped) of the locking range. Operation just beyond this limit results in a chaotic behavior. Moreover strong signals entering the slave laser cavity unleash competition between the adjacent sidebands due to locking bandwidth overlapping. The impact on the RF spectrum is shown in Figure 4.16 for a 12 GHz generated signal. For similar optical powers of both slave lasers and similar injection conditions, a 4 dB increase of the injection rate (attenuation of the injected signal) results in 7 dB decrease of the overtone rejection rate. Furthermore, a 2 dB degradation of the signal to noise ratio is observed.

Further experimental observations show that the spectral purity is inherently dependent on the frequency detuning and on the relative power of the chosen modulation sideband with respect to the adjacent sidebands. Likewise the overtone rejection rate and locking stability

also deeply depend on the injection rate. With the low value of the injection rate, attenuated modulation sidebands further away quickly diminish improving the RF spectral purity. By carefully selecting the frequency detuning and the injection rate the overtone rejection ratio can be greatly enhanced.

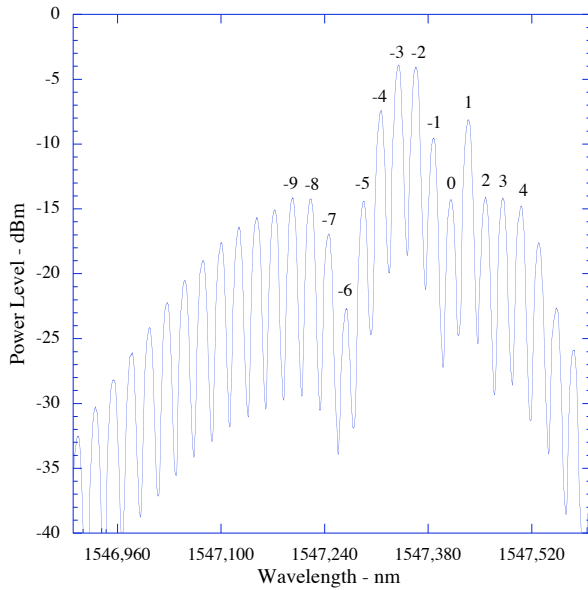


Figure 4.15: Modulated master laser at 3 GHz

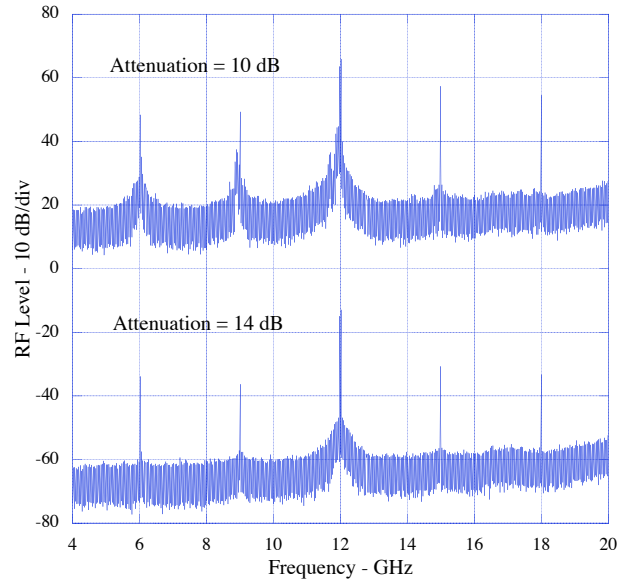


Figure 4.16: RF spectrum

4.4.4 Transmission Over 30 km of a Single-Mode Fiber

The master laser was biased at 80 mA and the modulating power at 3 GHz was 36 dBm giving an effective modulation depth of $\sim 24\%$. The modulation sidebands were chosen so as to minimize the bandwidth overlapping (Figure 4.2). The slave laser frequencies were adjusted to lock them in to the -14 and -9 modulation sidebands in order to produce a beating frequency of 15 GHz. The slave lasers optical spectrum is represented in Figure 4.17 and the resulting RF spectrum is found in Figure 4.18. The overtone rejection rate obtained is better than 20 dB and the signal to noise ratio is ~ 45 dB. To acknowledge the importance of the sideband modulation choice together with the injection locking conditions, the slave lasers were locked to different modulation sidebands. The optical spectrum (Figure 4.19) and the

resulting RF spectrum (Figure 4.20) clearly present deteriorated characteristics. The overtone rejection rate is now only about 8 dB and the signal to noise ratio has decreased to 32 dB.

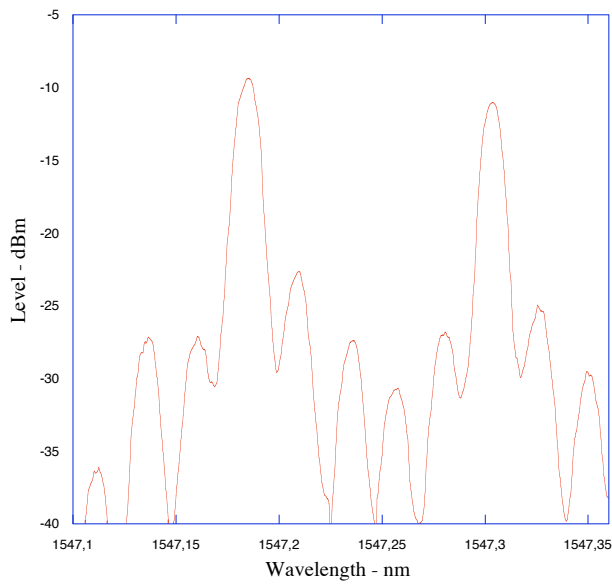


Figure 4.17: Slave lasers optical spectrum

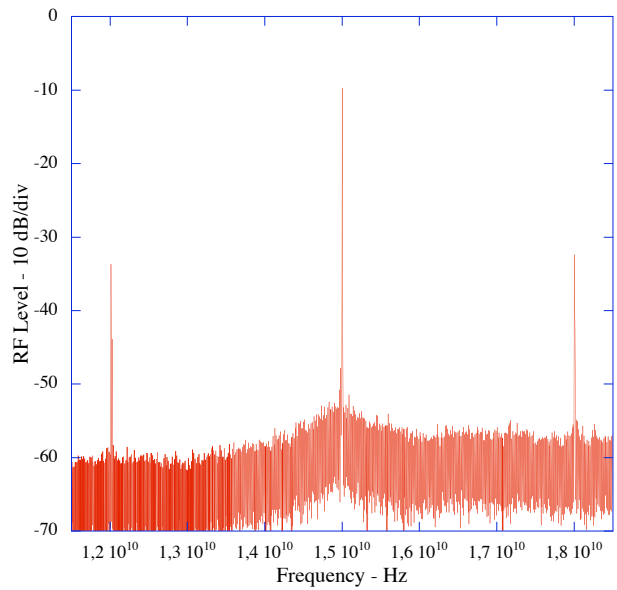


Figure 4.18: Resulting RF spectrum

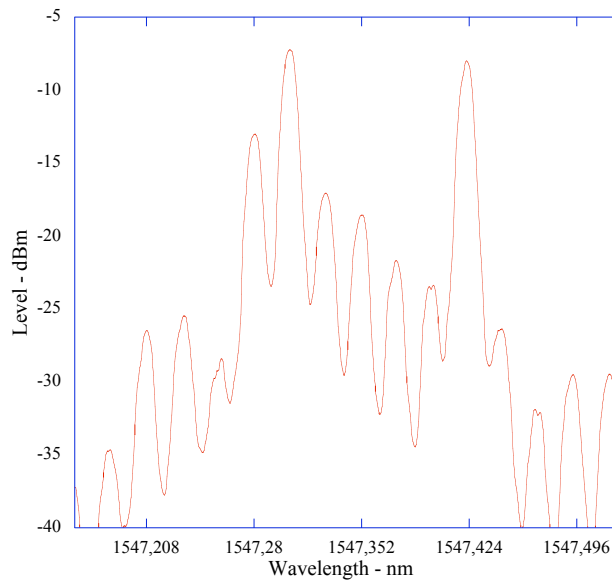


Figure 4.19: Slave lasers optical spectrum

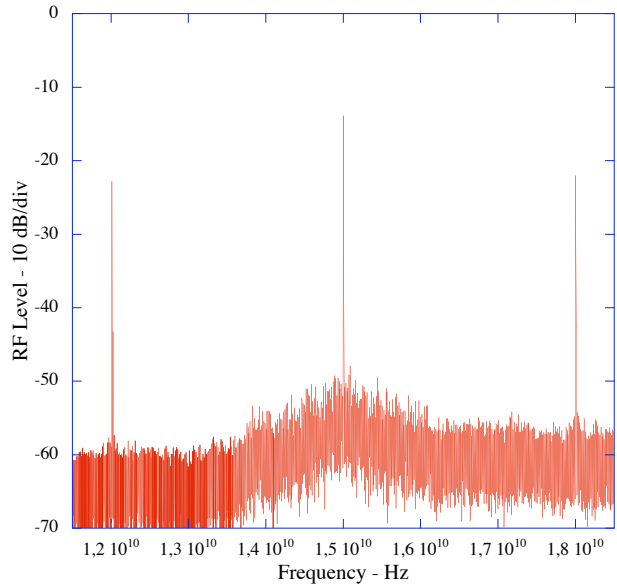


Figure 4.20: Resulting RF spectrum

The optically generated RF carrier at 15 GHz was transmitted via 30 km of a standard single-mode optical fiber. As a result of chromatic fiber dispersion, a delay τ_{disp} is added between the optical fields of both slave lasers. The delay for this transmission distance and carrier frequency is ~ 61 ps, which is lower than the coherence time $1/\Delta\nu$ of the laser ($\sim 1 \mu s$). This means that the two fields are partially uncorrelated. The rms phase error is calculated using the results of chapter one and is found to be $\sim 0.11^\circ$. The impact of this phase error on

the RF spectrum is shown in Figure 4.21 where the resolution bandwidth is 10 Hz and the display scan bandwidth is 10 kHz. As a result of the partial phase correlation the RF spectral purity has been degraded.

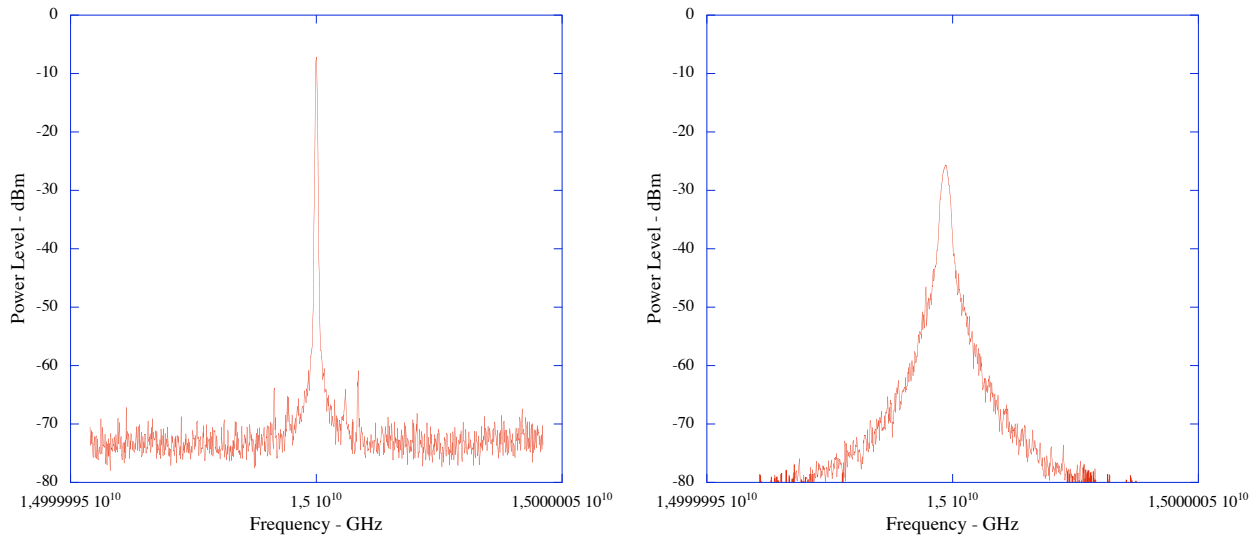


Figure 4.21: Partial uncorrelation after 30 km of transmission distance.

4.4.5 RF Characteristics

The frequency tunability of the microwave source can be obtained by observing the power spectrum of the modulated master laser. The most distant sidebands that can be chosen for stable injection locking the slave lasers are peak numbers -19 and 6 , making the maximum frequency equal to 75 and 100 GHz for a modulation frequency of 3 and 4 GHz. By attempting to increase the modulation depth, e.g. by adapting an impedance matching circuit, higher-order modulation sidebands could be successfully used to synchronize the slave lasers, thus providing a greater frequency tunability. Actually the modulation frequency can be tuned continuously so the resulting tunability of the microwave frequency can also be varied continuously with a frequency precision imposed by the frequency precision of the RF generator used to modulate the master laser. The frequency tuning speed of the source remains a drawback. It is not straightforward to simply change, for example, the modulation current, without optimizing the injection conditions.

The RF output power is however, a mayor advantage inherent to the sideband injection locking technique. The maximum output power is limited by the saturation power of the photodetector, but can be as high as several milliwatts. In our experiments, the maximum RF output power obtained was -5 dBm.

Another mayor advantage is the remotability for controlling basic parameters of the RF carrier. The amplitude, the time delay and the phase are remotely controlled at the control station through simple adjustments of the slave lasers differential delay, their current and temperature.

The limit on the repetition rate and number of channels when transmitting data by directly modulating one of the slave lasers is imposed by the locking bandwidth. However, adding slave lasers and synchronizing them to different modulation sidebands allows increasing the overall transmission bandwidth of the source. In our case, the slave lasers were not modulated. Thermal instabilities have to be counteracted before attempting to characterize the source as a transmission system.

4.5 Conclusion

The microwave generation technique by optical heterodyning of two slave lasers was optimized considering the modulation properties of the master laser and the injection conditions of the slave lasers. Conversion efficiencies higher than 50% were obtained. The use of high performance lasers in the control station may substantially lower costs since no active components must be installed in the base stations, specially microwave amplifiers. In particular, it was found that the RF spectral properties are improved by maximizing the overtone rejection rate. This is done by carefully selecting the injection rate and the frequency detuning. In addition, the modulation conditions of the master laser were established for guaranteeing stable operation.

Chapter 5: **General Conclusion**

Optical communication devices and techniques now play a key role in many analog microwave applications. Numerous advantages include size, weight, link loss, bandwidth, EMI immunity, and new functions such as optical generation of microwaves, the subject of this thesis. The general approach to the subject was undertaken from an exploratory, experimental, and theoretical point of view. The technique experimentally developed, sideband injection locking, consisted in optical heterodyning two phase-correlated optical waves obtained from two slave lasers injection-locked to the sidebands of sub-harmonically modulated master laser. The objective of the thesis was to establish the feasibility of the technique for servicing local high-speed access in terms of link performance, to understand the locking properties dependence on the structure of distributed feedback lasers, to comprehend the slave lasers locking properties influence on spectral characteristics of the RF generated carriers, to measure the complex index of refraction changes due to optical injection in DFB lasers, and to document a procedure for optimizing the RF spectral characteristics. As a result the subject was covered from the optoelectronic and communications engineering point of views. The major contributions of this work are summarized as follows

1. A feasibility analysis on link performance calculating the phase noise probability distribution of the optical-heterodyne generated RF carrier. It was determined that links with a $BER < 10^{-9}$ are possible in the 60GHz range using a 155 Mbps QPSK format over 15 km of fiber distance as long as the dispersion delay is compensated by an opposing differential delay between both slave lasers.

2. A method based on the coupled-wave theory for describing the optically injection-induced gain and frequency changes of distributed feedback lasers. The locking bandwidth dependence on grating characteristics was determined as a result.

3. A measurement method based on a phase-sensitive OLCR for determining the optically induced complex index changes of a DFB lasers directly from gain and optical length changes obtained from the reflectogram data. The results were then directly used to estimate the effective linewidth enhancement factor agreeing with other indirect measurements.

4. An experimental procedure for optimizing the RF spectral properties in terms of the modulated master and slave lasers power spectral densities and, in terms of the optical injection conditions. RF carriers up to 20 GHz were generated exhibiting a sub-hertz linewidth, with a carrier to noise ratio ~ 45 dB and a residual frequencies rejection rate > 23 dB.

Future work on the subject might be focused on the channel link performance, considering coding, modulation formats, distortion, and non-linear effects. On the other hand, the only requirements needed for testing the technique with specific applications, are a stricter control of frequency difference between master and slave lasers and a suitable packaging of the device. The upstream link could also be developed enabling more interesting applications. To do so, a very simple way is to use the unmodulated optical carrier at the base station for the upstream link since baseband data can directly modulate it. The only additions to the base station would be a splitter, an optical and RF filter, and simple external optical modulator.

To further add value to the device an automatic control system can be added so as to allow fine and wide RF frequency tuning. An electronic control loop must be added for constantly monitoring the injection locking conditions and adjusting the diode current and temperature as required by the petitioned RF frequency. An even better device would allow a variable differential delay enabling the use of the device for different transmission distances. Another future course of action might be to combine injection locking with a phase-lock loop, forming an optical injection phase-lock loop. Here, the phase-lock loop path controls the close-to-carrier phase noise and laser frequency drift, while the injection-locking path is in charge of wide-band phase-noise suppression. A further step in the development of the device would be to consider networking issues and interconnection with other networks.

Future work on injection locking might focus on a precise description of phase noise transfer through injection locking determining the causes for incomplete correlation. With regards to the locking range, the theoretical method presented here could be applied for different laser structures and different materials leading to the possibility of engineering the shape of the locking bandwidth.

Journal and Conference Publications issued from this work :

1. "Caracterización de componentes fotónicos utilizando reflectometría óptica de baja coherencia, *Rev. Mex. Física*, 72, pp. 379-386, 2006.
2. "Optically generated radio frequency signals by subharmonically injection-locked semiconductor lasers", Conference on Lasers and Electro-optics CLEO, San Francisco, CA, 17-21 May 2004.
3. "Analysis of Optical-Injected Distributed Feedback Lasers Using Complex Optical Low-Coherence Reflectometry", *IEEE PTL*, 15, pp. 1041-1135, 2003.
4. "Influence of the locking characteristics on signal to noise ratio of optically generated microwaves using the sideband injection locking technique", Conference on Lasers and Electro-optics CLEO Europe, Munich, Germany, 23-27 June 2003.
5. "Determination of optically-induced complex index change using a phase-sensitive OLCR technique", European Conference on Optical Communication ECOC'02, Copenhagen, Denmark, Sept 2002.
6. "Locking range dependence on the grating characteristics of distributed feedback semiconductor lasers" 14th Annual Meeting of the Lasers and Electro-Optics Society. IEEE LEOS, San Diego, CA, Nov 2001.
7. "Microwave generation by optimal sideband injection locking of two gain-coupled distributed feedback semiconductor lasers," 14th Annual Meeting of the Lasers and Electro-Optics Society. IEEE LEOS, San Diego, CA, Nov 2001
8. "Etude des lasers à semiconducteurs à réaction distribuée soumis à une injection optique," 20èmes Journées Nationales d'Optique Guidée, JNOG 2000, Toulouse, France, Nov. 2000.

